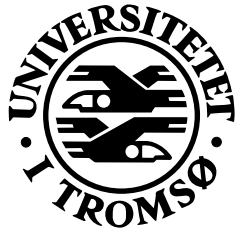

A dissertation for the degree of Doctor Scientiarum

---

# Interferometric and high time-resolution observations of Naturally Enhanced Ion-Acoustic Echoes at the EISCAT Svalbard Radar: Software Radar and Incoherent Scattering

**Tom Grydeland**

May 2003

Faculty of Science

Department of Physics

University of Tromsø

*Til min kjære Ane*

**Sammendrag**

Vi vet at det synlige nordlyset har struktur på mange forskjellige skalaer, helt ned til noen titalls meter. Ved å bruke EISCAT-radarene på Svalbard som et interferometer har vi påvist strukturer i radarekko fra nordlyshimmelen på en skala som nærmer seg den i det synlige nordlyset, samtidig med dette, men i langt større høyder.

I denne avhandlinga tar vi for oss hvordan disse radarobservasjonene ble gjort, hva de innebærer for teoretiske forklaringsmodeller, samt et nytt rammeverk for design og implementasjon av programvarebaserte radarer og andre vitenskapelige radioinstrumenter, spesielt den signalbehandlingen som har gjort disse observasjonene mulige.

**Abstract**

We know that the visible Aurora Borealis is structured on many different scales, down to a few tens of metres. By using the EISCAT radars on Svalbard as an interferometer, we have found structures in the radio echoes from the auroral ionosphere on a scale approaching that of the visible aurora, and simultaneously with it, but at far greater ranges.

In this thesis we discuss how these radar observations were made, what they imply for theoretical explanations, as well as a new framework for the design and implementation of software-defined radar and other radio science instrumentation, in particular the signal processing which made these observations possible.

# Acknowledgements

"Occasionally people do get the chance to learn things during the course of their education," Frank Lind told me as I was approaching a local exasperation density maximum. Besides being a reminder to me to take a task I am unprepared for as an opportunity, it is also an example of that particular form of humour which is amusing because it is true in an unexpected way.

Although getting to this point has been a lot of hard work, it has also been a lot of fun, and I want to thank all the people who helped make it fun, and keeping sight of the fun throughout. Many more people who could have been mentioned — you are all appreciated, even if you are not mentioned here by name.

Thanks to my supervisor, César La Hoz. Your sure guidance and experience has been invaluable in this process, and I have had more (and more heated) arguments with you than with anyone else the last ten years.

Thanks to my co-supervisor Tony van Eyken for always considering my suggestions, and to John Holt for getting me to Millstone Hill and trusting me with MIDAS-W even in its infancy. Thanks to Tor Hagfors, a driving force behind the introduction of interferometry at the ESR, and whose experience has been invaluable in this work. Thanks to Einar Mjølhus for patiently trying, over and over, to teach me plasma physics.

Thanks to Mårten, for your never failing enthusiasm, and for taking on tasks that were far beyond your responsibility. Thanks to Tom, Frank and Phil for making my year at Haystack so memorable. Thanks to Liv, Marit and Ramona for making life quite a bit easier. Thanks to Tom Duck in particular for Mills Mess.

Funding from Norsk Forskningsråd and the Geophysics group at the University of Tromsø made my stay at Millstone Hill possible, for which I am grateful.

Thanks to Lars, for being a friend, always.

Takk sist — men på ingen som helst måte minst — til Ane.
Dette ville ikke vært mulig uten deg.

# Contents

# Chapter 1

# Introduction

## 1.1 Motivation

One of the truly remarkable things about children is their fantastic curiosity about all things around them. No explanation is ever good enough to fully satisfy, and every answer leads to the next set of questions.

I believe one thing which distinguishes those who are scientists at heart from other people is the way they never let go of that curiosity, never simply accept that things are the way they are. I had this brilliantly demonstrated during a guided tour of Cité de l'Espace in Toulouse, where the guide had a hard time indeed getting the attention of the scientists (myself included) who were happily playing with all the wonderful exhibits demonstrating Coriolis force, the Galaxy seen at different parts of the radio wave spectrum, or a number of other exciting demonstrations and had no time to listen to her.

The Science fiction author and biologist Isaac Asimov once compared science to a garden. Once, around the turn of the previous century believed to be a tidy English garden, neatly sectioned and small enough that a well-educated person could be expected to have some familiarity with most areas. Since then, the garden has grown beyond all expectations, the neat divisions have broken down, and scientists struggle to regain some sense of neatness in smaller and smaller sections that become increasingly hard to separate from neighbouring fields.

So which section of the garden should one attend to?

As my own curiosity has been to do with the tangible world around us, the study of physics has been a natural choice.

A naturally occurring phenomenon which commands attention in the polar regions is the spectacular Aurora Borealis, the Northern Lights. Here, man's fascination with the infinite Universe is combined with a highly dynamic spectacle visible to the naked eye, and with the explanation of crucial parts still missing.

In Tromsø, the EISCAT radars are perfectly located for adding a dimension to the study of aurorae apart from what the naked eye can see. Looking for a direction with promise of an opportunity for significant development of understanding and which was not already being explored by everybody else led to the study of incoherent scatter plasma lines, the subject of my Master's thesis.

Another strong fascination with me is that of making things work, and the creativity involved in making things that work in useful ways. Having learnt how many different uses can be found for plasma lines in incoherent scattering, and seeing that the EISCAT Svalbard Radar had no provisions for making plasma line observations, a project which would be both useful and interesting was to implement such a capability, which might also help explain the highly variable spectra seen at the ESR.

Also driven by the desire to create useful things is another project, with potentially more long-term impact; the MIDAS-W Software Radar prototype and the Open Radar Initiative. This project has potential to redefine the way we think of radio science instrumentation.

The construction of the second antenna at the ESR allowed of the opportunity to do receive-side interferometry, and at a time where the development data acquisition and signal processing components from the MIDAS-W Software Radar prototype had advanced to the point where they could be used for such a task.

Several different forms of motivation therefore converge on this project — the fascination of a highly dynamic naturally occurring phenomenon, the interesting physics underlying it, applying new techniques and developing the technology involved for these.

## 1.2 Original Project Description (På Norsk)

Tromsø, 29. januar 1999

### 1.2.1 Innledning

Hoveddelen av den tilbakespredte energien i en inkoherent spredningsradar er sentrert innenfor noen kHz av senderfrekvensen, i det såkalte ionespekteret eller ionelinja. De aller fleste eksperimenter med slike radarer, herunder alle fellesprogrammene til EISCAT, tar da også bare signal fra denne sentrale delen av spekteret.

Den neste betydelige delen av spekteret kalles plasmalinja. På samme måte som ionespekteret svarer til de ione-akustiske bølgene svarer plasmalinja til elektrostatiske (Langmuir-) bølger i plasmaet. Ettersom elektrontettheten i ionosfæren øker fra null til $10^{12}\,\mathrm{m}^{-3}$ varierer frekvensen til plasmalinja over mange MHz. Den er derfor vanskelig å observere.

Plasmalinjer er imidlertid svært interessante for en plasmafysiker. Plasmalinja gir oss estimater for f.eks. elektrontetthet fullstendig uavhengig av ionespekteret, og samtidige

observasjoner av opp- og nedskifta plasmalinjer kan gi ytterligere målepunkter uavhengig av ionespekteret. Disse punktene kan brukes for å bestemme flere av de vanlige ionosfæreparametrene under analysen, eller for å bestemme parametrene med bedre nøyaktighet. Plasmalinjedata kan også brukes til mer nøyaktig kalibrering av ionespektrumsanalysen enn hva som ellers er mulig.

I hovedfaget mitt designet og implementerte jeg et eksperiment for de eksisterende fastlandsradarene med en bedre tidsoppløsning, en mer optimalisert ionespektrumsdel for den delen av ionosfæren vi ser på, samt observasjoner av opp- og nedskifta plasmalinjer på samme tid.

### 1.2.2 En fortsettelse inn i et doktorgradsprosjekt

Alt som er sagt om plasmalinjer i innledninga gjelder minst like mye for EISCATs Svalbard Radar (ESR). En av de observasjonene som er gjort til nå (23. januar 1997) viser perioder på 5 – 10 min med rolige forhold, adskilt av kortere perioder med svært urolige forhold. Under de urolige periodene har vi observert svært mange anomale spektra med stor variasjon både i tid og rom (høyde). Det er etterhvert åpenbart at den enkle, Maxwellske forklaringen som har vært så anvendelig på inkoherent spredning til nå, ikke er god nok til å beskrive fenomener vi ser med ESR. Mange arbeider allerede med disse spektrene. Plasmalinjeobservasjoner vil være til stor hjelp for å avgjøre hvordan disse anomale spektrene kan tolkes, og hvilke fysiske parametre vi kan avlede fra disse. Vi håper også at plasmalinjedataene skal hjelpe oss til en forståelse av den fine strukturen vi ser i de analyserte dataene.

Det eksisterende mottakersystemet for ESR har ingen mulighet til å observere plasmalinjer. A/D omformeren har en teoretisk båndbredde på rundt 10 MHz, nok til å motta ionespekteret og plasmalinjer med moderate frekvenser, men den effektive båndbredden er kun ca. 4 MHz. Planen for å observere plasmalinjer med ESR er å duplisere hele mottakersida fra og med andre mixer/forsterker to ganger. Disse skal installeres snarest. De nye mottakerne vil etter all sannsynlighet ha en større båndbredde enn dagens system. Med to slike moduler vil man kunne observere begge plasmalinjene samtidig og kontinuerlig.

Ingen av de eksisterende eksperimentene på ESR har noen plasmalinjekomponenter. Det vil imidlertid la seg gjøre å inkorporere en ekstra modulasjon i sendermønsteret til f.eks. dagens gup3-eksperiment som er et program til generelt bruk, med observasjoner fra 85 til 600 km.

Et første steg i prosjektet vil være å designe og implementere første generasjon plasmalinjeeksperimenter med én mottakermodul på ESR. Det vil også være interessant å forsøke å gjøre observasjoner av både opp- og nedskifta plasmalinjer ved å bytte senterfrekvens på mottakermodulen mellom pulsene. For denne delen av prosjektet er det nødvendig med et opphold på ESR.

En annen interessant idé i dette er å bruke en spesialbygget mottaker lignende den som ble utviklet av F. T. Djuth for bruk ved Areciboradaren eller en moderne videreutvikling

av denne som brukes av IRF i Uppsala, ved bl.a. Bo Thidé. Slike mottakere kan kobles til hvilken radar som helst, og vil kunne gi fullstendige profiler av plasmalinjefrekvensen. Utprøving av et slikt instrument på ESR vil kunne gi oss mye nyttig erfaring og ny viten om den polare ionosfære. I denne delen av prosjektet vil det være naturlig å besøke forskere som bruker slike instrumenter allerede.

Et neste steg i prosjektet vil være å utvikle/implementere analyseteknikker som tar hensyn til plasmalinjene. Her vil det være naturlig å samarbeide med de som allerede ser på teoriene bak de merkelig utseende ionespektrene. Det er vanskelig å være for spesifikk her, ettersom det konkrete innholdet i denne delen av prosjektet vil avhenge av hva slags modeller som utvikles for disse dataene i mellomtiden. Ettersom GUISDAP — analyseverktøyet for ESR-data — fremdeles er ustabilt og under stadig endring, er det viktig at jeg i denne og den forrige delen av arbeidet har tilgang på tilstrekkelige og bærbare computerressurser til å behandle og analysere de observasjonene som gjøres.

## 1.3 Original Project Description (English translation)

Tromsø, January 29th, 1999

### 1.3.1 Introduction

The major part of the scattered energy in an incoherent scattering radar is centered within a few kHz of the transmitted frequency, in the so-called ion spectrum or ion line. Most experiments with such radars, including all common programmes of EISCAT, only record the signal from this central part of the spectrum.

The next significant part of the spectrum is called the plasma line. In the same way the ion spectrum corresponds to the ion-acoustic waves, the plasma line corresponds to electrostatic (Langmuir) waves in the plasma. Since the electron density in the ionosphere increases from zero to $10^{12}\,\mathrm{m}^{-3}$, the frequency in the plasma line varies over many MHz. It is therefore difficult to observe.

On the other hand, plasma lines are very interesting to the plasma physicist. The plasma line provides an estimate of e.g. the electron density quite independently of the ion spectrum, and simultaneous observations of up- and down-shifted plasma lines can provide more data independently of the ion spectrum. This data can be used to determine other ordinary ionospheric parameters in the analysis, or to determine the same parameters with better accuracy. Plasma line data can also be used for a more accurate calibration of the ion spectrum analysis than is otherwise possible.

During my Cand. Scient. work, I designed and implemented an experiment for the existing mainland radars with a higher time resolution, a more optimised ion spectrum part for the part of the ionosphere under study, and simultaneous observations of up- and down-shifted plasma lines

### 1.3.2 Continuation into a PhD project

Everything said about plasma lines in the introduction is equally valid for the EISCAT Svalbard Radar (ESR). One observation made already (January 23rd, 1997) shows periods of 5 – 10 min. of calm conditions, separated by shorter periods of very disturbed conditions. During the disturbed periods, we have observed a large number of anomalous echoes with great variability in time and space (altitude). It is increasingly obvious that the simple, Maxwellian explanation which has been so applicable for incoherent scattering up to now is not good enough to describe phenomena seen with the ESR. Many people are already working with these spectra. Plasma line observations will be a great help for deciding how these anomalous echoes can be interpreted, and what physical parameters we can derive from them. We also hope that plasma line data will lead to an understanding of the fine structure seen in the analysed data.

The existing receiver system at the ESR has no provisions for observing plasma lines. The A/D converter has a theoretical bandwidth of approximately 10 MHz, enough to receive the ion spectrum and plasma lines with moderate frequencies, but the effective bandwidth is only about 4 MHz. The plan for making plasma line observations with the ESR is to duplicate the entire receiver, starting with the second IF mixer/amplifier, twice. These will be installed shortly. The new receivers will probably have a larger bandwidth than today's system. With two such modules, both plasma lines can be observed simultaneously and continuously.

None of the existing experiments for the ESR have a plasma line component. It is possible to incorporate an extra modulation in e.g. the current general-purpose gup3 experiment, which covers ranges from 85 to 600 km.

A first step in the project will be to design and implement a first generation plasma line experiment with a single receiver module at the ESR. Attempting observation of both up- and down-shifted plasma lines by changing the centre frequency of the receiving module between pulses will also be of interest. For this part of the project, a longer visit to the ESR will be necessary.

Another interesting idea is to use a purpose-built receiver similar to that developed by F. T. Djuth for use at the Arecibo radar or a modern development of this used at IRF in Uppsala by e.g. Bo Thidé. Such a receiver can be connected to any radar, and will be able to provide complete profiles of the plasma line frequency. Testing such an instrument at the ESR will provide much useful experience and new knowledge of the polar ionosphere. In this part of the project, a visit to scientists working with such instruments already is a natural part.

A next stage in the project will be to develop and implement analysis techniques which take plasma lines into account. In this part, cooperation with those already investigating theories behind the peculiar spectra will be natural. It is difficult to be too specific here, as the concrete contents of this part will depend on what models are developed for these data in the mean time. Since GUISDAP — the analysis tool for ESR data — is still unstable

and in constant flux, it is important that I have access to sufficient and portable computing resources in this and the previous stage for processing and analysing the observations made.

## 1.4 A note on terminology

The term "raw data" is heavily overloaded in ionospheric radar. To the geophysicist, velocities and temperatures may be raw data, while convection and potential patterns are the processed results. In the traditional EISCAT parlance, raw data is range-gated time-averaged correlation or power estimates, while the EISCAT Svalbard Radar and the upgraded EISCAT mainland systems typically produce time-averaged profiles of lagged products, from which range-gated correlation function estimates can be formed in a variety of ways. For some applications, phase information in the received signal is required, and for such applications, the sample stream must be stored in its entirety, whether the samples are broadband (typically band-limited), or as mixed to baseband, filtered and decimated to the bandwidth of the signal.

To avoid this semantic entanglement, the term "raw data" will not be used at all in this thesis. Instead, the following terms and acronyms will be employed.

**Time Series of Voltages (TSV)** is a sequence of samples, stored without integration, but possibly after being mixed to baseband, filtered and decimated to a rate matching the bandwidth of the signal. Provided the signal bandwidth does not exceed the expected value, this form of data contains all information.

**Lag Profile Matrices (LPM)** is time averages of all or some of the lagged products that can be formed from TSV data. In this form, information on the (random) phase is lost, which is why this form of data can be integrated. When alternating codes are discussed, we will sometimes refer to the **result LPM**, which is the LPM consisting of ambiguity-free lagged products which results after the complete code set has been decoded.

**Autocorrelation Functions (ACF)** is when averages of LPM data are formed in such a way that all estimated quantities have similar range contributions. The range resolution obtained after range averaging should match or exceed that defined by the modulation.

For cross-spectrum estimation, we will be using cross-lag profile matrices (XLPM) and cross-correlation function (XCF) estimates. The exact form of these types of data varies with modulation and coding, but these broad categories will serve to distinguish various forms of data.

## 1.5 Plan for remainder of thesis

Chapter 2 discusses briefly the phenomenon of naturally enhanced ion-acoustic echoes. Previously reported observations are summarised, as is the state of the various theoretical explanations suggested for these observations. A discussion of what kind of observations will be most helpful for distinguishing between these explanations is also included.

Chapter 3 describes a plasma line radar experiment created for the EISCAT radars, shows examples of published and unpublished natural and heating-enhanced plasma line observations from the UHF and VHF systems, as well as a new experiment for combined interferometry and plasma line observations for the ESR. Some of the material in this chapter is from (Rietveld *et al.*, 2002, Paper 1).

Chapter 4 introduces the concept of a Software Radar, describes how this relates to the Software Radio idea in communications systems, introduces the MIDAS-W Software Radar prototype (Holt *et al.*, 2000, Paper 2; Grydeland *et al.*, 2003c, Paper 3) as well as the Open Radar Initiative (Lind *et al.*, 2003) and describes the relation between these various projects and ideas and also to related work by other groups.

Chapter 5 explains in some detail how the technological advances presented in chapter 4 have been applied to the study of naturally enhanced ion-acoustic echoes. Particular emphasis is put on the technique of receiver-side interferometry, which has resulted in significant advances in our knowledge of this phenomenon. The spectral estimation technique employed in these observations is explained, and the effect of windowing is discussed. These are the techniques used in Paper 4 (Grydeland *et al.*, 2003b) and presented briefly in Paper 5 (Grydeland *et al.*, 2003a). Some other techniques under development which have not yet produced publishable results are also discussed here.

Chapter 6 shows some observations made using the MIDAS-W software at different radars. Space is mainly given to observations of naturally enhanced ion-acoustic echoes from the EISCAT Svalbard Radar, but examples are also given of observations from the Millstone Hill incoherent scattering radar and the 50 MHz coherent SOUSY Svalbard Radar. More observations are also presented on the accompanying CD-ROM.

Chapter 7 suggests a few directions for future research building on the work presented here. Interferometric techniques have seen decades of development in radio astronomy and equatorial radar, while the use of such techniques for highly dynamic auroral phenomena is in its infancy, and there is much room for improvement.

# Chapter 2

# Enhanced Ion-acoustic Echoes

As incoherent scattering (IS) is an exceedingly weak scattering process, the instruments used to observe such scattering have to be extremely sensitive. With such sensitivity comes a large susceptibility to interference and other sources of noise. One such source is scattering off hard targets in the vicinity of the radar (ground clutter), another one is scattering from hard targets in space. These targets can be active or dead satellites, debris from destroyed space vehicles, or anything else capable of scattering radio waves at the frequency of the radar. As the ionospheric radar scientist is not really interested in these echoes, apart from how to get rid of them, they are commonly referred to as satellites.

Satellites are a serious problem for IS radar, as a satellite can scatter strongly enough to mask the wanted signal, even with the object in a side-lobe with much lower sensitivity or with scattering from several pulses earlier (i.e. with satellites at thousands of kilometres of range.) As a result, IS radars must have effective systems for detecting the presence of satellite echoes in the signal, and to reject or clean contaminated data.

Then, in 1988, reports came from the Millstone Hill observatory (Foster *et al.*, 1988) of echoes found to be of geophysical origin, but which had several points of similarity with satellite echoes. Such echoes had therefore been rejected along with true satellites, which explains how they had escaped previous detection.

Once it was realised that some so-called satellites weren't, similar echoes were also observed at the EISCAT mainland radars (Rietveld *et al.*, 1991) and at the ESR (Buchert *et al.*, 1999). Several theories have been proposed to explain the observations, and although they all undoubtedly have merit, none seem able to explain all observations.

## 2.1 Incoherent Scattering

The expression for the incoherent scattering cross section has been developed by several authors and by many different approaches (e.g. Dougherty and Farley, 1960; Fejer, 1960;

Salpeter, 1960; Hagfors, 1961; Rosenbluth and Rostoker, 1962; Rostoker, 1964). The fact that all of these authors have arrived at the same result by such different methods makes it all the more reasonable that the result is valid under a wide range of conditions. The development is not repeated here, but one of the possible formulations of the result is stated:

$$\begin{aligned} S(\boldsymbol{k},\omega) = & \left|1-\frac{\chi_e}{\epsilon}\right|^2 \int d\boldsymbol{v} f_{0e}(\boldsymbol{v})\delta(\omega-\boldsymbol{k}\cdot\boldsymbol{v}) \\ & + \left|\frac{\chi_e}{\epsilon}\right|^2 \sum_\alpha \frac{n_\alpha}{n_e} z_\alpha^2 \int d\boldsymbol{v} f_{0\alpha}(\boldsymbol{v})\delta(\omega-\boldsymbol{k}\cdot\boldsymbol{v}) \end{aligned} \tag{2.1}$$

where $f_{0\alpha}$ are the background (unperturbed) velocity distribution functions, $z_\alpha$ is the charge number of ion species $\alpha$, and $\chi_e$ and $\chi_\alpha$ are the electron and ion susceptibilities,

$$\chi_\alpha(\boldsymbol{k},\omega) = \frac{\omega_{p\alpha}^2}{k^2} \int \frac{\boldsymbol{k}\cdot\nabla_{\boldsymbol{v}} f_{0\alpha}(\boldsymbol{v})}{\omega-\boldsymbol{k}\cdot\boldsymbol{v}}\, d\boldsymbol{v}, \tag{2.2}$$

and $\epsilon = 1+\chi_e+\sum_\alpha \chi_\alpha$ is the plasma dielectric function. In (2.1), $\boldsymbol{k}$ is decided by the scattering geometry, e.g. for backscattering, $\boldsymbol{k} = -2\boldsymbol{k}_{\text{radar}}$, and $\omega = \omega_s - \omega_{\text{radar}}$ is the shift of the scattered frequency $\omega_s$ from the transmitted frequency $\omega_{\text{radar}}$. The factors before the integrals mean that most of the scattered power is concentrated where $\epsilon$ is small, i.e. near solutions of the plasma dispersion relation. Furthermore, as a threshold of instability is approached, we can expect the scattering levels to increase significantly at the frequency of the unstable oscillation. The term on the first line of (2.1) are governed mainly by the electron dynamic, and results in two narrow spectral lines shifted up and down by the Langmuir frequency, the so-called plasma lines which will be discussed more in chapter 3. The term on the second line is governed by the ion dynamic, and results in scattering from a frequency band centered at the transmitted frequency and with a width determined by the ion-acoustic frequency.

The result is valid for a stable plasma, for radar frequencies much higher than the local plasma frequency, and for radar wavelengths much greater than the local Debye length.

## 2.2 Previous Observations

The first reports of naturally enhanced ion-acoustic echoes were by Foster *et al.* (1988) and Foster (1990), where the Millstone Hill IS radar (42°30′N, 75°W) was seeing enhanced scattering at the edges of the mid-latitude trough. The enhancement was interpreted through destabilisation of the ion-acoustic mode by large flows of thermal electrons known to exist along the edges of the trough. A subsequent little-known publication (Groves *et al.*, 1991) shows the only report to date of similar echoes from the radar at Søndre Strømfjord, Greenland (75° invariant latitude), and an explanation based on excitation of Langmuir waves due to suprathermal electrons interacting nonlinearly with the ion-acoustic waves was introduced.

At EISCAT, similar echoes were also found to occur, (Collis *et al.*, 1991; Rietveld *et al.*, 1991), and these authors also explained their observations in terms of ion-electron two-stream instability. One striking difference between the EISCAT observations and the earlier Millstone Hill observations is that EISCAT commonly sees both ion-acoustic shoulders enhanced well above the thermal level, even when the spectrum is quite asymmetric (Rietveld *et al.*, 1991, fig. 1 and 3, but also Collis *et al.*, 1991, fig. 2), and the stronger enhancement can occur in alternate shoulders for successive 10 s integration periods.

Rietveld *et al.* (1996) conducted a survey of more than 5000 hours of Common Programme data from the EISCAT UHF radar to isolate and categorise the conditions surrounding such observations. They confirmed the range/frequency distribution seen by Rietveld *et al.* (1991), the association with auroral activity, and concluded that none of the proposed theories were able to explain all the features of the observations. Although this survey is concerned with UHF observations, they cite the result that the enhanced echoes occur more often and for longer periods, up to several minutes, at VHF frequencies. Their reported altitude of maximum occurrence is $\sim 500$ km for the UHF radar (933 MHz) and $\sim 800$ km for the VHF radar (224 MHz).

Simultaneous observations at EISCAT UHF and VHF radars were presented by Forme *et al.* (1995), who confirmed the association with enhanced electron temperature, electron precipitation and ion outflow. These authors also observed that the enhancements appeared to be excited more easily at VHF frequencies, and identified a second type of enhanced echoes occurring over smaller range extents, with no associated ion outflow and with both shoulders equally enhanced, sometimes also showing a weak central peak.

Naturally enhanced ion-acoustic echoes have also been observed at the EISCAT Svalbard Radar (ESR). Situated at 78°9′N, 16°2′E, it is in a region often covered by the arctic cusp, meaning that this radar often sees precipitation entering the Earth's ionosphere directly from the solar wind. The operating frequency of 500 MHz places it close to halfway between the mainland EISCAT radars in terms of wavelength. Naturally enhanced ion-acoustic echoes were first reported from the ESR by Buchert *et al.* (1999). Attempts were made to coordinate radar observations with a co-aligned narrow field of view video camera (Sedgemore-Schulthess *et al.*, 1999), while Ogawa *et al.* (2000) and Forme *et al.* (2001) tried to determine whether the enhanced scattering showed a dependence on frequency within the operating range of the radar, a feature which, if observed, would provide evidence in the debate over different explanations. The conclusions of these studies are drawn very carefully, and the studies are obviously limited by the time resolution of the radar.

The observations reported by Rietveld *et al.* (2002), discussed also in section 3.2, were the first reported observations of naturally enhanced ion-acoustic echoes observed together with up- and down-shifted plasma lines. In these observations, plasma lines at an offset not intentionally monitored were scattered into a neighbouring channel, and plasma line spectra are not available. These authors considered this evidence of naturally excited plasma instability.

Important observational evidence was provided by Grydeland *et al.* (2003b), who used very short integrations (200 ms) to eliminate temporal averaging, and an interferometric technique (see sec. 5.1) to resolve spatial structures. They showed examples of enhancements caused by a very localised scattering structure, and of simultaneously observed enhancement in up- and down-shifted ion-acoustic shoulders which in fact was produced simultaneously and in the same volume.

These observations are presented more fully by Grydeland *et al.* (2003a), who show that enhanced echoes often are caused by filamented structure and enhancement of both shoulders in a single volume demonstrated to exist by Grydeland *et al.* (2003b) is the typical situation when both enhanced shoulders can be attributed to a localised structure. Simultaneous observations using a highly sensitive narrow field-of-view video camera showed dynamic and highly structured aurora with tall rays, and a correlation between auroral activity and the intensity in enhanced radar backscattering on sub-second timescales was established for the first time. These authors also discuss the implications of the observed filamentation, and conclude that the increase in scattering cross-section can only be explained through instabilities.

## 2.3 Suggested Theoretical Explanations

We have already touched briefly upon the theories during the presentation of previous observations. In this section, we will try to summarise the proposed theories in sufficient detail that their predicted observables become clear, in particular those observables which distinguish the various theories from each other. A thorough review of the different suggested processes has been given by Sedgemore-Schulthess and St.-Maurice (2001).

The explanations for enhanced ion-acoustic echoes fall into two broad categories; streaming instabilities and production of strong ion-acoustic waves from directly enhanced Langmuir waves through non-linear wave-wave interactions. The streaming instabilities are subdivided into current-driven ion-electron two-stream instability and ion-ion two-stream instability. The Langmuir turbulence explanations generate ion-acoustic waves passively through interference ("beating") between two Langmuir waves, or by conversion of unstable Langmuir waves into ion-acoustic waves modelled by parametric decay or a numeric solution of the Zakharov equations.

### 2.3.1 Ion-electron two-stream instability

We should point out that most studies discussing the ion-electron two-stream instability consider current densities which, while high compared to observations, are still stable for reasonable electron to ion temperature ratios and electron densities. The "destabilisation" discussed in these cases means reduced damping rates, with enhancement in the thermally excited fluctuation levels as a result.

The first reported observations of enhanced ion-acoustic scattering, (Foster *et al.*, 1988), suggested that these echoes were caused by the ion-acoustic wave mode destabilised through a large drift between the thermal populations of electrons and ions, in the form of intense field-aligned currents which span latitudes associated with the mid-latitude trough. Although the average currents are well below those required to cause such enhanced scattering, these authors suggested that the current has become filamented, and support this with satellite observations of current filaments of the order of $100\,\mu\mathrm{A\,m^{-2}}$ (Bythrow *et al.*, 1984). Relative drift between thermal populations of electrons and ions can cause asymmetric enhancement of one or the other ion-acoustic shoulder, depending on the flow direction of the electrons relative to the ions (Rosenbluth and Rostoker, 1962). For typical electron to ion temperature ratios, $T_e/T_i \sim 3$, the asymmetry and enhancement can be considerable even at drifts that are stable to the ion-electron two-stream instability.

This enhancement mechanism was also applied to the first EISCAT observations of enhanced ion-acoustic scattering (Collis *et al.*, 1991; Rietveld *et al.*, 1991). While there is no trough with associated bulk electron flows at EISCAT latitudes, these radars have another source of electron flows: precipitation. Precipitating electrons do not destabilise the ion-acoustic mode directly, but these authors argued that precipitating electrons deposited at a particular altitude of poor perpendicular conductivities would, through charge accumulation, cause an electric field to emerge, whereby the thermal electron population would be caused to drift, predominantly along the magnetic field lines and away from the deposition altitude. Modelling has been able to create such field-aligned flows of thermal electrons in response to electrons precipitating in extremely narrow structures or sharp conductivity gradients (St.-Maurice *et al.*, 1996; Noël *et al.*, 2000), and the fit to observed spectra can be excellent in cases when only one shoulder is enhanced (Collis *et al.*, 1991, fig. 3).

Two problems with this explanation were immediately identified: 1) The currents implied, even when allowing for filamentation, are simply huge. The fitting done by Collis *et al.* (1991) results in current densities of 1–6 $\mathrm{mA\,m^{-2}}$, with one case of $11\,\mathrm{mA\,m^{-2}}$, one to two orders of magnitude larger than what had ever been observed *in situ*. Current densities as large as $300\,\mathrm{mA\,m^{-2}}$ have been observed since then (Stasiewicz *et al.*, 1998), and $500\,\mathrm{mA\,m^{-2}}$ have been modelled (Noël *et al.*, 2000), but the current densities implied by this explanation are still much larger than those observed. 2) Since the theory predicts enhancement of one or the other shoulder, but not both, simultaneous enhancement has to be explained through averaging over periods or volumes of separate up- and down-shifted enhancement. The results presented here and in the papers (Grydeland *et al.*, 2003b,a) suggests that this explanation is incorrect, however.

### 2.3.2 Ion-ion two-stream instability

A different explanation, one which addresses these problems, was proposed by Wahlund *et al.* (1992a). These authors noted that enhanced scattering had been observed in association with strong field-aligned bulk ion outflow (Wahlund *et al.*, 1992b), and that this, combined with high electron temperature and soft electron precipitation, would be favourable

for triggering an ion-ion two-stream instability. The instability occurs when there are different ion species or different populations of the same species with a relative drift of the order of a few thermal speeds of the lighter species. Drift between ions of different mass, they suggested, could be initiated by a non-ambipolar quasi-stationary electric field, and when the instability is triggered, the resulting turbulence causes enhanced resistivity which, in the presence of field-aligned currents, enhance the electric field further. For different populations of the same species, the drift in one of the populations is caused by acceleration elsewhere.

This theory has the desirable qualities that it explains simultaneous enhancement of both ion-acoustic shoulders, and with current densities well within those reported from direct observations. On the other hand, the mechanisms used to produce relative drift between ion species are unlikely to work except in the topside ionosphere, at altitudes of 300–400 km and above. Another objection, raised by Fontaine and Forme (1995), is that this theory will explain a transition from predominantly down-shifted enhancement at lower altitudes to predominantly up-shifted enhancement at higher altitudes, but not the opposite transition, which is more typical for the EISCAT observations. There is a chance that these authors have misinterpreted the simulations by Wahlund *et al.* (1992a), however, as these authors don't state the direction of drifts. The positive Doppler shift in their figure 1 is indication of ion drift towards the observer, so for outward drifting ions, this model does seem to produce predominantly downshifted enhancement for larger drift velocities (larger altitudes), consistent with observations.

The major problem with this explanation is how the different ions are accelerated relative to each other in the first place. A stationary electric field would certainly accelerate the ions, and lighter ions more than heavier, but given the higher mobility of the electrons, it is unclear how such fields can exist for periods long enough to cause significant ion acceleration.

### 2.3.3 Langmuir Turbulence

Groves *et al.* (1991), suggested that the enhanced ion-acoustic scattering was instead caused by the conversion of photoelectron-induced Langmuir waves to ion-acoustic waves by means of non-linear coupling through the ponderomotive force. In this picture, intense, weakly damped Langmuir waves are excited by a suprathermal population of photoelectrons, This alternate explanation is able to explain simultaneous enhancement of the up- and down-shifted shoulders in the same volume. This method also predicts greater enhancements than those obtained using the (stable) ion-electron two-stream mechanism described above. The energy of the suprathermal particles is the main source of free energy for the ion-acoustic fluctuations in this theory, and it does not require unrealistically high values of parameters.

An idea based on similar physics, but with a different source, was suggested by Forme (1993), inspired by non-linear coupling mechanisms known to take place in artificial HF modification (Heating) experiments and some types of solar bursts (Robinson, 1997, and

references therein). In this picture, intense Langmuir waves are excited by fairly low-energy (1–100 eV) precipitating electrons through a "bump-in-tail" instability. The initial, intense Langmuir wave gives rise to a downward propagating ion-acoustic wave and an upward propagating secondary Langmuir wave, a process known as parametric decay. In this initial formulation, only one shoulder would be enhanced. Later refinements of the theory, (Forme, 1999) models the interaction through a numerical solution of the Zakharov equations (Zakharov, 1972), a model which contains parametric decay as well as strong turbulence (cavitation) depending on the strength of the driving. This model allows of both shoulders to be enhanced in a way consistent with the observed range distribution of asymmetries, as illustrated by Forme *et al.* (2001).

In beam modelling, the beam is usually given, and assumed to be modified only weakly with the plasma. To what extent the time- and space-dependent decay of the beam influences the physics in the surrounding plasma has not been modelled, and should be particularly relevant when the beam directly creates instabilities in the surrounding plasma. On the other hand, the quick deterioration of the beam can help explain the short duration of the observed enhanced scattering events.

## 2.4 Observational opportunities for hypothesis testing

When presented with competing, and to some extent conflicting, hypotheses for a given set of observations, we should ask ourselves in what way these hypotheses differ in their predictions. If available observations are unable to provide decisive evidence in favour of or against one or more hypotheses, we should try to obtain such evidence, in the best traditions of science. Of course, production mechanisms may differ from observation to observation, more than one production mechanism may be operating in any given volume, and some of these mechanisms are thought to be triggered by the same conditions, so an absolute rejection of a mechanism may be impossible from such evidence alone. Such evidence might still shed light on previous observations, and bring to light new requirements for the theorists' work.

Let us therefore summarise the features of these hypotheses that lend themselves to testing, in the sense that a given observation would be incompatible with one or more hypotheses.

### 2.4.1 simultaneous enhancement

The ion-electron two-stream instability will explain only one enhanced shoulder at a time, while EISCAT observations typically show both shoulders enhanced over extended spatial regions which could result from separate enhancements averaged together.

Also, observations are typically averaged over a few to many tens of seconds of time, so enhancement of first one shoulder then another could also be averaged together. We will

address these types of averaging in turn. The details of the techniques will be discussed in chapter 5.

#### Very high temporal and spatial resolution

When faced with a phenomenon known to vary on short timescales, deciding on what integration time to use in advance is difficult. For such a study, TSV data is the obvious choice, where integrations can be decided after the fact, and different choices can be tested and compared, as in figure 5.8.

From a philosophical point of view, observations alone cannot really determine that temporal averaging does not take place, arguments based on an understanding of the underlying physics need to complement the observations. In the particular case of the interferometric observations, these are inconsistent with enhancement being produced in many unrelated volumes.

Interferometry also (primarily) provides information about the horizontal scale and position of the scattering structure, but this information is ambiguous. With such information for simultaneously observed enhancements, we can determine whether or not the enhancements are produced in the same volume.

#### Enhancement levels

The only theory which can predict enhancement levels from theoretical considerations is the ion-electron two-stream "instability," for stable situations, that is, near but below the threshold of instability. The enhancement levels are up to about 7 dB. For the ion-electron two-stream instability, enhancements of 1–2 orders of magnitude (computed using linear theory) are reported, but only as indication that strong turbulence must be expected and linear theory is unusable. The theory by Groves *et al.* (1991) use a fluctuation-dissipation simulation to compute about 20 dB of enhancement from reasonable photoelectron fluxes at the Millstone Hill frequency (440 MHz). For the Langmuir Turbulence simulations by Forme (1999), the thermal background fluctuations are not part of the simulation, so it is not possible to compute enhancements over thermal levels from these simulations. For the ion-electron and ion-ion mechanisms in the unstable regime, a turbulence simulation must be made to estimate fluctuation levels, and such studies have, to our knowledge, not been done.

### 2.4.2 Plasma lines

The Langmuir turbulence explanations postulate the existence of intense waves at the local plasma frequency for a broader or narrower range of $\boldsymbol{k}$-vectors. ISR observations where plasma line frequencies are also monitored should be able to observe such Langmuir wave activity, thereby supplying credible evidence in favour of this type of explanation.

### 2.4.3 Other spectral features

The streaming instability mechanisms predict quite regular and well-defined spectral shapes, while Langmuir turbulence, particularly when driven sufficiently hard to excite strong turbulence, can result in features not explained by other theories, e.g. a spectral peak at zero frequency (Forme *et al.*, 1995).

A different example is the argument due to Collis *et al.* (1991) that the spectral lines in their observations are thermally broadened as for a damped mode, not line-like as might be expected from an instability. Others might argue that turbulence would indeed excite wave modes over a broad range of wave vectors and frequencies, and that they could all be strongly enhanced.

This kind of of analysis of details in available observations might provide further clues for an acceptable explanation.

# Chapter 3

# Plasma Line observations

In the same way that the ion spectrum is caused by scattering from ion-acoustic fluctuations, high-frequency electrostatic waves (Langmuir waves) give rise to scattering on frequency shifts near the local plasma frequency, so-called *plasma lines* (Pines and Bohm, 1952; Perkins and Salpeter, 1965; Yngvesson and Perkins, 1968).

For a thermal situation, the scattering cross section due to Langmuir waves is smaller than the scattering in the ion-acoustic spectrum by a factor $k^2\lambda_D^2$, a quantity which must be small for incoherent scattering to occur at all, and plasma lines at the thermal level are usually not detectable. Suprathermal electrons can enhance the mode to a level where the scattering is detectable, (Perkins and Salpeter, 1965; Yngvesson and Perkins, 1968) and the suprathermal electrons can have many sources and be modelled in various ways, e.g. photoelectrons or secondary electrons from precipitation modelled through a power-law distribution (Bjørnå and Trulsen, 1986), a suprathermal flux of secondary electrons caused by precipitating protons (Bjørnå *et al.*, 1982), precipitating electron distribution modelled and computed numerically (Kirkwood *et al.*, 1995), a photoelectron distribution modelled and computed numerically (Guio and Lilensten, 1999) or non-Maxwellian velocity distributions for the electrons (Saito *et al.*, 2000).

As the Langmuir frequency depends mainly on electron density, the existence of plasma lines is useful for determining the background electron density, one of the hardest parameters to calibrate in normal IS radar work. Plasma lines have also been used to determine e.g. photoelectron fluxes (Perkins *et al.*, 1965), electron temperature (Kofman *et al.*, 1981), ion composition (Bjørnå and Kirkwood, 1988), and ion-neutral collision frequencies (Bjørnå, 1989).

The theories of enhanced ion-acoustic fluctuations involving Langmuir waves (Groves *et al.*, 1991; Forme, 1993, 1999) imply that plasma lines should be present and enhanced to an observable level. It is therefore of great interest to make combined ion-line plasma-line observations during periods of enhanced ion-acoustic scattering. One of the earliest known examples of simultaneous observations of enhanced ion-acoustic scattering and strong plasma lines is the experiment analysed by Grydeland (1998). The experiment

used for these observations was intended for inferring ion composition using ion lines and photoelectron enhanced plasma lines (Bjørnå and Kirkwood, 1988). ACFs were computed around zero Doppler for the ion scattering and power profiles computed for six different upshifted plasma line offsets. This application requires stationary conditions, hence the basic time resolution of this experiment was one minute, which makes the observations quite unusable for drawing any conclusions about the enhanced scattering, no matter how fascinating they are.

For the UHF and VHF observations presented here, the experiments used are realisations of the `EPLA2` experiment generation system designed for the EISCAT UHF radar and described in (Grydeland, 1998). This system uses a handful of high-level parameters to generate all the files that were necessary to run a radar experiment on this (now replaced) radar system.

We will present unpublished data from $E$-region plasma line observations taken with the UHF radar in 1998, presented by Grydeland *et al.* (2001a), and observations during artificial ionosphere modification (heating) experiments from 1999, from the UHF and VHF radars, presented on a number of occasions (Rietveld *et al.*, 2000; Isham *et al.*, 2000; La Hoz *et al.*, 2000a,b) and published by Rietveld *et al.* (2002).

## 3.1 Barker-coded alternating code observations of naturally enhanced ion-acoustic and plasma line echoes

For these observations, a 16-bit strong alternating code was used, sub-coded with a 7-bit Barker code. The baud length of the Barker code bauds was 3 $\mu$s, for a range resolution of 450 m, and lags out to 360 $\mu$s covered. A separate Barker-code with the same baud length was also transmitted to provide the zero-lag estimate not available from the alternating code. The Barker code and alternating code is received in three channels, which allows two plasma line offsets to be monitored. In this experiment, these two modulations cover ranges from 89.9 to 123.2 km. In addition, a long pulse modulation with a pulse length of 200 $\mu$s is used to determine background $F$-region plasma parameters, with a coverage from 180 to 414 km and a range resolution of 15.6 km.

Unfortunately, some of the parameters used for these observations were sub-optimal. The 200 $\mu$s long pulse has too little lag coverage for $E$-region and lower $F$-region observations, and the lag coverage in the alternating code is also on the short side.

The 75 minutes shown in figure 3.1 are the only plasma lines seen during 20 hours of experiment run on two different nights of observations, and while there is simultaneous activity in the ion spectra, no examples of enhanced echoes were found.

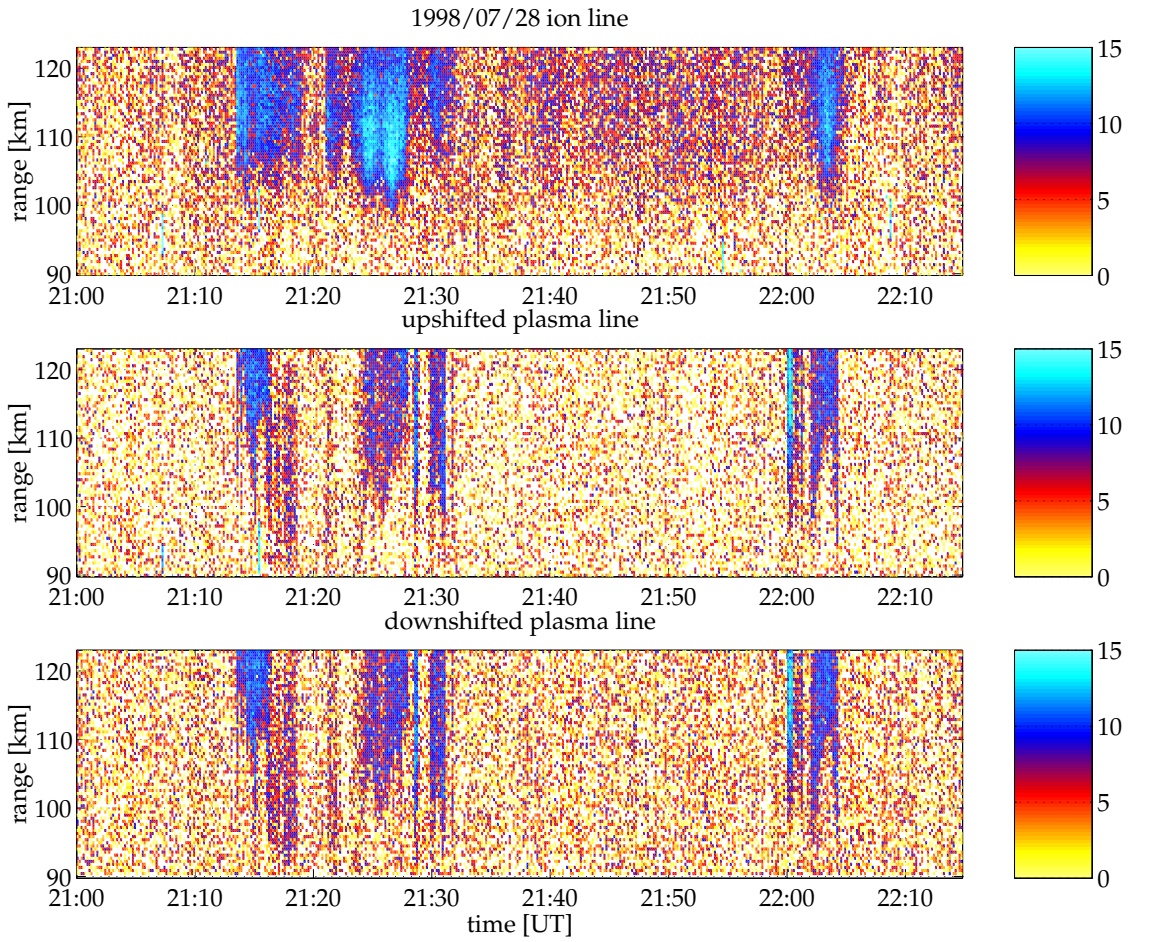


**Figure 3.1:** Power profiles from ion line and up- and down-shifted plasma lines from a Barker-coded alternating code experiment run with the EISCAT UHF radar on 1998-07-28. The plasma line channels were tuned to ±3 MHz.

## 3.2 UHF and VHF heating experiment

The combined ion-line/plasma-line experiment was adapted for the VHF radar and parameters chosen for use in an artificial ionospheric modification (Heating) experiment in 1999. Although artificially induced enhanced ion-acoustic spectra and plasma lines were the purpose of the experiment, naturally enhanced ion-acoustic lines were also observed during this event, together with plasma lines at a plasma line offset not intentionally monitored,

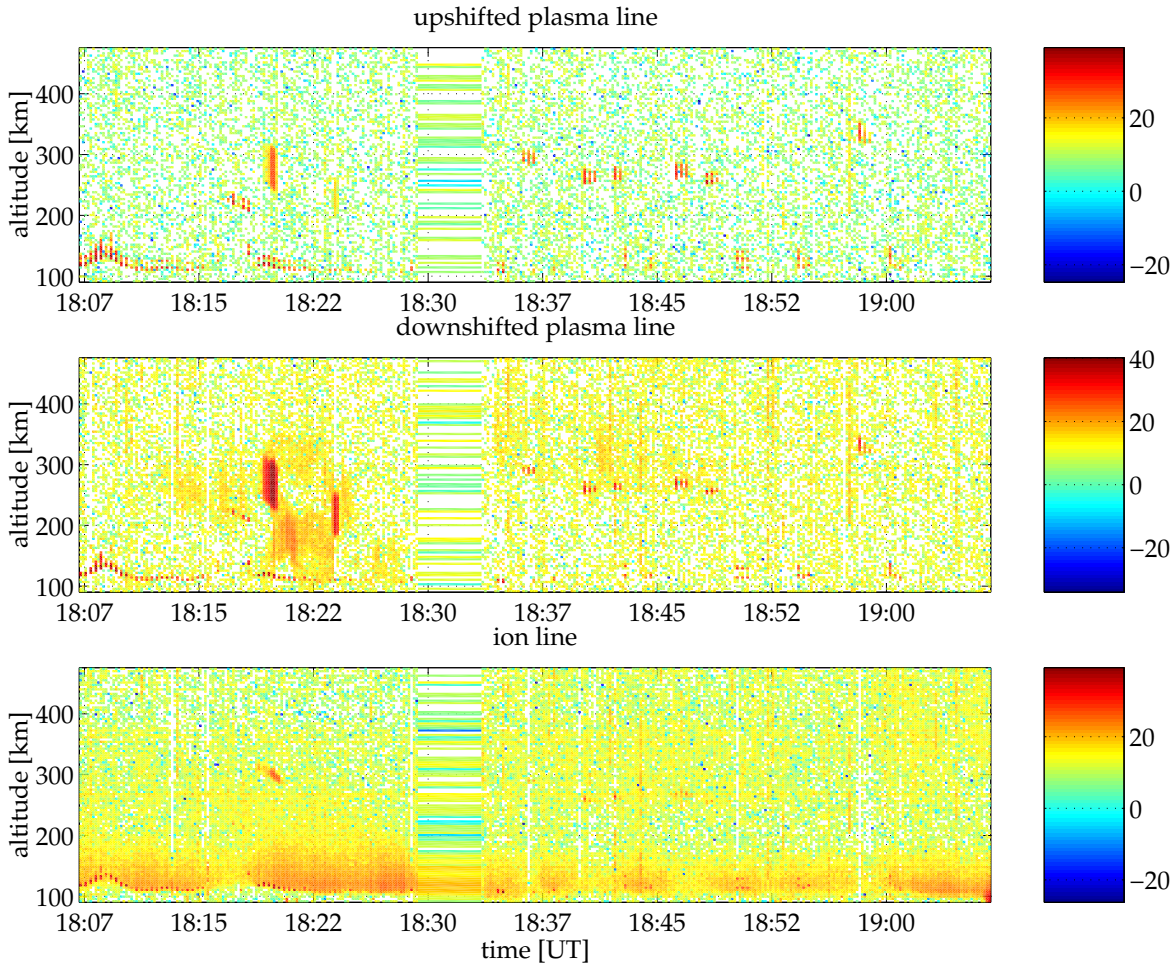


**Figure 3.2:** Power profiles, on a logarithmic scale, from ion line and up- and downshifted plasma lines from an alternating code heating experiment run at the EISCAT VHF radar on 1999-11-11. The even shading between 100 and 200 km in the ion line channel is the *E*-region, the enhanced scattering seen in alternate 10 s integrations in all channels is the heating-induced scattering. After 18:35, scattering is occasionally seen from the topside *E*-region, and the intense scattering after 18:17 is the unintended naturally enhanced scattering discussed in the text. (Rietveld *et al.*, 2002, fig. 1) © COSPAR 2002

but one where plasma line energy from long pulse appeared in channels tuned to receive ion lines and plasma lines from the power profile (short pulse).

For these observations, Barker sub-coding of the alternating code was not required. The alternating code part uses 20 bits of a 32-bit alternating code, with a baud length of 25 $\mu$s,

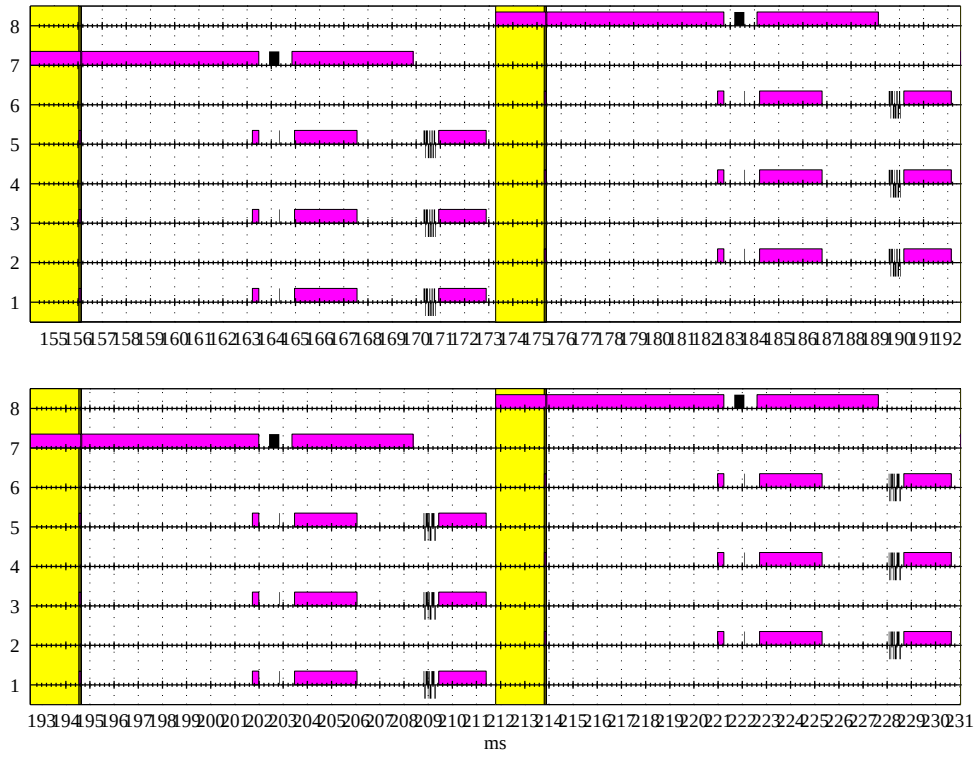


**Figure 3.3:** Timing diagram for the `HPLA2-20` experiment, showing two of the 64 cycles required for the alternating code. Each line corresponds to a specific frequency, black rectangles indicate transmission, pink indicates receiving and yellow indicates calibration noise injection.

for a total pulse length of 500 $\mu$s and a range resolution of 3.75 km. A short pulse of 25 $\mu$s is also transmitted to provide the zero-lag estimate not available from the alternating code. Two plasma line offsets are monitored, as above. In this experiment, the alternating code covers ranges from 90 to 310 km, while the power profile extends the coverage to 475 km. In addition, a long pulse modulation with a pulse length of 420 $\mu$s is used to determine background $F$-region plasma parameters, with a coverage from 180 to 780 km and a range resolution of 31.5 km.

In figure 3.2 is seen power profiles from the EISCAT VHF radar on 1999-11-11, this is essentially the same figure as figure 1 of Rietveld *et al.* (2002). The heater was run in a 10 s on, 10 s off mode, and heater-induced scattering is seen in all channels. The heater frequency is 4.04 MHz, and the plasma line channels are tuned to a centre frequency of 4.03 MHz. The upshifted plasma line channel shows a correlator bug which causes a weak "echo" of scattering four gates (15 km) up from the physical signal.

In all EPLA2 experiments, the entire transmit-receive pattern is repeated on two different sets of frequencies on alternate interpulse periods (IPPs). The long pulse and short pulse are transmitted first, then received, and then one scan of the alternating code set is transmitted and received on the same frequencies used for the short pulse. The cancellation properties of the alternating code means that residual scattering from the short pulse does not show up in the decoded alternating code signal. The timing diagram for the experiment is shown in figure 3.3.

The way the frequencies of the long pulse and short pulse are distributed, causes the channels intended for plasma line power profiles from the short pulse at 4.03 MHz offset to also be sensitive to plasma lines from the long pulse at 3.03 and 5.03 MHz on alternate IPPs. The scattering seen at an apparent altitude of 250 km at 18:17 is in fact naturally enhanced plasma lines from the long pulse at 5.03 MHz. That they are naturally enhanced, and not due to heating, can be deduced by their not following the 10 s on, 10 s off pattern of the heater, and that they are from the long pulse is indicated by their extent, which matches the 420 $\mu$s (63 km) of that pulse. As this scattering is from a different modulation than that used to compute range, the range scale is incorrect for these echoes. The true range of this signal is approximately 65 km lower than the apparent range.

## 3.3 Langmuir Turbulence experiment for the ESR

Based on the very interesting interferometry results obtained with a long pulse experiment (Grydeland *et al.*, 2003b,a), a program intended for combined interferometry and plasma line observations was developed. The program was adapted from an earlier program by Brett Isham for the VHF radar, but significantly expanded and modified for the different hardware of the ESR, with much assistance from Assar Westman. We will describe this program briefly below.

The program is a combined ion-line/plasma line long pulse experiment, suitable for combining with interferometry using a MIDAS-W type receiver (Holt *et al.*, 2000, but also section 4.3) in the ion lines. The block diagram in figure 3.4 shows how a MIDAS-W receiver was connected.

In this program, two long pulses are transmitted every IPP, directly after each other and on different frequencies, each 550 $\mu$s long. Each physical plasma line channel therefore receives two different plasma lines, one from each transmitted frequency. If the plasma line frequency increases with range, the plasma line from the smallest offset will be scattered at the lowest range. Which of the two pulses correspond to high and low offset is different in the up- and down-shifted plasma lines, however. One of the plasma lines therefore causes scattering from the first pulse at the lowest altitude and the second pulse at higher altitude, in which case separating the two signals is easy. For the other plasma line, however, the opposite happens, and the two signals can be caused to overlap in the receiver channel, as discussed by Grydeland (1998). If the Langmuir frequency decreases with range, the two

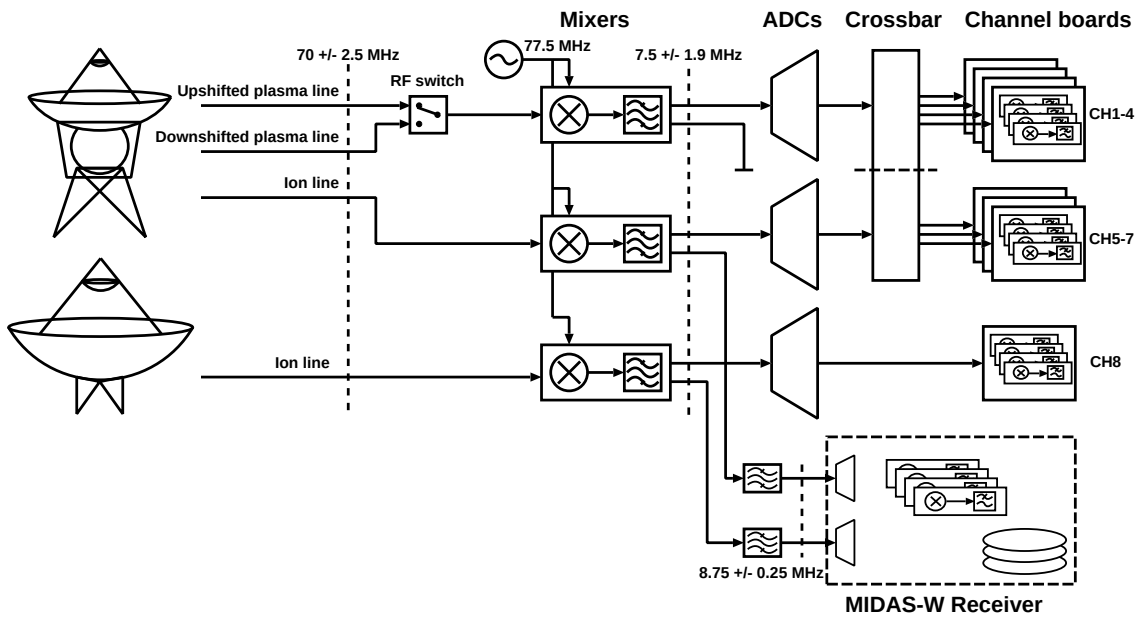


**Figure 3.4:** A block diagram sketch of the ESR analog/digital receiver, how its components are used in the Langmuir Turbulence experiment, and how the MIDAS-W receiver is attached.

plasma lines switch roles. In this experiment, alternating low-high and high-low frequencies are therefore used in alternate IPPs, so that separable plasma lines always are obtained for one of the two IPPs.

When used for interferometry, the 32 m antenna is pointed in the same direction as the 42 m antenna (field-aligned, azimuth = 181.0°, elevation = 81.6°). In the ESR, the 32 m antenna has two wide-band plasma line channels, one for each of the up- and down-shifted plasma lines. Each channel is equal to the ion line channel, centered at a 70 MHz IF and with 5 MHz of bandwidth. The plasma line channels can be set for a "near" setting (centered at $\pm 4$ MHz) or a "far" setting (centered at $\pm 8$ MHz). This gives a total of four 70 MHz IF channels from the two antennas. The ESR only provides three $70 \rightarrow 7.5$ MHz mixers, however, so one mixer must be shared between two of these IF channels. As we intend to do interferometry on the ion line channels, these must have one mixer each all the time. Through a radar-controlled switch, the third mixer is shared between the two plasma line channels. The downshifted plasma line is monitored for two IPPs, then the upshifted for two IPPs.

The ESR has eight channel boards (digital receiver channels). In this experiment, four boards are used to monitor different plasma line offsets, while the remaining four are used for ion spectra and background estimation. Two are used for the two ion line channels from the 32 m antenna, one for background estimation and the last of the four receives the

signal from one of the ion line channels from the 42 m antenna, which lets us verify that this antenna sees the same signal as the 32 m antenna.

With two transmitter frequencies per IPP, we monitor eight different plasma line offsets in each direction. Because of the constraint of placing all four transmitter frequencies within the band sampled by the MIDAS-W receiver, and the design of the analog paths in the ESR receiver, the offsets can only be chosen within certain limits. We have come up with two solutions, one "near" solution, where plasma lines from $\pm 3.375$ to $\pm 4.625$ MHz are monitored, and one "far" solution, with plasma line offsets from $\pm 4.9$ to $\pm 6.6$ MHz.

The ESR signal processing system computes LPMs covering lags every 20 $\mu$s out to 540 $\mu$s for range coverage of 235 to 1650 km. In the plasma line channels, complex baseband TSV data is taken at 10 $\mu$s sampling rate for 100 kHz bandwidth per channel. In addition, an integrated power profile is computed for every plasma line channel. In the MIDAS-W receiver, real bandpass samples are taken in the signal from each antenna at 1 MHz sampling rate for 500 kHz of bandwidth per signal.

### 3.3.1 Observations

The `LT1` experiment has been run for an extended campaign during January of 2003. Naturally enhanced ion-acoustic echoes were observed on two occasions, associated with high coherence at least part of the time, but the plasma line data is inconclusive so far.

All the integrated data (ion line LPMs from 32 and 42 m antennas, and the plasma line power profiles) were affected by the error in data transport described in section 5.5. An example of naturally enhanced ion-acoustic echoes observed during this campaign is shown in figure 5.13.

# Chapter 4

# Software Radar

Simply storing amplitudes from a radar receiver is not new. What makes the approach described in this chapter novel, is the focus on building the receiver-side software in a way which lends itself easily to deployment in many different environments, and in configurations ranging from large production systems in multiple racks of equipment, to portable systems. For this to work, system and software design needs to focus on identifying common properties of radio science systems and scientific radio instrument data handling and processing.

Software Radar can then be described as a philosophy, or a set of guiding principles for system design and integration, and for designing and implementing the software in the system. A striking and practical fundamental property is to bring the signal into the digital domain and under the control of software running on general purpose computers as soon as practically possible, thereby minimising the effort spent on special-purpose equipment and software.

MIDAS-W predates Software Radar. It was the first attempt at producing a workstation-based data acquisition and processing system at Millstone Hill, and it is currently the production system for that radar. MIDAS-W serves as a prototype Software Radar, and a testbed for the Open Radar Initiative.

The Open Radar Initiative is where common development of Software Radar components for the Radio Science community will be coordinated and communicated. For instance, signal processing components from MIDAS-W will be transferred to the Open Radar Initiative when they have matured sufficiently.

MIDAS-W, Software Radar and the Open Radar Initiative has been the subject of several presentations (Grydeland *et al.*, 1999, 2001a; Erickson *et al.*, 2001; Lind *et al.*, 2001; Holt *et al.*, 2001; Grydeland *et al.*, 2001b, e.g.), and has been published, or submitted for publication (Holt *et al.*, 2000; Lind *et al.*, 2003; Grydeland *et al.*, 2003c).

## 4.1 Software Radio, ideas and techniques

The term *Software Radio* was introduced in the early 1990ies to describe a radio where functionality would be provided perhaps 80% by software and 20% by hardware, instead of the inverse ratio typical at that time. A thorough treatment of many aspects to do with the design and implementation of Software Radio systems is given in (Reed, 2002). Software radios need to be flexible, re-programmable, and able to handle different communications protocols and physical frequencies using the same physical hardware under software control. Simply having a Digital Signal Processor (DSP) in a communications device does not turn it into a Software Radio.

As an example, if a design of a portable communications device (such as a cell phone) is implemented using application-specific integrated circuits (ASIC), and a change of functionality (e.g. updated specifications for the communications standard used by the device) is required at the last moment, the entire production could become worthless. If this functionality is implemented in software instead, the change of functionality is obtained through a simple upgrade of software. A next level of flexibility might be imagined where devices detect that its communications partner supports a more recent protocol than the device itself, obtains updated software and upgrades itself while on the air.

In addition to the already mentioned advantages, a software-centered approach leads to radio designs with fewer discrete components, and possibly lower power use. Cost for a single unit does not necessarily diminish, but longer lifetime of a device made possible through software updates might lead to lower total cost of ownership over the device's life.

## 4.2 Radar Application of Software Radio ideas and techniques

There is nothing in the ideas and principles of Software Radio which inherently limits its use to communications applications. The Software Radar idea and the Open Radar Initiative (described below) grew out of the realisation that through the application of selected ideas and techniques from Software Radio, radars and similar radio science instruments could achieve many of the same goals.

Some of the motivations behind Software Radio are not applicable to scientific radio systems. For instance, such instruments rarely have to deal with multiple versions of communications protocols, and they are not currently likely candidates for remote software upgrades.

On the other hand, there are some other properties quite desirable for scientific applications which might be realised quite easily in a software-centric design:

- Independence of underlying hardware. Many radar systems have invested in a particular generation of e.g. signal processing hardware, only to find it impossible to

obtain parts, repairs or compatible replacements just a few years later. With signal processing in software and hardware encapsulated in a device-independent software layer, components which become obsolete or no longer perform as required can be replaced with newer components with whatever differences hidden behind an software interface.

- Relatively painless upgrade paths. As new hardware becomes available, it can replace the older with a minimum of integration, and with processing being done in software running on ordinary workstations, an increase in performance can be obtained through buying a new workstation.
- Coordination of effort. With radar software written with re-usability in mind, it is conceivable that the same software can be used for multiple instruments. In foreseeable future, the investments in software for radio instruments can benefit from software which has already been developed, and further developments can be contributed back to the community.

## 4.3 The MIDAS-W Software Radar prototype

MIDAS-W (W for Workstation) actually predates the Open Radar Initiative. It grew out of a need for an upgrade to the Millstone Hill Incoherent Scatter Data Acquisition System (MIDAS), and a realisation that off-the-shelf analog-to-digital converters (ADCs) and workstations had become sufficiently capable that the data taking and processing requirements of IS radar could be met by a commercially available ADC board mounted in an ordinary workstation and with all processing implemented in software (Holt *et al.*, 2000).

After an initial demonstration of the MIDAS-W architecture, an effort to produce a production quality system resulted in the replacement of the MIDAS-1 system (and its custom built signal processing hardware) ahead of schedule in November of 2001. Since this time, MIDAS-W has been the production data acquisition and control system for the Millstone Hill Incoherent Scatter radar.

## 4.4 The Open Radar Initiative

The Open Radar Initiative (Lind *et al.*, 2003) is an effort to develop reliable and reusable hardware and software to support scientific applications of radar and radio science related technology. A major goal of the initiative is to provide the technological elements of Software Radar systems as well tested and highly modular software and hardware elements. This modularity will aid the implementation of other experimental radio science systems.

The Open Radar Initiative is coordinated through the web site

`http://www.openradar.org/`

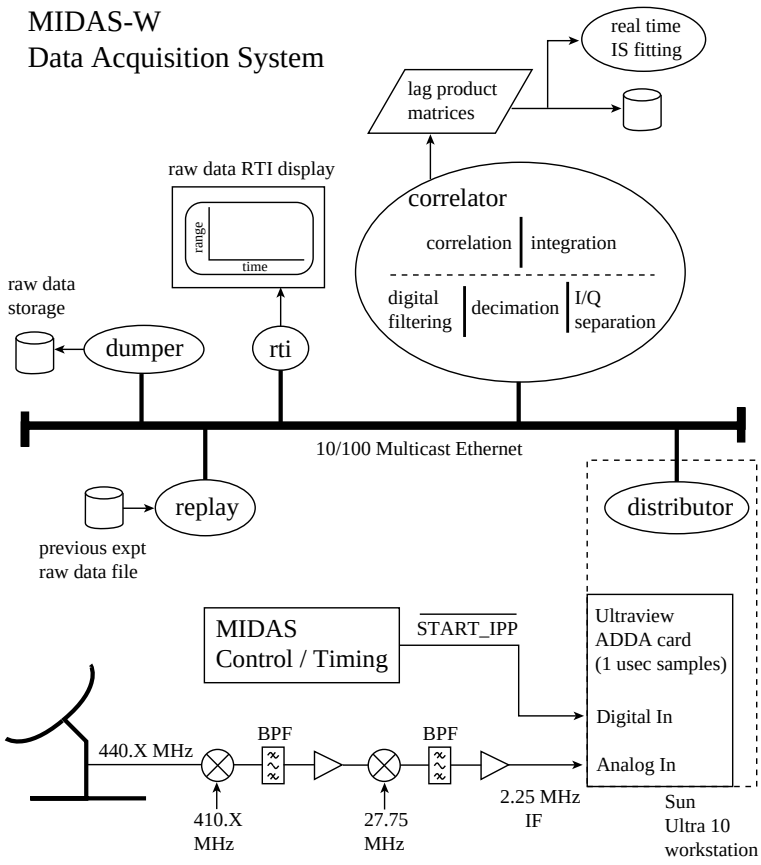


**Figure 4.1:** Simplified block diagram of a MIDAS-W Software Radar prototype, as used at Millstone Hill during its initial deployment and testing (Holt *et al.*, 2000, fig. 6) © EGS – Springer-Verlag 2000

### 4.4.1 Network Architecture and signal channels

A thorough discussion of the network architecture of a general Software Radar system and its implications is beyond the scope of this thesis, a fuller presentation is given in (Grydeland *et al.*, 2003c, Paper 4) with a brief summary given below. We will instead take a close look at some of the components that make up a signal processing

A Software Radar system is a virtual entity distributed among computing elements and connected by a high speed communications network. Multicast communication can be used over this network to enable a high degree of parallelism in data management, control, and system monitoring. For convenience multicast traffic can be separated into multiple *channels* which may bridge multiple physical networks and where each channel is allocated to handle a particular type of traffic.

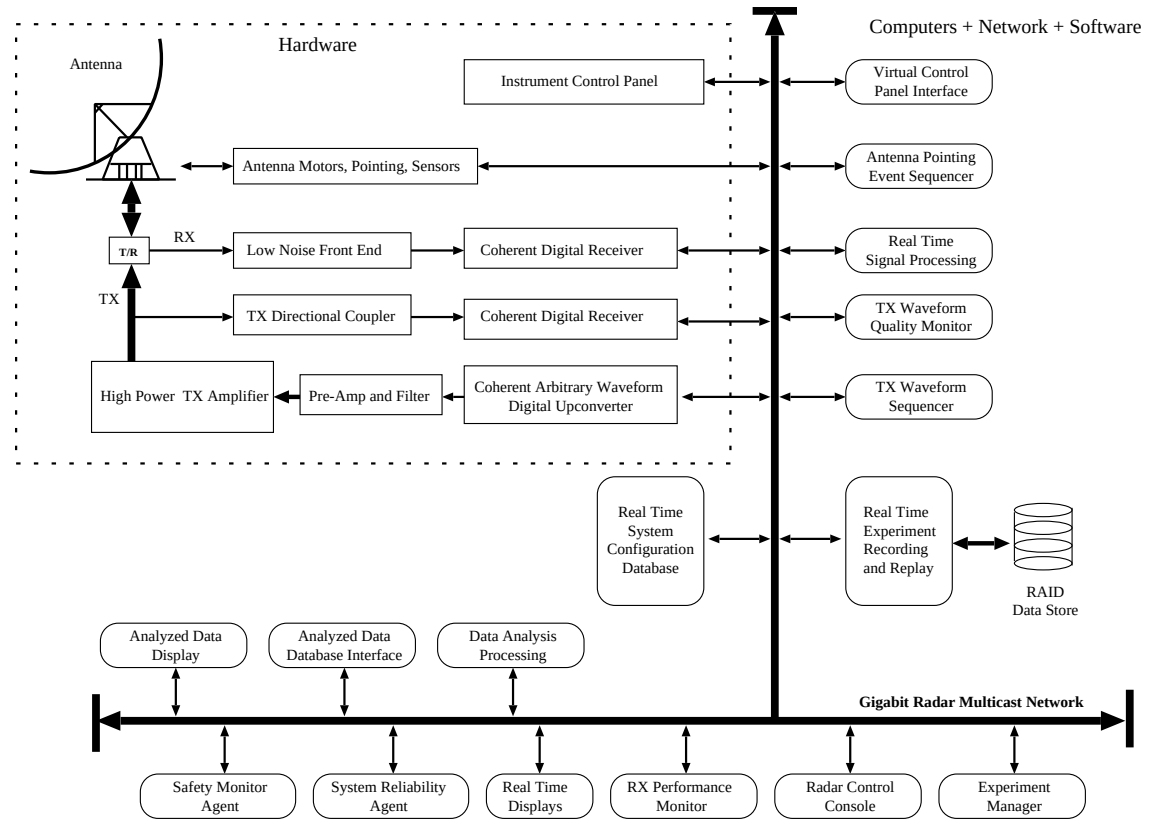


**Figure 4.2:** Simplified block diagram for a production Software Radar system

A typical set of channels found in a Software Radar system include one or more control, data, status, profiling, and debugging channels. Channels can be persistently or dynamically allocated depending on the particular requirements of the system. A series of *patterns* are used to interact with the channels in standardized ways. These patterns correspond to strategies for solving recurring problems and their software implementation (Gamma *et al.*, 1994). A simplified block diagram of what a production Software Radar system might look like at a steerable IS Radar facility is shown in figure 4.2.

### 4.4.2 Signal processing components

While software-centric solutions offer higher flexibility and reconfigurability, they also mean that many levels of computation previously implemented in hardware now must be available as software.

### Digital receiver software

Signals must be at baseband (centered at zero frequency) for correlation estimation, but sampling is often done off-baseband to avoid the complication of achieving perfectly matched real and imaginary (I and Q) analog paths. Mixing the signal to baseband, filtering and decimation must then be done numerically. Some data acquisition hardware includes a first-stage digital receiver, but otherwise, this function must be performed in software.

For this purpose, we have implemented software modules implementing the functions of a numerical oscillator (NCO), mixing, digital FIR filtering and decimation. A hardware digital filter typically produces every mixed sample before decimation throws out all but one in $N$ filtered samples. In a software implementation, it is better to compute only the results which will be required, so filtering and decimation is a single operation. The mixing and filtering/decimation components are capable of dealing with purely real or complex signals, real or complex filter coefficients, and any integer decimation can be performed.

### Correlation estimation

In Incoherent scatter radar, the details of the spectral power distribution of the scattering process is usually obtained by way of the autocorrelation function (ACF) of the scattered signal (Farley, 1969). Section 5.2, and to some extent 5.4, discusses spectral estimation using such techniques, while this section deals with details of the signal processing and how it has been implemented in the Software Radar components.

The best way of forming integrated correlation estimates for most incoherent scatter applications is through a *lag profile matrix* (LPM) (Turunen, 1986; Wannberg, 1993, called UNIPROG (UNIversal PROGram) in the earlier references). The complex baseband sample vector is multiplied with its own complex conjugate at all desired lag increments. The lagged product does not contain a random phase, and can be integrated (summed). If desired, autocorrelation function estimates can then be formed by making suitable sums along the diagonals of this matrix for groups of lagged products with the same or similar spatial contributions (Turunen and Silén, 1984), and section 5.2 in this thesis.

LPM computations are useful for all currently employed incoherent scatter techniques for ionospheric observations, and in most cases, only a little post-processing separates the different modulations from a signal processing point of view. For alternating codes, LPMs are formed separately for each modulation. At the end of integration, all intermediate LPMs are decoded and summed to a result LPM. The decoding stage consists of applying a ($\pm 1$) FIR filter generated from the code along each lag profile (Huuskonen *et al.*, 1996). For random (Sulzer, 1986) and deterministic (Lehtinen and Häggström, 1987; Lehtinen *et al.*, 1997) alternating codes (but *not* for the alternating codes discovered by Sulzer (1993)), every decoded lagged product is ambiguity-free, so partial gates with fewer lags (but worse statistics) can be computed before and after the first and last complete gate. In practice, only the partial gates before the first complete gate are of interest.

When alternating codes are oversampled — called *fractional lags* by Huuskonen *et al.* (1996) — each integrated lag profile for the non-integer lags can be decoded in two different ways. The resulting lag profiles have slightly different range contributions, so for optimal analysis they should be considered separately.

In multi-pulse codes and alternating codes (all flavours), the zero-lag profile is ambiguous in range, and has traditionally been discarded or been used only for channel balancing (Turunen and Silén, 1984). As discussed by Lehtinen and Huuskonen (1986), this ambiguous data can be useful when inversion methods are employed, so in our implementation, the zero lag profile is always computed. For power profiles, an LPM with a single (zero) lag is used.

A parametrised LPM processing module capable of computing the LPMs for all of these modulations has been written, complete with post-processing methods for alternating codes and extraction of an ACF matrix from the LPM using several different summation rules. The module is also capable of cross-lag profile matrix (XLPM) processing and extraction of a cross-correlation function (XCF) matrix for interferometry. All power spectra and interferometry examples shown in this thesis and in the articles (Holt *et al.*, 2000; Grydeland *et al.*, 2003a,b,c) have been processed using this module.

## 4.5 Related work

A portable, high-speed data collection system was used for observing the entire plasma line profile at Arecibo in 1991 (Djuth *et al.*, 1994). The spectral shape of the plasma line profile was measured using a random alternating code, called a Coded Long Pulse (CLP) by these authors (Sulzer, 1986). The signal was sampled at 5 MHz, with 8-bit complex samples, and the IPP had to be lengthened to more than 5 times that required by duty cycle limitations to reduce data rates. Signal processing was done off-line, but along the same lines as one would expect to see for real-time processing.

A similar system was used for the CRRES AA2 release experiment in 1992 (Djuth *et al.*, 1995) where the interaction between a high-power HF beam and a high ion mass plasma was studied, using ion and plasma line profiles measured from Arecibo. Here, TSV data was collected for the entire experimental period $\sim 45$ min, and the authors comment on how this enabled them to optimize integration periods and signal processing techniques as desired, as well as letting them examine radar returns on a pulse-by-pulse basis.

A group from Sodankylä geophysical observatory and the University of Oulu is also taking TSV data at the ESR, using a combination of a spectrum analyzer, a programmable I/O card and a desktop computer with large hard disks (Lehtinen *et al.*, 2002; Damtie *et al.*, 2002). These authors use off-line processing to implement new pulse coding schemes, where unambiguous lag profiles are computed from the ambiguous profiles measured in the experiment through statistical inversion methods.

# Chapter 5

# Interferometry and other Techniques

For the purpose of resolving any temporal or spatial averaging, and for extracting all the useful information from the acquired data, a number of techniques have been employed, the receiver-side interferometry discussed in two of the papers (Grydeland *et al.* (2003b, Paper 3) and Grydeland *et al.* (2003a, Paper 4)), being the most crucial.

In this chapter, the interferometric technique and some of the other techniques also employed are presented in a bit more detail than is appropriate for journal publication. Some of the alternate approaches that never made their way into the published papers are also explored, as well as some techniques that have been developed, and which will be used in the future.

## 5.1 Interferometry for horizontal resolution

With TSV data from two phase-coherent receivers, there is the opportunity of detecting small-scale structures using an interferometric technique. The technique is in principle the same as that used by (Farley *et al.*, 1981) to infer velocities of travelling eddies in the equatorial electrojet, although the geophysical phenomenon under study is quite different. In this and related publications, (e.g. Kudeki *et al.*, 1999; Chau and Woodman, 2001b), a simple expression for the coherence is used. When the width of the scatterer is not negligible compared to the antenna beam width, or the receiving antennas have different beam patterns, a more careful treatment of the effect of antenna beam patterns, leading to a more complicated expression, might be necessary. As the observations will be used to infer horizontal size, this investigation is carried out.

Another difference between these previously employed techniques and the one used here is that previous techniques have computed the power spectra and cross-spectra required through direct Discrete Fourier Transform (DFT) techniques, while here, the LPM technique used for ACF estimation uses two different signals, and has been extended to also cover negative lags, and this has been used for cross-correlation function (XCF) estimation. See section 5.2 for details on the processing.

### 5.1.1 The received signals

Consider a radar system with two unequal antennas separated by a distance greater than the wavelength of the radar, but much smaller than the distance to a scattering volume to be investigated using this system. One antenna is used for transmitting and receiving, indicated by the subscript tx, and the other for receiving only, indicated by the subscript rx. Define a coordinate system with its centre in the transmitting antenna, pointing in the $z$ direction, and express all linear spatial coordinates in units of wavelength. The discussion is limited to the far field of the antennas, whereby integrations over apertures are performed by multiplying with antenna gain patterns, denoted by $G_{\mathrm{tx}}(x/z, y/z)$ and $G_{\mathrm{rx}}(x/z, y/z)$, respectively, and phase is computed from the centre point of the antenna.

The spatial part of the electric field incident on the scattering volume is given by

$$E_{\mathrm{inc}} = \frac{E_0 R_0}{R} G_{\mathrm{tx}}(x/z, y/z) \exp[-2\pi i R] \tag{5.1}$$

where $R = \sqrt{x^2 + y^2 + z^2}$ is the distance from the transmitting antenna and $E_0$ is the field at an arbitrary distance $R_0$. The source term for the scattering is obtained by multiplying this field with a term which is proportional to the electron density fluctuation, which is denoted by $C \cdot n(x, y, z)$. Using the unmodified incident field in this expression is to assume weak scattering, also known as the Born approximation. The constant $C$ describes the scattering strength of the medium and includes among others the scattering cross section of an electron and the factor $E_0 R_0$ from equation (5.1).

The spatial part of the scattered field in the aperture plane $z = 0$ is given by

$$E_{\mathrm{sc}}(x, y) = C \iiint \frac{1}{R'} E_{\mathrm{inc}}(x', y', z')\, n(x', y', z')\, g(z' - Z_0) e^{-2\pi i |\boldsymbol{R}' - \boldsymbol{r}|} dx'\, dy'\, dz' \tag{5.2}$$

where $g(z)$ is a spatial weighting function centered at 0 due to the modulation pattern and impulse response of the radar receiver, $\boldsymbol{r} = (x, y)$ is the position in the aperture plane for which the field is computed, and $|\boldsymbol{R}' - \boldsymbol{r}| = \sqrt{(x' - x)^2 + (y' - y)^2 + z'^2}$ is the distance from the scattering volume element to the point in the aperture plane.

Next, observe that since $g(z)$ is local, and $Z_0 \ggg 1, x, y$, then $1/z$, $x/z$ and $y/z$ are approximately constant over the volume being considered, except when used for phase purposes. We can also make the approximations

$$R = z\sqrt{1 + (x^2 + y^2)/z^2} \approx z(1 + (x^2 + y^2)/2z^2) = z + (x^2 + y^2)/2z \tag{5.3}$$

and

$$|\boldsymbol{R}' - \boldsymbol{r}| \approx z + (x'^2 + y'^2 + x^2 + y^2 - 2xx' - 2yy')/2z. \tag{5.4}$$

Insert (5.1) in (5.2), and define

$$n_k(x, y; Z_0) = \int n(x, y, z) g(z - Z_0) e^{-4\pi i z} dz, \tag{5.5}$$

which expresses the selection on $k$ which occurs for backscattering, that is, scattering in the direction of the transmitter. We now obtain

$$E_{\rm sc}(x,y) = \frac{C}{Z_0^2}\iint dx'\,dy'\,G_{\rm tx}(x'/Z_0, y'/Z_0)n_k(x',y';Z_0) \\ \exp\left[-2\pi i\frac{x'^2+y'^2}{Z_0}\right]\exp\left[2\pi i\frac{xx'+yy'}{Z_0}\right]\exp\left[-2\pi i\frac{x^2+y^2}{2Z_0}\right] \qquad (5.6)$$

The received signals in an arbitrary antenna on the ground can now be found by integrating this field over the antenna aperture, or equivalently, by multiplying the expression under the integrals in (5.6) with gain pattern of the receiving antenna.

Different elementary volumes contribute to the integral with different phase, so the integration over scattering volume is still necessary.

The received signal in the transmitting antenna ($\boldsymbol{r} = \mathbf{0}$) is given by

$$f_{\rm tx} = \frac{C}{Z_0^2}\iint n_k(x',y';Z_0)G_{\rm tx}^2 e^{-2\pi i(x'^2+y'^2)/Z_0}dx'\,dy' \qquad (5.7)$$

In the receive-only antenna, with gain pattern $G_{\rm rx}$ and displaced a distance $\boldsymbol{r} = (A,0)$, the signal is

$$f_{\rm rx} = \frac{C}{Z_0^2}\iint n_k(x',y';Z_0)G_{\rm tx}G_{\rm rx}e^{-2\pi i(x'^2+y'^2-Ax'+A^2/2)/Z_0}dx'\,dy'. \qquad (5.8)$$

### 5.1.2 Cross-correlations and autocorrelations

From expressions (5.7) and (5.8), form the cross-product and ensemble average, which gives an expression for the complex spatial cross-correlation of the scattering received in the two antennas:

$$\langle f_{\rm tx}f_{\rm rx}^*\rangle = \frac{C^2}{Z_0^4}\iiiint \langle n_k(x,y;Z_0)n_k^*(x',y';Z_0)\rangle \\ G_{\rm tx}^2(x/Z_0,y/Z_0)G_{\rm tx}(x'/Z_0,y'/Z_0)G_{\rm rx}(x'/Z_0,y'/Z_0) \\ e^{-2\pi i(x^2-x'^2+y^2-y'^2+Ax'-A^2/2)/Z_0}dx\,dy\,dx'\,dy' \qquad (5.9)$$

The constant phase factor $\exp(i\pi A^2/Z_0)$ is due to the asymmetry between the transmitting and receiving antennas. It is of no interest and is discarded.

Next, assume spatial stationarity; that the spatial correlations depend only on distance within the scattering volume, not on absolute position. This assumption needs to hold on the spatial scales that define the scattering (a few Debye lengths), but it does not need to hold across the entire scattering volume.

$$\langle n_k(x,y;Z_0)n_k^*(x',y';Z_0)\rangle = \left\langle|\Delta n|^2\right\rangle\delta(x-x')\delta(y-y') \qquad (5.10)$$

Introduce the angles of integration

$$\theta_x = x/Z_0, \quad \theta_y = y/Z_0 \tag{5.11}$$

and obtain

$$\langle f_{\rm tx} f_{\rm rx}^* \rangle = \frac{C^2}{Z_0^2} \iint \left\langle |\Delta n(\theta_x, \theta_y)|^2 \right\rangle G_{\rm tx}^3(\theta_x, \theta_x) G_{\rm rx}(\theta_x, \theta_x) e^{-2\pi i A \theta_x} d\theta_x \, d\theta_y \tag{5.12}$$

Expressions are obtained for the spatial auto-correlations in each of the antennas in a similar way:

$$\langle |f_{\rm tx}|^2 \rangle = \frac{C^2}{Z_0^2} \iint \left\langle |\Delta n(\theta_x, \theta_y)|^2 \right\rangle G_{\rm tx}^4(\theta_x, \theta_x) \, d\theta_x \, d\theta_y \tag{5.13}$$

and

$$\langle |f_{\rm rx}|^2 \rangle = \frac{C^2}{Z_0^2} \iint \left\langle |\Delta n(\theta_x, \theta_y)|^2 \right\rangle G_{\rm tx}^2(\theta_x, \theta_x) G_{\rm rx}^2(\theta_x, \theta_x) \, d\theta_x \, d\theta_y \tag{5.14}$$

and the observable coherence is obtained through normalising (5.12) by the geometrical mean of (5.13) and (5.14),

$$\rho = \frac{\langle f_{\rm tx} f_{\rm rx}^* \rangle}{\sqrt{\langle |f_{\rm tx}|^2 \rangle \langle |f_{\rm rx}|^2 \rangle}} \tag{5.15}$$

### 5.1.3 Wide antenna beams

Assume for mathematical convenience that a discrete scattering structure has a Gaussian shape centered at $(\theta_{xo}, \theta_{yo})$ with unequal widths in the $x$- and $y$-directions, $\sigma_x$ and $\sigma_y$ respectively:

$$\left\langle |\Delta n(\theta_x, \theta_y)|^2 \right\rangle = \exp\left[ -\frac{(\theta_x - \theta_{xo})^2}{2\sigma_x^2} - \frac{(\theta_y - \theta_{yo})^2}{2\sigma_y^2} \right] \tag{5.16}$$

and that the antenna beams are much wider than the scatterer. In this limit, the antenna gains in expressions (5.12), (5.13) and (5.14) can be replaced with the gains in the direction of the centre of the scatterer, and taken outside the integrals, where they will eventually disappear in the normalisation at (5.15). When equation (5.16) is inserted in (5.12), the integral over $\theta_x$ becomes

$$\begin{aligned} \langle f_{\rm tx} f_{\rm rx}^* \rangle &\propto \int \exp\left[ -\frac{(\theta_x - \theta_{xo})^2}{2\sigma_x^2} - 2\pi i A \theta_x \right] d\theta_x \\ &= \sqrt{2\pi}\sigma_x e^{-2\pi i A \theta_{xo}} \exp\left[ -\frac{1}{2}(2\pi A)^2 \sigma_x^2 \right] \end{aligned} \tag{5.17}$$

while the integration over $\theta_y$ in (5.12) and over $\theta_x$ and $\theta_y$ in (5.13) and (5.14) are even simpler. The resulting complex cross-correlation becomes

$$\langle f_{\rm tx} f_{\rm rx}^* \rangle = G_{\rm tx}^3(\theta_{xo}, \theta_{yo}) G_{\rm rx}(\theta_{xo}, \theta_{yo}) \frac{C^2}{Z_0^2} 2\pi\sigma_x\sigma_y e^{-2\pi i A\theta_{xo}} \exp\left[-\frac{1}{2}(2\pi A)^2\sigma_x^2\right] \quad (5.18)$$

And the spatial auto-correlation in each antenna is

$$\langle |f_{\rm tx}|^2 \rangle = G_{\rm tx}^4(\theta_{xo}, \theta_{yo}) \frac{C^2}{Z_0^2} 2\pi\sigma_x\sigma_y \quad (5.19)$$

$$\langle |f_{\rm rx}|^2 \rangle = G_{\rm tx}^2(\theta_{xo}, \theta_{yo}) G_{\rm rx}^2(\theta_{xo}, \theta_{yo}) \frac{C^2}{Z_0^2} 2\pi\sigma_x\sigma_y, \quad (5.20)$$

which gives the following simple expression for coherence:

$$\rho = e^{-2\pi i A\theta_{xo}} \exp\left[-\frac{1}{2}(2\pi A)^2\sigma_x^2\right] \quad (5.21)$$

This result is equivalent to equation (8) in Farley *et al.* (1981). From this expression, the interferometry *fringe size* is defined as $1/A$, the angular distance which corresponds to a phase shift of $2\pi$.

A similar result will arise from any sort of localised scattering structure, as long as it is much narrower than the antenna beams.

### 5.1.4 Gaussian antennas

Next, assume Gaussian patterns for the two antennas

$$G_{\rm tx,rx}(\theta_x, \theta_y) = \exp\left[-\frac{\theta_x^2 + \theta_y^2}{2\sigma_{\rm tx,rx}}\right] \quad (5.22)$$

and the Gaussian expression (5.16) will again be used for the scatterer. Inserting these expressions in (5.12) and reorganising terms produces

$$\begin{aligned}\langle f_{\rm tx} f_{\rm rx}^* \rangle = \frac{C^2}{Z_0^2} & e^{-\theta_{xo}^2/2\sigma_x^2} e^{-\theta_{yo}^2/2\sigma_y^2} \\ & \times \int \exp\left[-\frac{1}{2}\frac{\theta_x^2}{D_x^2} + 2\left(\frac{\theta_{xo}}{2\sigma_x^2} - i\pi A\right)\theta_x\right] d\theta_x \\ & \times \int \exp\left[-\frac{1}{2}\frac{\theta_y^2}{D_y^2} + 2\left(\frac{\theta_{yo}}{2\sigma_y^2}\right)\theta_y\right] d\theta_y \end{aligned} \quad (5.23)$$

where

$$\frac{1}{\Sigma^2} = \frac{3}{\sigma_{\rm tx}^2} + \frac{1}{\sigma_{\rm rx}^2}, \qquad \frac{1}{D_{x,y}^2} = \frac{1}{\Sigma^2} + \frac{1}{\sigma_{x,y}^2}, \quad (5.24)$$

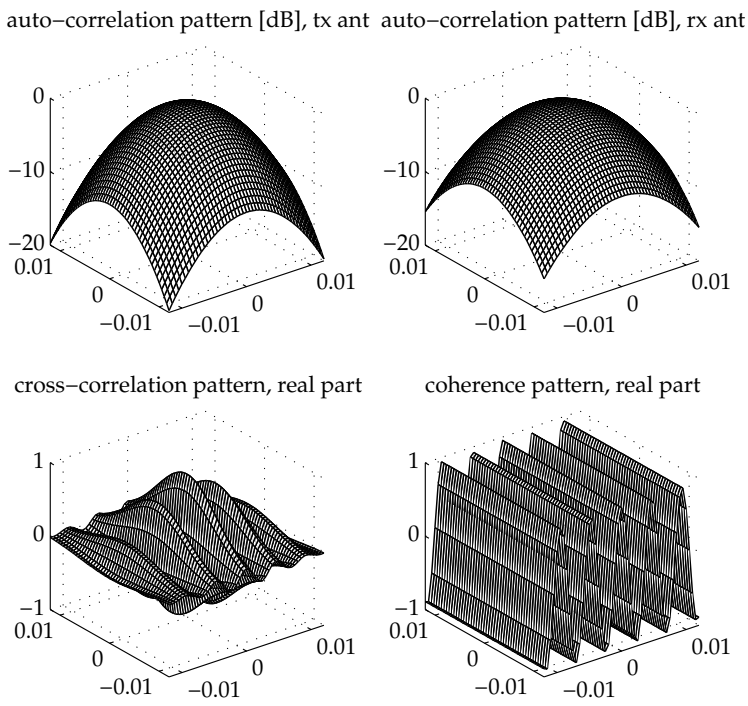


**Figure 5.1:** The correlations induced by a Gaussian scatterer with half width 1/10 fringe size as it is placed in different positions within the antenna beams. From top to bottom left to right, the panels show a) $\langle |f_{\rm tx}|^2 \rangle$, equation (5.13) inserted (5.22), b) $\langle |f_{\rm rx}|^2 \rangle$, equation (5.14) inserted (5.22), c) $\langle f_{\rm tx} f_{\rm rx}^* \rangle$, equation (5.25), d) $\rho$, equation (5.29). The antenna separation and beam widths are for the ESR.

Here, the integrals over $\theta_{x,y}$ have been put in a form found in tables, and the resulting complex cross-correlation is

$$\begin{aligned}\langle f_{\rm tx} f_{\rm rx}^* \rangle &= \frac{C^2}{Z_0^2}\, 2\pi D_x D_y \exp\left[-\frac{1}{2}\frac{D_y^2}{\Sigma^2}\frac{\theta_{yo}^2}{\sigma_y^2}\right] \times \exp\left[-2\pi i A \theta_{x0}\frac{D_x^2}{\sigma_x^2}\right] \\ &\quad \times \exp\left[-\frac{1}{2}D_x^2\left(\frac{1}{\Sigma^2}\frac{\theta_{x0}^2}{\sigma_x^2} + (2\pi A)^2\right)\right] \\ &= \frac{C^2}{Z_0^2}\, \exp\left[-\frac{1}{2}\frac{D_x^2}{\Sigma^2}\frac{\theta_{xo}^2}{\sigma_x^2} - \frac{1}{2}\frac{D_y^2}{\Sigma^2}\frac{\theta_{yo}^2}{\sigma_y^2}\right] \\ &\quad \times \exp\left[-\frac{1}{2}(2\pi A)^2 D_x^2\right] e^{-2\pi i A \theta_{xo} D_x^2/\sigma_x^2} \end{aligned} \tag{5.25}$$

Note the change of sign for the $(2\pi A)^2$ term from that published in Grydeland *et al.* (2003b). Similarly, the spatial auto-correlation in each antenna becomes

$$\langle |f_{\rm tx}|^2 \rangle = \frac{C^2}{Z_0^2} 2\pi D_x D_y \exp\left[-\frac{1}{2}\frac{D_{{\rm tx},y}^2}{\Sigma_{\rm tx}^2}\frac{\theta_{y0}^2}{\sigma_y^2}\right] \exp\left[-\frac{1}{2}\frac{D_{{\rm tx},x}^2}{\Sigma_{\rm tx}^2}\frac{\theta_{x0}^2}{\sigma_x^2}\right] \tag{5.26}$$

and

$$\langle |f_{\rm rx}|^2 \rangle = \frac{C^2}{Z_0^2} 2\pi D_x D_y \exp\left[-\frac{1}{2}\frac{D_{{\rm rx},y}^2}{\Sigma_{\rm rx}^2}\frac{\theta_{y0}^2}{\sigma_y^2}\right] \exp\left[-\frac{1}{2}\frac{D_{{\rm rx},x}^2}{\Sigma_{\rm rx}^2}\frac{\theta_{x0}^2}{\sigma_x^2}\right] \tag{5.27}$$

where

$$\frac{1}{\Sigma_{\rm tx}^2} = \frac{4}{\sigma_{\rm tx}^2}, \qquad \frac{1}{\Sigma_{\rm rx}^2} = \frac{2}{\sigma_{\rm tx}^2} + \frac{2}{\sigma_{\rm rx}^2}, \qquad \frac{1}{D_{{\rm tx,rx},x,y}^2} = \frac{1}{\Sigma_{\rm tx,rx}^2} + \frac{1}{\sigma_{x,y}^2}. \tag{5.28}$$

The expression for coherence then becomes

$$\rho = \frac{\exp\left[-\frac{1}{2}\frac{D_x^2}{\Sigma^2}\frac{\theta_{xo}^2}{\sigma_x^2} - \frac{1}{2}\frac{D_y^2}{\Sigma^2}\frac{\theta_{yo}^2}{\sigma_y^2}\right] e^{-2\pi i A\theta_{xo}D_x^2/\sigma_x^2} \exp\left[-\frac{1}{2}(2\pi A)^2 D_x^2\right]}{\left(\exp\left[-\frac{1}{2}\left(\frac{D_{{\rm tx},x}^2}{\Sigma_{\rm tx}^2} + \frac{D_{{\rm rx},x}^2}{\Sigma_{\rm rx}^2}\right)\frac{\theta_{x0}^2}{\sigma_x^2} - \frac{1}{2}\left(\frac{D_{{\rm tx},y}^2}{\Sigma_{\rm tx}^2} + \frac{D_{{\rm rx},y}^2}{\Sigma_{\rm rx}^2}\right)\frac{\theta_{y0}^2}{\sigma_y^2}\right]\right)^{1/2}} \tag{5.29}$$

The normalisation in (5.15) removes the absolute scattering levels and most of the effect due to tapering antenna patterns (the exponentials over $-\theta_{xo,yo}^2$) from the expressions. Any remaining difference from the simple expression (5.21) in the resulting coherence for a given pattern and structure size is due to the exponents in the remaining two exponentials in (5.29) being multiplied by $D_x^2/\sigma_x^2$.

Figure 5.1, shows how the quantities $\langle |f_{\rm tx}|^2 \rangle$, $\langle |f_{\rm rx}|^2 \rangle$, $\langle f_{\rm tx} f_{\rm rx}^* \rangle$ and $\rho$, equation (5.29), vary as a Gaussian structure 1/10 of the fringe size is placed in different positions across the beams of the antennas.

### 5.1.5 Equal Gaussian antennas

When the transmitter and receiver antennas are equal, $\Sigma = \Sigma_{\rm tx} = \Sigma_{\rm rx}$, $D_x = D_{{\rm tx},x} = D_{{\rm rx},x}$ etc., and the expression for coherence can be greatly simplified,

$$\rho = e^{-2\pi i A\theta_{xo}D_x^2/\sigma_x^2} \exp\left[-\frac{1}{2}(2\pi A)^2 D_x^2\right], \tag{5.30}$$

and it is easy to see how this expression simplifies to (5.21) when $\Sigma \gg \sigma_x$, which implies $D_x \approx \sigma_x$.

### 5.1.6 Interpretation as physical size

Let us see what the results (5.21) and (5.29) implies in terms of physical size for a given observed coherence. In figure 5.2, the maximum observable coherence is plotted versus structure size along the baseline for some ionospheric ranges. The solid lines are for the detailed result (5.29), while the dashed lines are for the simpler result (5.21). Wavelength,

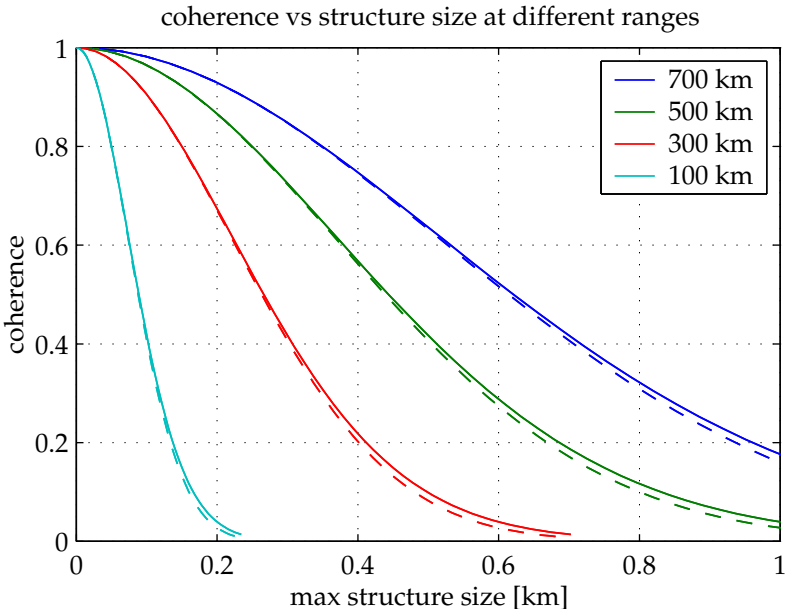


**Figure 5.2:** Coherence as a function of horizontal structure size for some ranges. The dashed lines are for the simple expression (5.21), and the solid lines are for the detailed expression (5.29), with parameters (beam widths, wavelength and antenna separation) for the ESR

antenna separation and beam widths are for the ESR. We see that the detailed expression produces results that are indistinguishable from those of the simpler expression in this case.

After the presentation of power spectrum and cross-spectrum estimation in the next section, the subject of size estimation is revisited in section 5.2.3.

## 5.2 Power spectrum and cross-spectrum estimation using autocorrelation and cross-correlation estimates

As we are interested in the detailed spectral properties of the scattering processes under observation, we need the best possible estimators for the power spectra and cross-spectra of the scattering. There is plenty of literature on the subject of spectral estimation, and we will not make a detailed review in the present work. A thorough treatment of this subject is found in e.g. Percival and Walden (1993).

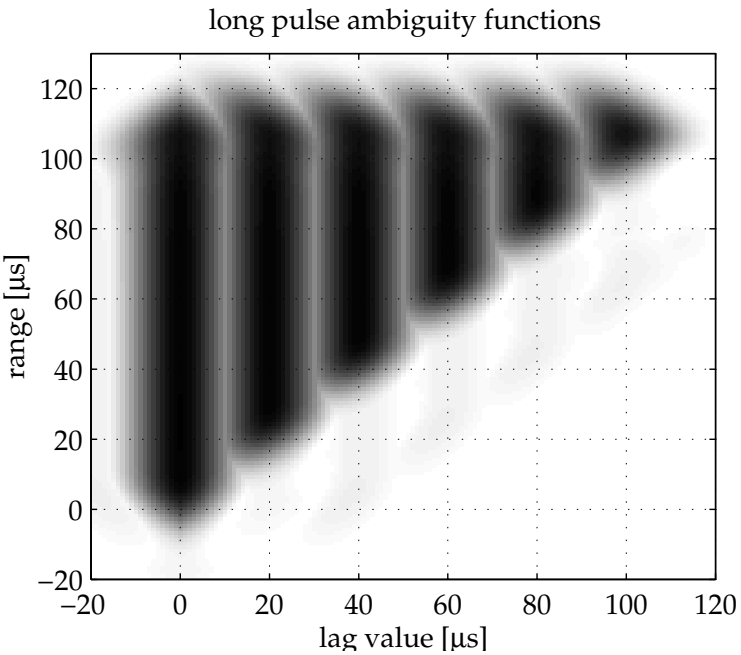


**Figure 5.3:** The range-lag ambiguity functions for a long pulse modulation. The ambiguity functions for lags 0, 20, 40, 60, 80 and 100 $\mu$s are shown in the same diagram; where they overlap, the stronger is shown. The impulse response used is from a 50 kHz Butterworth filter.

Spectral estimation techniques can be divided in two broad classes: filter bank methods and parametrised methods. The latter assumes a parametrised model for the spectrum and estimates the values for these parameters, and is optimal when the process is well understood. These techniques will not be touched upon here. Filter bank methods make no prior assumptions on the shape of the spectrum and are appropriate when the process is less well understood or there is a chance that data does not fit any preconceived model. Filter bank methods for discrete-time data can be subdivided in direct spectral estimation techniques which, in one way or another, use the Discrete Fourier Transform (DFT) on the received signal, and correlation techniques which, in one way or another estimate correlations of the received signal, which are Fourier Transformed to make an estimate of the power spectral density.

Most discussions of spectral estimation will assume the signal to be stationary to some order or even wide-sense stationary. For IS radar, the signal scattered from any given range will usually fulfill such conditions on timescales of at least a few seconds. For systems with continuous illumination and where the range contributing to the scattering is decided by geometry (e.g. bi- or multistatic systems), these techniques can be applied directly. For radar backscattering, the sensitive receiver must be separated from the pow-

erful transmitter, and the only practical way of doing this with a single antenna is by pulsing the transmitter on for short periods followed by longer periods of receiving. The signal received on the ground contains contributions from many different ranges, and the contributing range changes over the length of the signal vector. As the physical parameters which characterise the scattering from a given volume changes with range, the received signal is obviously not stationary. When creating a spectral estimate from such a compound signal, it is necessary to limit the spatial contribution (by means of the length of the pulse) to no more than typical scale heights in the medium. For incoherent scattering, a further complication is that the scattered signal has random phase, so signal from successive pulses cannot be integrated together unless the random phase component has been eliminated. (A few notable exceptions exist: Polar Mesospheric Summer Echoes — PMSE — and Sporadic E-layer echoes).

One of the simplest, and earliest, direct spectral estimators is the Periodogram

$$\widehat{S}^{p}_{zz}(\omega) = |FT\{z\}|^2, \tag{5.31}$$

which is simply the absolute value of the (Discrete-time) Fourier Transform of the data vector. Refinements include subdividing the vector into sub-vectors which are Fourier Transformed separately and the result averaged (Bartlett), and windowing the sub-windows and allow them to overlap (Welch). One unfortunate property of this estimator in its basic form is that it is not consistent, that is, the variance of the estimate does not tend towards zero as the number of points used increases.

The corresponding correlation-based spectral estimator is the Blackman-Tukey estimator

$$\widehat{R}_{zz}(k\Delta\tau) = \frac{1}{N-k}\sum_{i=1}^{N-k} z_i z^*_{i+k}, \qquad \widehat{S}^{(\mathrm{BT})}_{zz}(\omega) = FT\{\widehat{R}_{zz}\}, \tag{5.32}$$

where the correlation function is estimated using the unbiased ACF estimate. This estimate can result in negative spectral estimates, which is clearly unphysical. If $N-k$ in the denominator is replaced with $N$, the estimate is called the standard biased ACF estimate, and the resulting spectral estimate is equivalent to the Periodogram. In this technique, the data vector is divided into sub-vectors and within each sub-vector, every possible lagged product $z_n z^*_{n+k}$ is formed and averaged. This view of the periodogram exposes some of the problem with this estimator. In particular, the number of averaged points decreases with lag, leading to especially bad variance in the longer lags, which severely affects the spectral resolution.

### 5.2.1 Trapezoidal weighting

In pulsed radar, another unfortunate property of this spectral estimator emerges, one which can be illustrated through the use of ambiguity functions (Lehtinen, 1986). For every lagged product $z_n z^*_{n+k}$, we can compute exactly what region in range and lag contributes

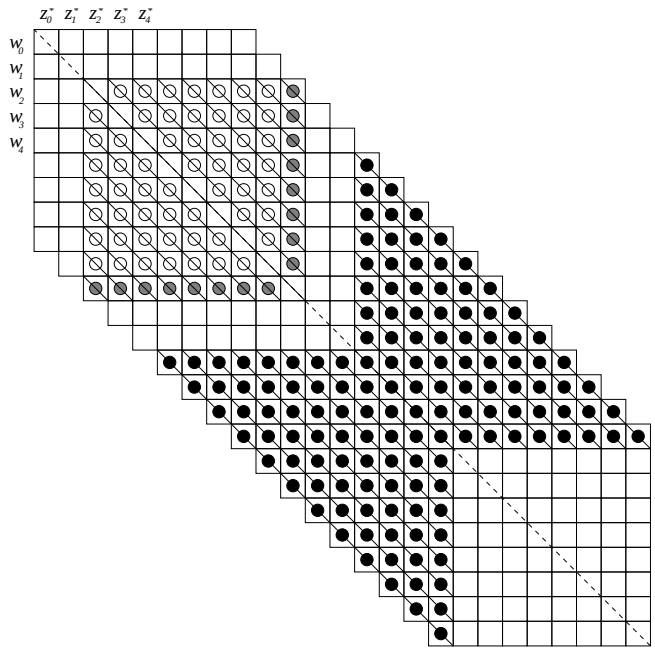


**Figure 5.4:** A small cross-lag profile matrix (XLPM) with eight non-zero lags in either direction. The black disks indicate the points used for estimating the cross-correlation function (XCF) for a single range gate of a long pulse modulation; four lag zero points are used here. The points along each diagonal are averaged to form the estimate of the cross-correlation at that lag value. For coded pulses (alternating codes or random codes), the open and shaded circles indicate the lagged products that are used to form a single range gate. The shaded circles indicate the positions of the points in a result (decoded) LPM that correspond to this range gate. The symbols $w$ and $z$ refer to the complex sample vectors from the two antennas, called $f_{\mathrm{tx}}$ and $f_{\mathrm{rx}}$ in section 5.1

to this product, given the transmitted waveform and the impulse response of the receiver. In figure 5.3, ambiguity functions for a 120 $\mu$s long pulse are shown, for lagged products at lags of 0 to 100 $\mu$s, at 20 $\mu$s intervals. The impulse response used is that of a 50 kHz Butterworth filter, matching a 20 $\mu$s sampling interval. In addition to getting fewer lagged products at longer lags, the volume contributing to the measured correlation *per lagged product* decreases with lag, and the level of clutter (uncorrelated signal) increases (not shown). To compensate for the reduction of volume, it is possible to combine lagged products into estimates of correlation at a given lag in such a way that a full correlation function estimate is obtained with similar range contribution at every obtainable lag value.

$$\widehat{R}_{zz}^{\mathrm{tz}}(k\Delta\tau) = \frac{1}{N+k} \sum_{i=k_0-k}^{N} z_i z_{i+k}^* \tag{5.33}$$

This differs from the correlation function estimator used in the Blackman-Tukey estimate in that more points are averaged for longer lags. This is called trapezoidal rule summation (Turunen and Silén, 1984; Nygrén, 1996, sec. 5.8) and is illustrated with the black circles in figure 5.4, the points that are averaged are those along each diagonal, connected with a line.

For cross-correlation functions, the lagged cross-products are from the two different signals, and the summation rule has been extended to cover negative lags also, as is appropriate for cross-correlation functions.

$$\widehat{R}^{\mathrm{tz}}_{wz}(k\Delta\tau) = \begin{cases} \dfrac{1}{N+k} \displaystyle\sum_{i=k_0+k}^{N} w_{i-k} z_i^* & k < 0 \\ \dfrac{1}{N+k} \displaystyle\sum_{i=k_0-k}^{N} w_i z_{i+k}^* & k \geqslant 0 \end{cases} \tag{5.34}$$

Traditionally, analysis programs for IS radar data would use techniques like that described above to estimate the scattered spectrum and try to fit physical parameters to it for every range gate. Modern analysis programs (OASIS (Holt *et al.*, 1992), GUISDAP (Lehtinen *et al.*, 1996)) will instead consider whole profiles of lagged products, taking the ambiguity function of each product into consideration, and produce a profile of ionospheric parameters. Although this clearly superior approach has been demonstrated to work and to give substantial benefits, it has not yet superseded the traditional methods.

### 5.2.2 The effect of windowing on the spectral estimate

Power spectrum or cross-spectrum estimates are obtained by Fourier transforming the correlation function estimates, but the resulting spectrum is subject to distortions depending on the lag windowing function employed (Percival and Walden, 1993, sec. 6.7 and 6.8). If the correlation function estimator is an unbiased estimator of the true power spectrum $S(f)$ and the windowed estimator is denoted by $\widehat{S}^{(w)}(f)$, then the effect of the window is a smoothing in the spectral domain

$$E\{\widehat{S}^{(w)}(f)\} \approx \int_{-f_N}^{f_N} H(f - f')\, S(f')\, df' \tag{5.35}$$

where $E\{\cdot\}$ signifies the expectation value and $H$ is the Fourier transform of the lag window used, called a *kernel* in this context. Fourier transforming the correlation function estimates directly corresponds to using a rectangular window which has a $\sin(x)/x$ kernel. This kernel has slowly decaying side-lobes, which give rise to an effect called *spectral leakage*, where the estimation of low-power frequencies is influenced by high-power frequencies. In figure 5.5, this effect is identified as oscillations in the power spectrum. In the coherence (lower right panel), windowing effects from the cross-spectrum and, through the normalization, the

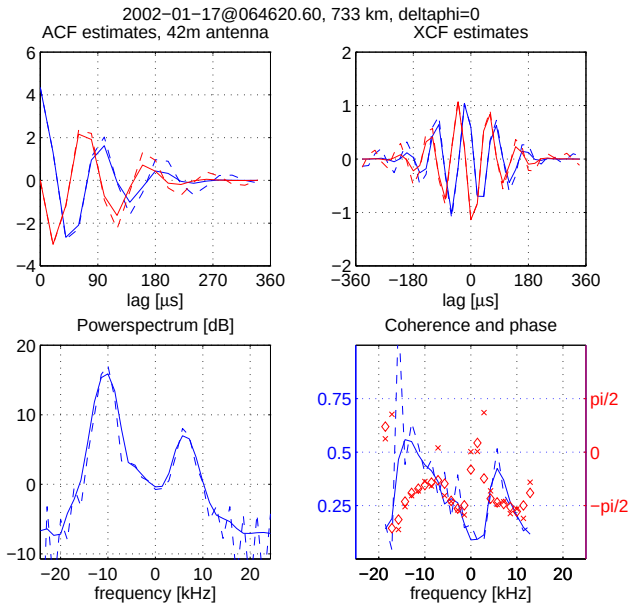


**Figure 5.5:** The effects obtained using windowing on the correlation functions, these examples are from the 0.2 s integration starting on 06:46:20.60 UT, for the range gate centered at 733 km. The top two panels show correlation function estimates computed from the measurements, real parts in blue, imaginary parts in red. Broken lines are the original estimates, solid lines are after windowing has been applied. The top left panel shows the ACF estimate obtained with the 42 m antenna, while the top right panel shows the XCF estimate. The bottom left panel shows the resulting power spectra, using rectangular (broken line) and Hanning (solid line) windows, while the bottom right panel shows the resulting coherence (blue lines) and phase (red markers) for rectangular window (broken lines, crosses) and Hanning window (solid lines, diamonds).

power spectra, can be seen. The Hanning window's kernel has fast decaying side-lobes, at the cost of a wider main-lobe. This gives estimates with good protection against spectral leakage at the cost of a slight loss of spectral resolution.

While the effect of improper windowing is not very obvious in the power spectra, except in the low-power frequencies, the effect on the coherence estimation is profound. In the lower right panel of figure 5.5, the coherence curve for rectangular windows (the broken line) shows large oscillations and it exceeds unity on occasions, both of which are unphysical. Using a well-behaved window eliminates the unphysical behaviour.

The Hanning window is not the only possibility, other windowing functions can also be used. In figure 5.6 is plotted the resulting spectra from the same data set using three different windows, compared to the result when not using windowing. The expressions for

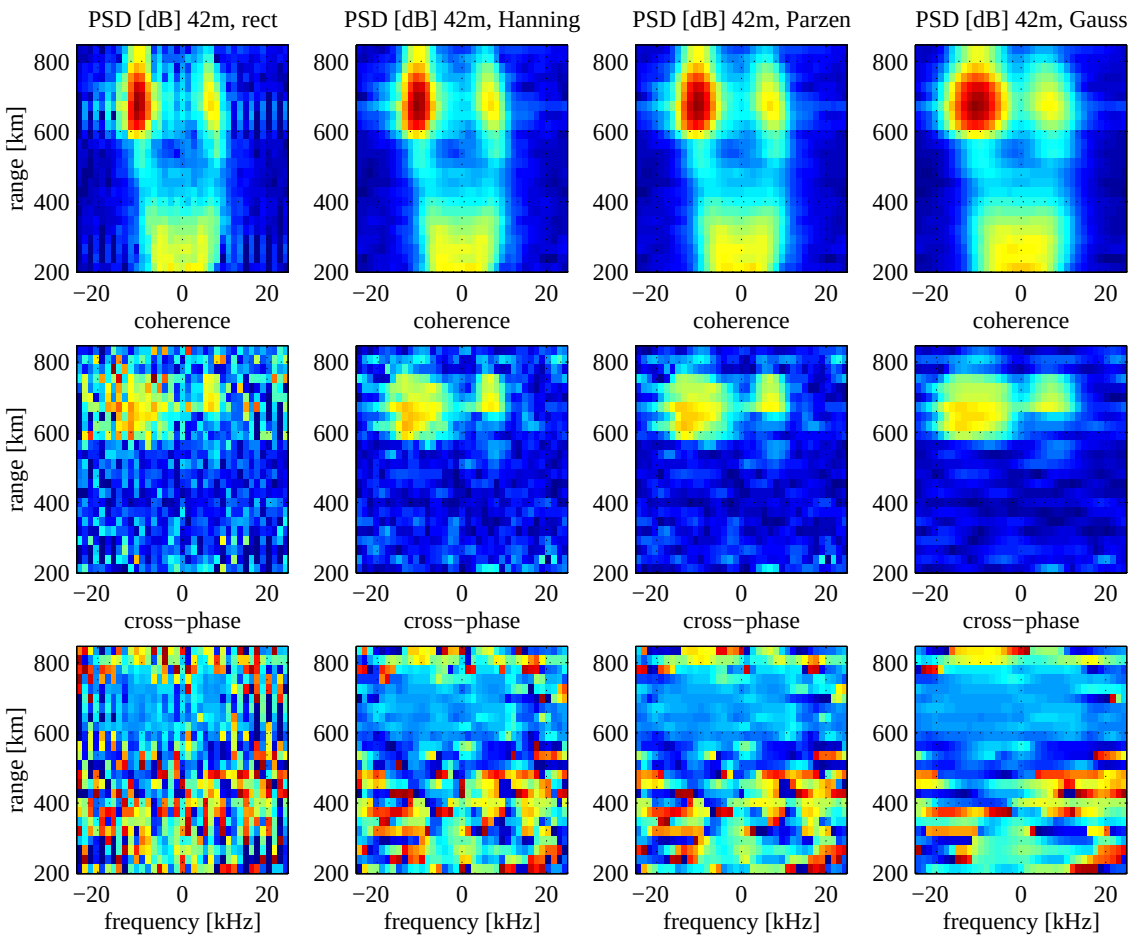


**Figure 5.6:** Comparing the effect of various windowing functions. From top to bottom, the panels are 1) power spectral density for the signal from the 42 m antenna, on a logarithmic colour scale from $-5$ dB (blue) to 20 dB (red), 2) coherence, ranging from 0 (blue) to 1 (red), and 3) cross-spectrum phase, from $-\pi$ (blue) to $\pi$ (red). The windowing functions employed are, from left to right, rectangular (no windowing), Hanning, Parzen and Gaussian. The data is from 2002-01-17, the 0.2 s integration starting at 06:46:20.60 UT.

the various windows are

$$\text{Hanning}(k) = \frac{1}{2}(1 + \cos(k\pi/M)), \qquad k \in \{0, \ldots, M\}$$

$$\text{Parzen}(k) = \begin{cases} 1 - 6(k/M)^2 + 6(k/M)^3 & k \leqslant M/2 \\ 2(1 - k/M)^3 & k > M/2 \end{cases}$$

$$\text{Gauss}(k) = \exp(-k^2/M), \qquad k \in \{0, \ldots, M\}$$

The oscillations due to the rectangular window are obvious in the leftmost panels of this figure, but which is removed when some windowing is applied. Also obvious is the smoothing in the frequency domain which results from the windowing. The effect is most noticeable for the Gaussian window, while the Hanning and Parzen windows do not cause as much smoothing. While the points of highest coherence for rectangular windows are invariably on the edge of the coherent region and due to negative oscillations in the power spectral density estimation which result in near-zero values, the windowed estimates do not have negative oscillations and high values of observed coherence are usually from the centre of coherent regions.

An unfortunate effect of introducing windowing is that it adds an element of choice, or even taste, to the spectral estimation. While it is obvious from figure 5.6 that some sort of windowing is necessary, it is not necessarily obvious *which* window to use. Informally, a decrease in spectral resolution is the price paid for a decrease in the variance of the estimate, and the optimal trade-off must be decided for each application.

A number of examples of power spectra and cross-spectra obtained using trapezoidal summation rule and Hanning windows are shown in sections 5.5 and 6.3

### 5.2.3 Observed coherence and size

Power spectra are computed from ACF estimates by making them periodic, then applying the Hanning window and Fourier Transforming. An example of a power spectrum is shown in the lower left panel of figure 5.5. Cross-spectra are formed the same way, except that they are not made periodic. Coherence is then computed by normalizing the cross-spectrum by the geometrical mean of the power spectra

$$\rho = \frac{S_{\text{tx,rx}}}{\sqrt{S_{\text{tx,tx}} S_{\text{rx,rx}}}} \tag{5.36}$$

The normalization is done frequency by frequency. An example of a coherence spectrum is shown in the lower right panel of figure 5.5. High coherence indicates scattering from a spatially limited structure, as discussed in section 5.1.6. The magnitude of the observed coherence is a measure of the size of the scattering structure in the direction of the baseline, while the phase corresponds to its position along the baseline, although this correspondence is not unique.

Sky noise is present in the signal from both antennas, and no attempt is made at correcting for this in the present work. Since noise in each signal correlates with itself, but they are mutually uncorrelated, the presence of noise, through the normalization in equation (5.36), leads to a lowering of the observed coherence relative to the maximum observable coherence for a structure of a given size. This effect is more severe for low signal to noise ratios. As a result, structures on the edge of the antenna pattern will appear with lower coherences than

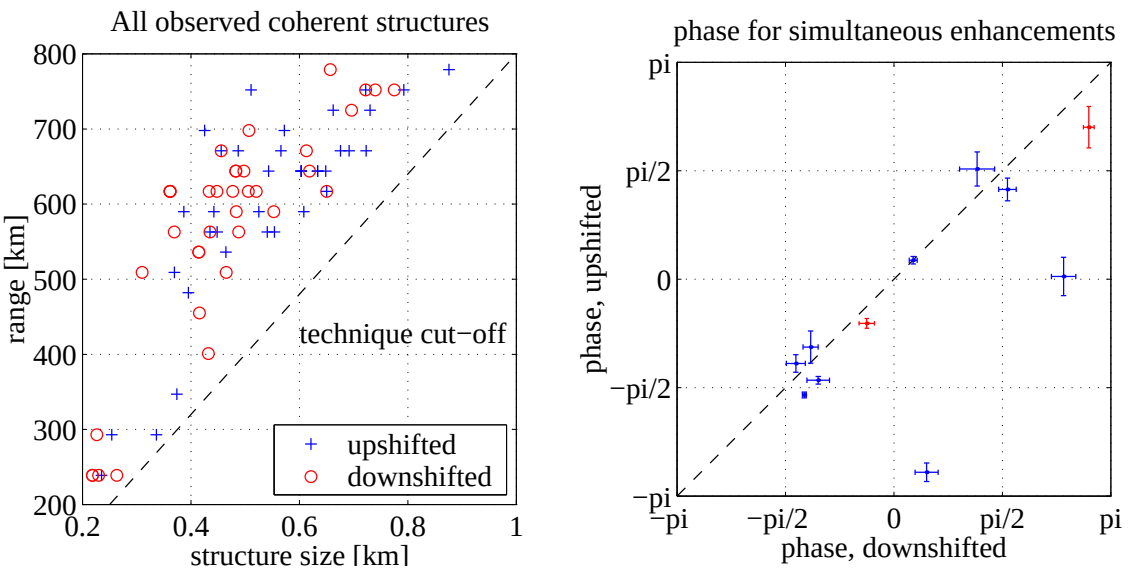


**Figure 5.7:** All observed coherent structures, plotted versus range and maximum structure size in the left panel, Phase in the coherent upshifted enhancement versus phase in the coherent downshifted enhancement in the right panel.

corresponding structures centered in the beam. Multiple localised scatterers at the same range and frequency will also reduce the observed coherence. As discussed by Grydeland *et al.* (2003b), this means that estimating the horizontal size of a scattering structure as discussed in section 5.1.6 without considering these sources of error results in overestimating the structure size. Our size estimates are therefore upper thresholds of actual sizes.

Figure 5.7, left panel, shows the size of the observed coherent structures, plotted versus altitude. The cut-off seen in the figure is due to structures larger than about half the fringe size do not result in sufficiently high coherence to be detected. The selection method used is explained in Grydeland *et al.* (2003a).

### 5.2.4 Evidence of simultaneous enhancement

The cross-spectrum phase due to a localised scatterer depends on its position along the baseline as indicated by equation (5.25), and is computed frequency by frequency. As a result, when the coherence indicates a localised scatterer at a given range and frequency, phase in this range-frequency region can be used to determine the position of the scatterer in one spatial dimension. This determination is not unique, as phase repeats itself multiple times within the beam, and it provides no information on position in the direction perpendicular to the baseline. When both up- and down-shifted enhancements occur within the same integration period, and both have significant coherence and the same cross-spectrum

phase, there are therefore at least two ways this can occur without the scatterers occupying the same physical space. The scatterer can be displaced in the direction perpendicular to the baseline — the $y$-direction — or it can be displaced by a distance in the $x$-direction which corresponds to a phase shift of exactly $2\pi$, or a combination of both.

From the coherent cases shown in figure 5.7, left panel, those where an upshifted and downshifted coherent enhancement were seen within 100 km of range of each other in the same 0.2 s integration were selected. For these cases, phase in the upshifted enhancement ($\phi_+$) is plotted against phase in the downshifted enhancement ($\phi_-$) in figure 5.7, right panel. The error bars are a measure of the variation of phase in a small range-Doppler region centered on the point of highest coherence. The selection procedure for the cases shown is explained in Grydeland *et al.* (2003a).

If the speculation that two enhanced shoulders rarely coexist on one magnetic field line due to Sedgemore-Schulthess *et al.* (1999) were correct, we would expect the points in figure 5.7, right panel, to be distributed evenly across this field. If both shoulders instead are produced on the same or immediately neighbouring field lines, we would expect them to follow the $\phi_+ = \phi_-$ line indicated with dashes. All but two of our identified cases lie on this line. In combination with the increased temporal resolution discussed in the next section, this is strong evidence that simultaneously enhanced shoulders are produced in the same volume.

## 5.3 Temporal resolution

From a purely theoretical point of view, there are two fundamental constraints on temporal resolution: How fast can information about the phenomenon be collected; and how fast does the phenomenon itself change. As long as the time resolution offered by the former is better than that required by the latter, there is no problem. An immediate question is then how one can be sure that shorter timescales than those detectable by the instrument do not exist. To answer this question, an understanding of the underlying physics must support our findings.

With TSV data available, we have the opportunity to form integrated (time-averaged) data at multiple time resolutions, lowering the integration period until significant detail no longer appears. The question of what constitutes significant detail becomes tricky as the signal to noise ratio decreases. In figure 5.8, we show the same period processed at three different time resolutions. The vertical scale is in dB, so there is no question that fluctuations much greater than the noise level exist even on the shortest of the timescales used in this figure, 50 ms. On the other hand, even the coarsest of these time resolutions, 200 ms, is able to capture the overall development of the event, the correct ratio between up- and down-shifted enhancement etc, even if the steepest of the increases and decreases are smeared out somewhat. For the observations from this experiment presented here, 200 ms integration will be used.

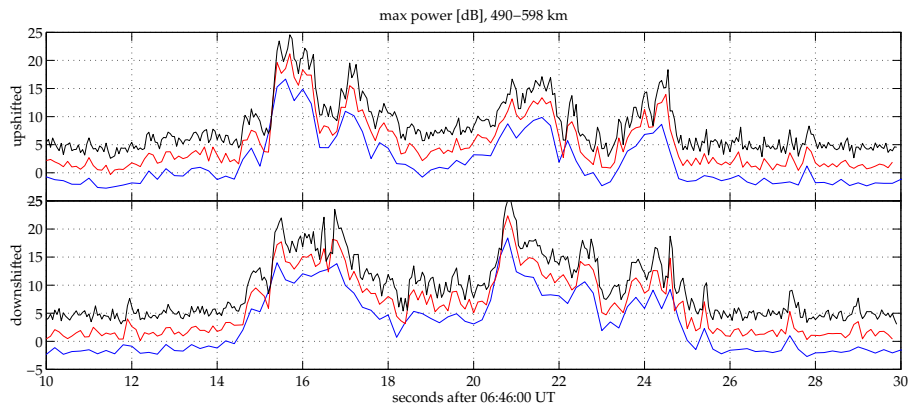


**Figure 5.8:** Time development of the enhanced echoes over the lifetime of the event, at three different time resolutions. We have extracted the power at the peak of the ion-acoustic shoulder in the region from 490 to 598 km separately for the up- and down-shifted shoulders. Three different integrations are shown here, 50, 100, and 200 ms. The 100 and 50 ms curves have been shifted upwards by 3 and 6 dB, respectively, to help separate the curves.

## 5.4 Range ambiguities due to incomplete code sets

Range resolution requires short pulses, as described above. At the same time, sufficient spectral resolution can only be obtained by having pulses at least as long as the typical correlation time of the scattering medium. As the scale height decreases and the correlation time of the medium increases with decreasing range, simultaneous demands on spatial and spectral resolution can no longer be accommodated simultaneously below a certain range, and techniques like multi-pulse codes (Farley, 1972), or alternating codes (Sulzer, 1986; Lehtinen, 1986; Lehtinen and Häggström, 1987; Sulzer, 1993) must be used, where increased range resolution is obtained at the cost of introducing uncorrelated signal (clutter) from nearby ranges.

The classical radar modulations — long pulses, short pulses, Barker coded pulses and multi-pulse patterns — achieve their range resolution on every transmit-receive period. The same is not true for alternating codes, whether random or deterministic. For these modulations, the pulse is divided into elementary bauds (which ultimately decide the range and lag resolution) and 180° phase change applied to every baud at random, or in a prescribed pattern. Every modulation pattern causes range ambiguities, but the correlation estimates from every pattern can be combined to form estimates which are ambiguity-free in an average sense (for random codes) or exactly (for deterministic codes). Every lagged product from a pair of baud samples is decoded in different ways to produce an estimate of the correlation at that lag value with net contribution from a range corresponding

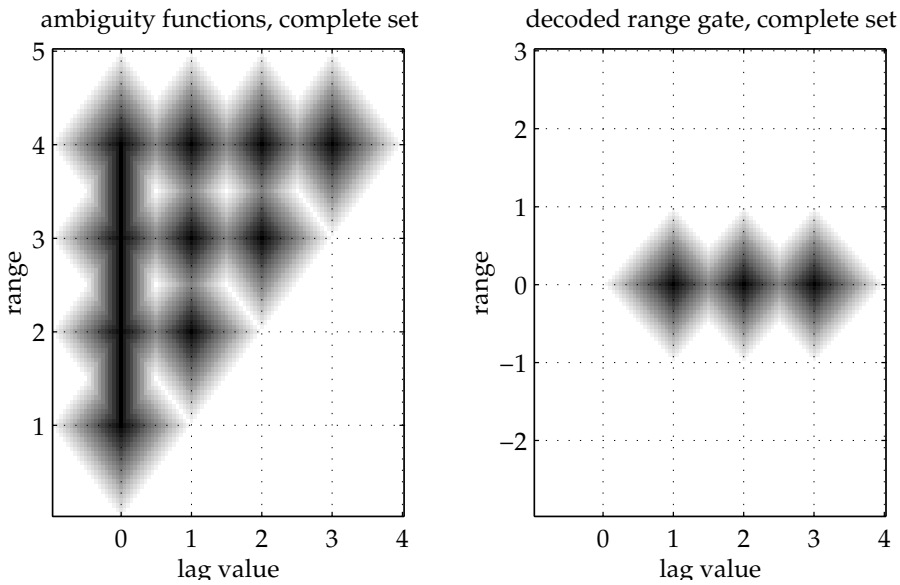


**Figure 5.9:** The two-dimensional range-lag ambiguity functions for a 4-bit strong alternating code. The elongated structure is the ambiguous zero-lag ambiguity function, while the remaining six pyramids are the six separate ambiguity functions available from the code; three for lag one, two for lag two and one for lag three. Whenever two ambiguity functions overlap, the larger one is shown. The right panel shows the resulting ambiguity functions for a completely decoded range gate. The pattern is highly localised; it has no side structure outside $\pm 1$ in range.

to a single baud — and this can be done for every range encompassed by this pair of bauds. An explanation of the decoding procedure where the essence does not disappear in mathematical mystery and which is valid for random and deterministic alternating codes alike can be found in (Farley, 1996).

For every code in an alternating code set, an LPM (or XLPM) like that in figure 5.4 is computed. These LPMs are combined in various ways, with signs computed from the codes transmitted, to form the ambiguity-free lagged products in a (decoded) result LPM. The points marked with open and shaded circles along a single diagonal in figure 5.4, when decoded in all possible ways for all modulations, result in a single ambiguity-free estimate of that lag in the shaded point along the same diagonal. For the next decoded point, the whole pattern is shifted one position.

Combining correlation estimates from codes where the phase coding of the modulation differs from one pulse to the next obviously requires the scattering target to be stationary for periods matching the code cycle period. For most applications, this is not a problem.

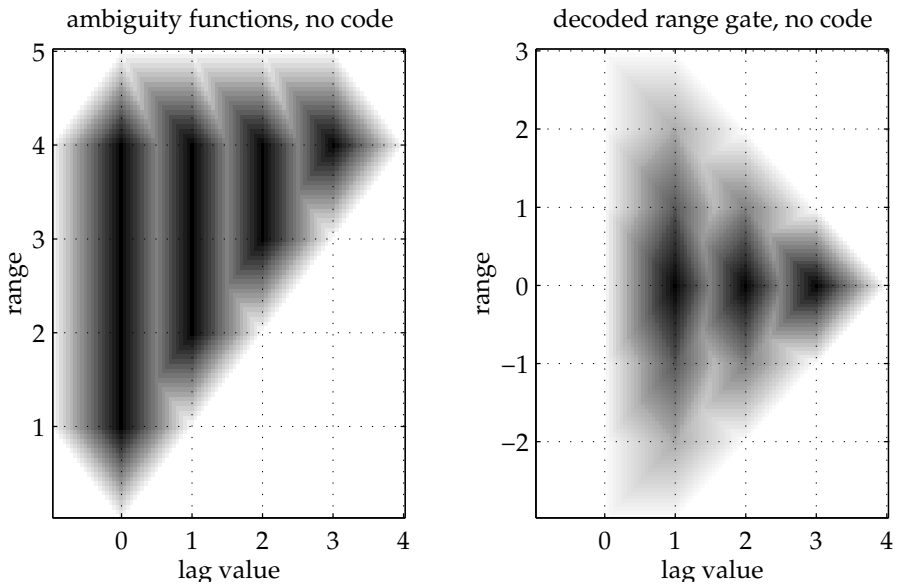


**Figure 5.10:** As figure 5.9, but when coding has broken down completely, i.e. all bauds are the same. The resulting range gate still has the largest contributions the the intended range but precise location has become much more difficult, and every lag has contributions from quite different volumes.

Typical integration periods are from five or ten seconds to several minutes, while the time to complete a cycle of an alternating code is usually on the order of half a second (`tau0`: 0.64 s) to a few seconds (`HPLA2`: 2.5 s). For analysis, integration of one or more minutes is common. In some of the observations presented later in this chapter, the scattering changes significantly within a tenth of a second. If such a phenomenon is to be studied with alternating code experiments, we first need to know to what extent the missing pieces of the code causes range ambiguities to remain.

In the left panel of figure 5.9, all possible range-lag ambiguity functions for a complete 4-bit deterministic alternating code set have been plotted, using a boxcar impulse response. This is the same figure as figure 6.6 of Nygrén (1996). While the zero lag is ambiguous, all other lags can produce a collection of ambiguity-free lagged products, every pyramid is a separate range-lag ambiguity function. When extracting a range gate, decoded lag one products for each of the three possible decodings are combined from three neighbouring pulse pairs to form an unambiguous lag one estimate for a single range. The resulting alternating code range gate is shown in the right panel of figure 5.9. As expected, every lag has the same range-lag ambiguity functions. Lag zero is not shown in this panel.

In figure 5.10, we see exactly the same picture, but this time for a case where coding has broken down completely, every transmitted baud has been identical. The three lag one

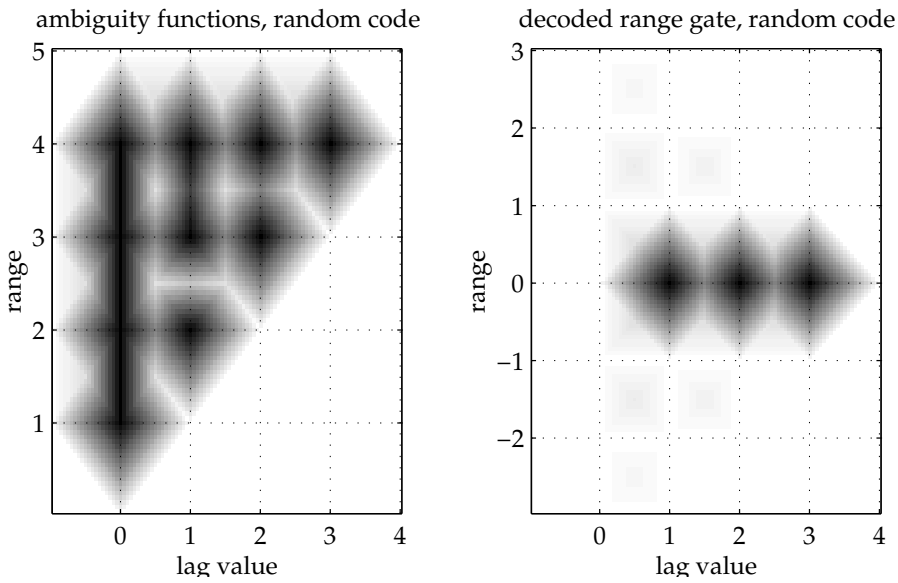


**Figure 5.11:** As figure 5.9, for 8 scans of a random code. Although the side structure cancellation is not perfect, it is still very good. The remaining side structure can be accounted for in analysis or removed via inverse methods on the individual lag profiles. Expressing every 4-bit scan of the code as a hexadecimal digit, the code is `4e1f6034`.

estimates have exactly the same ambiguity function, as have the two lag two estimates, and they all have a range extent as large as for a long pulse of corresponding length, notice the similarity with the long pulse case presented in figure 5.3. The right panel shows the range ambiguity functions for a single range gate. Every lag has range contributions from a volume centered at the intended range, and with the centre range having the largest contribution. This is an absolute worst case for the coding, no real-life case would ever be this bad. This case is in fact exactly what would be obtained for a long pulse the length of the code using the (unmodified) Blackman-Tukey estimate.

Finally, in figure 5.11, we see the case for eight scans of a 4-bit random code. The ambiguity functions in the left panel are no longer identical, and the decoded range gate, in the right panel, while showing basically the same shape as for a complete deterministic code set, still has some contributions from outside the intended range.

We are now in a position to evaluate the impact of using subsets of a complete alternating code set. In the top left panel of figure 5.12 we have plotted the range-lag ambiguity functions for a range gate of a subset consisting of 8 consecutive randomly selected scans of the 32 scans from the `tau0` code set. The bottom left panel shows the difference between this result and that for a complete code set, with an enhanced colour scale. For comparison, the corresponding results for a random code set of the same size is shown in the two panels

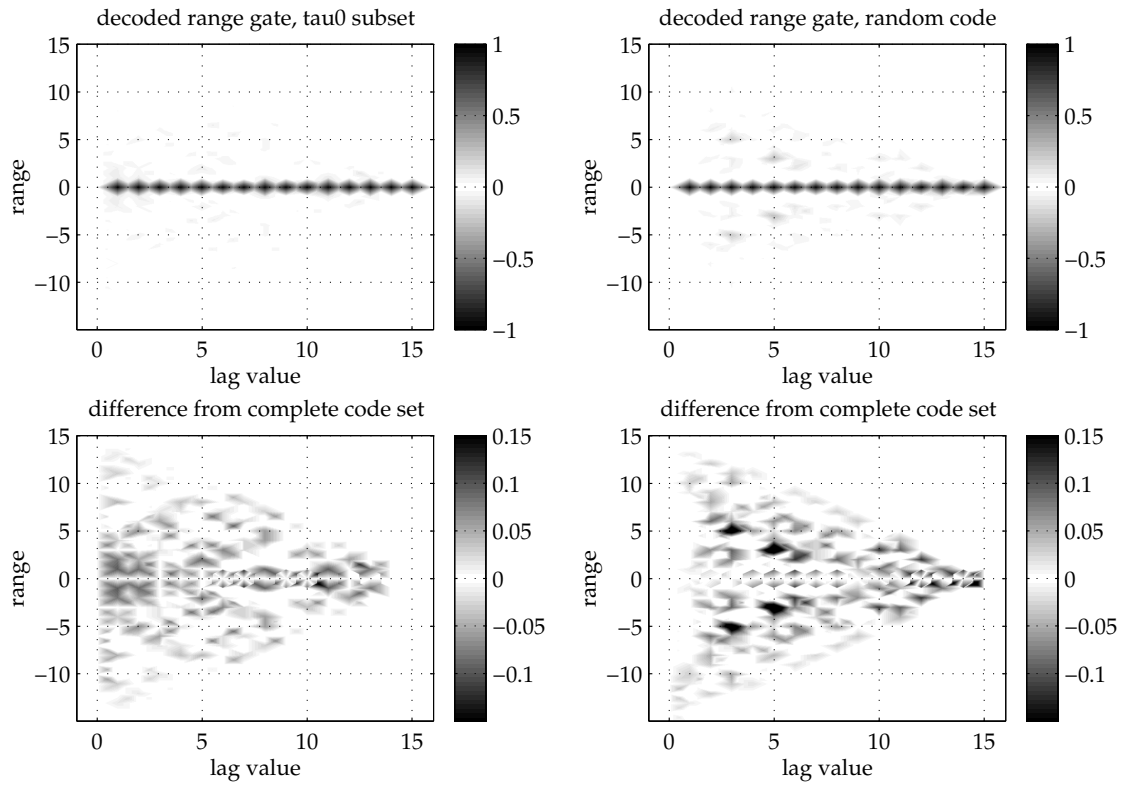


**Figure 5.12:** Comparing a subset of the `tau0` deterministic code set to the left, with a similar-size set of random codes to the right. The top two panels show the resulting range gate ambiguity functions, while the bottom two panels show the difference from the ambiguity functions of a complete code set. The code set sizes in this figure correspond to 160 ms integrations. The `tau0` figure uses scans 12 through 19 of that code, while the random code, expressed as hexadecimal words, is `3a6a e904 05d1 39a6 25bf 0a8e 93e9 80dc`.

to the right. Since randomness is involved, the figures will change for every selection of random numbers, but the figures shown are representative. Off-centre volumes can contribute with as much as 10-15% of the centre volume, and leakage from a given volume broadly, albeit not exactly, symmetric. Since this contribution varies from lag to lag, we can only consider it an addition to the noise floor in general.

As long as the ambiguity functions for each lag has reasonable shapes (which will be the case for all but pathological code sets) it is possible to use inverse methods on every ambiguous lag profile with appropriate regularization to obtain the most likely unambiguous profile for that lag (Damtie *et al.*, 2003).

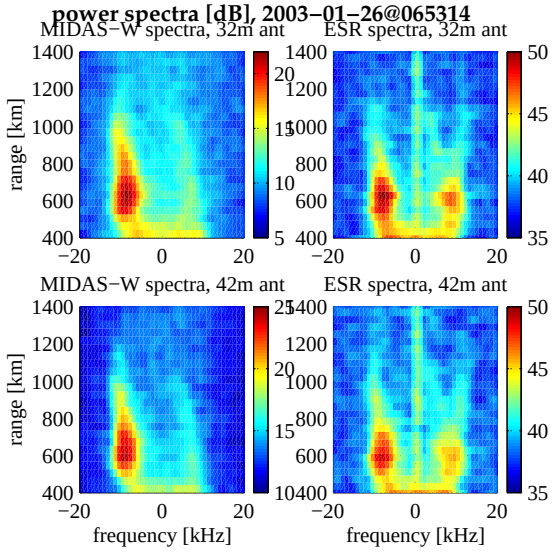


**Figure 5.13:** One of the observed enhancement event, as seen by the two systems. MIDAS-W spectra to the left, ESR spectra to the right. These are from 2003-01-26, the two second integration starting at 06:53:14 UT. Spectra are not background subtracted, and not corrected for attenuation with range squared.

Enhanced echoes have yet to appear during interferometric observations using coded pulses. It is therefore not entirely clear whether interferometry will work with coded pulses, or if the clutter (uncorrelated signal from neighbouring ranges) will be sufficiently strong that no observable coherence will result. One result which indicates that it might work was a recent presentation by Meyer *et al.* (2002), where a meteor was observed with passive radar, a technique where signal to noise ratio is always limited by clutter.

In figure 6.5 an example is shown of what appears to be a satellite, observed with the ESR interferometer using alternating codes.

## 5.5 Recovering spectral information from distorted spectra

In January 2003, the Cosmic geophysics group at the physics department of the University of Tromsø had a coordinated optical and radar campaign, with a high-resolution light-enhanced camera and the two antennas of the EISCAT Svalbard Radar, all pointing along the magnetic field, the EISCAT radars operating as an interferometer as described above using the newly developed Langmuir Turbulence experiment, described in section 3.3. This experiment uses long pulses for ion line and plasma line observations in the EISCAT

receiver system, while our portable MIDAS-W receiver is recording TSV data (at ion line frequencies) directly from both antennas.

During the 2003 campaign, we again made observations of the kind of enhanced echoes we were hoping to see in the MIDAS-W data. Like the year before, parts of these observations were associated with high coherence and other parts were not. The events seen this year exhibited quite high Doppler shifts, the Doppler shift increasing with altitude. This indicates outward streaming ions, their outward velocity increasing with altitude, as can be seen even with the naked eye in the left panels of figure 5.13. The curious thing was that from all our preliminary plots, the MIDAS-W data was showing significant asymmetry, while the data from the EISCAT system appeared almost symmetric. As these two are different digital signal paths from the same analog signal, see figure 3.4, they should have exactly the same spectral information. In other words, the two pictures should be the same in a broad sense, although they will differ in signal level and details.

### 5.5.1 The spectral discrepancy

In figure 5.13, we have made as close a comparison as we could easily make between the two systems. Each panel shows a profile of power spectra on a logarithmic scale, only the ranges from 400 to 1200 km are shown. MIDAS-W data is to the left, while ESR data is to the right. The upper two panels show power spectra from the 32 m antenna, the lower two the 42 m antenna. The `LT1` experiment uses two long pulses per IPP, but as explained in section 3.3, only one of these is monitored in the 42 m antenna. To make the panels in the figure as directly comparable as possible, all panels are created using only this pulse, even though data from both pulses is available for the remaining three panels.

In both the ESR and MIDAS-W receivers, the signal is reduced to some reasonable bandwidth, digitally filtered and decimated to 20 $\mu$s sampling, and full lag profile matrices are computed, where all lags out to 540 $\mu$s are kept. Range gates are then formed using trapezoidal rule summation, figure 5.4, with 13 points averaged for the zero lag estimate, corresponding to about half the pulse length. Data has not been corrected for background noise, nor for the attenuation inversely proportional to range squared seen for volume scattering radar.

Data has been integrated for 2 seconds in both systems, but the clock used in the MIDAS-W system is not exactly synchronized with the ESR clock, so while we can tell from the data that the integration period boundaries are similar, they are not exactly the same.

From this figure, it is clear that the two pictures cannot both be correct. It almost seems as if a mirroring of the stronger (downshifted) peak occurs. In an analog receiver, this can occur when there is a mis-balance between the real and imaginary parts of the receiver. In a receiver where mixing to baseband is done digitally, as is the ESR, this cannot occur.

When this discrepancy was pointed out to EISCAT, their staff immediately found an error in the data transport at the ESR, resulting in the real and imaginary parts of the processed

signal coming from neighbouring samples. Sample $n$ contains the real part from sample $n$ and imaginary part from sample $n+1$.

### 5.5.2 Analytic treatment

For a complex signal $z(t) = x(t) + iy(t)$, its Fourier Transform is given by $Z(\omega) = X(\omega) + iY(\omega)$, and the power spectrum $S_{zz}(\omega)$ is given by

$$S_{zz}(\omega) = |FT\{z\}|^2 = |X(\omega) + iY(\omega)|^2 = |X|^2 + |Y|^2 + 2\,\mathrm{Im}(XY^*) \tag{5.37}$$

Using the imaginary part from sample $n+1$ means *advancing* the imaginary part with a time shift equal to the sampling interval. (If the breach of causality is troubling to the mind, it can be expressed as a delay of the real part instead.) When the imaginary part of the signal has been advanced by a time $\tau$, the signal has become $z'(t) = x(t) + iy(t+\tau)$, with Fourier Transform

$$Z'(\omega) = FT\{x(t)\} + iFT\{y(t+\tau)\} = X(\omega) + iY(\omega)e^{-i\omega\tau} \tag{5.38}$$

and the distorted power spectrum becomes

$$S'_{zz}(\omega) = |X|^2 + |Y|^2 + 2\,\mathrm{Im}(XY^*e^{i\omega\tau}) \tag{5.39}$$

The change in power spectrum due to the error is then given by

$$\Delta = S - S' = 2\,\mathrm{Im}[XY^*(1 - e^{i\omega\tau})] \tag{5.40}$$

The following intuitive picture illustrates what the above means in practice for a single-tone signal $e^{i\omega t}$. The "delay" of $-\tau$ inflicts a frequency-dependent phase shift $\phi = -i\omega\tau$ on the imaginary part. For $\tau = 0$, this shift is zero, and the real and imaginary parts are $\pi/2$ apart in phase. For $\tau \neq 0$ and zero frequency, the effect is likewise nil. As the frequency of the tone increases, the phase shift of the imaginary part also increases, and when $\omega\tau = \pi/2$, the phase difference between the real and imaginary parts has increased to $\pi$ — the real and imaginary parts have exactly opposite phase. This is equivalent to a purely real signal and it has a symmetric spectrum. If the tone frequency is increased to $\omega\tau = \pi$, the phase difference between the real and imaginary parts is $3\pi/2$, which corresponds to a signal $e^{-i\omega t}$, all the signal power has moved over from $\omega$ to $-\omega$. It should be clear from this simple picture that advancing or delaying either part of the signal has the same effect on the observed spectra.

When spectra are symmetric, as is the case for thermal IS spectra, one might imagine that an artefact which introduces symmetrisation of asymmetric spectra has no effect. The effect is actually more subtle than this. Starting with a purely real signal, shifting the imaginary part has no effect, the symmetric spectrum remains symmetric regardless of shift. If the symmetric spectrum is instead composed of proportional real and imaginary parts, where both are non-zero, a shift of the imaginary part again influences the phase difference, but the magnitude of the effect depends on the exact phase of the symmetric signal.

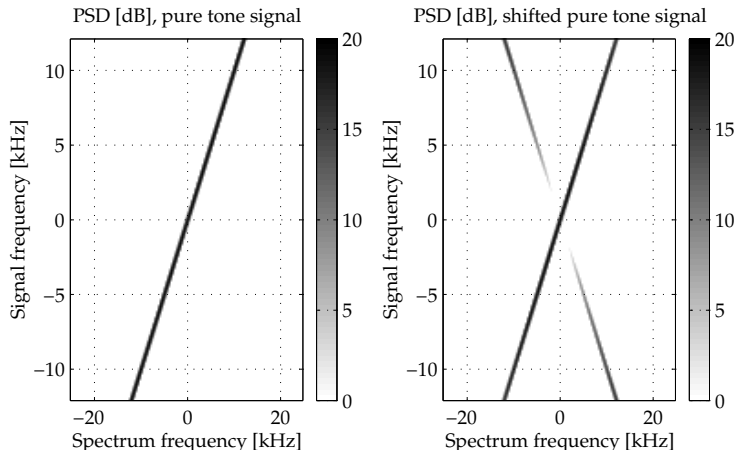


**Figure 5.14:** Simulating the error on synthetic (pure-tone) signal. The left panel shows power spectra of a pure-tone signal, for frequencies matching those observed in our experiment. The right panel shows the result when a delay of one 20 $\mu$s sample is introduced in the imaginary part.

### 5.5.3 Simulations

A simple simulation is shown in figure 5.14. A synthetic tone was generated at frequencies from $-12$ to 12 kHz, sampled at 20 $\mu$s, just like the data in our experiment. Power spectra were then computed using a direct FT method. The result is shown in the left panel. The imaginary part of the signal was advanced by one 20 $\mu$s sample and the computations were repeated. The result is shown in the right panel. As expected, the effect on spectra is a partial mirroring around zero frequency, where the mirroring is more pronounced for higher Doppler offsets, the intensity scale of the figure has been narrowed to emphasize this effect.

Another simple simulation illustrates the effect on a symmetric spectrum. In figure 5.15, the simulation of figure 5.14 have been repeated, except that the synthetic signal is real, $\cos \omega t$, multiplied with a constant phasor $e^{i\pi\phi}$ which differs from panel to panel. The first panel shows a purely real signal, and is identical to the result when the imaginary part is not shifted. The effect on a combined (wide-band) spectrum can clearly be hard to imagine intuitively.

Having access to TSV data from the MIDAS-W part of the receive chain, the effect of this error on actual data can be simulated by introducing exactly the same error at the same point in the MIDAS-W processing, and see if this would bring the MIDAS-W and ESR data into agreement. The result is shown in figure 5.16. As we can see, the correspondence is now much better.

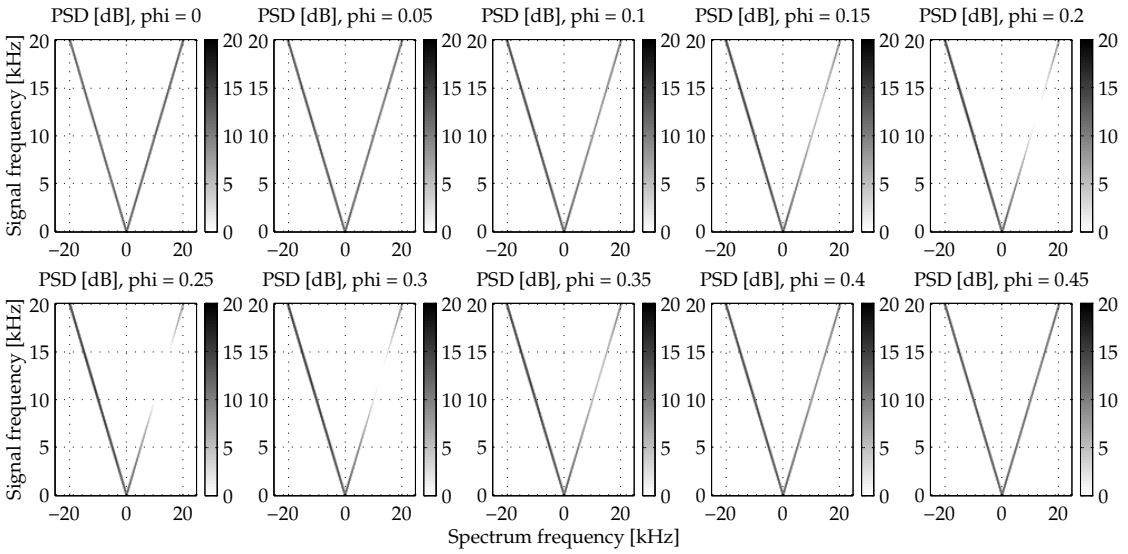


**Figure 5.15:** Simulating the error on symmetric, synthetic (pure-tone) signal, where the signal at negative frequency is shifted in phase relative to the signal at positive frequency. For all panels, a delay of 20 $\mu$s has been introduced in the imaginary part.

### 5.5.4 Recovering information on the spectral peaks

Despite the worrying picture shown in figure 5.15, thermal spectra are hardly influenced by the effect — it managed to go unnoticed for 9 months — and there appears to be little reason to worry overly much about the results on analysed results. For enhanced and asymmetric spectra, however, the ESR spectra are clearly unusable. In our experiment, we have the possibility of replacing the contaminated LPMs with equivalent ones computed from the MIDAS-W data (appropriately scaled.) For previously collected data, this is not an option, and it would be useful if the effect of the error could be removed somehow.

As can be seen from the above, a complete understanding of how an arbitrary spectrum is affected by the error can be found. Analysis programs can then apply an analytic distortion to theoretical spectra, in a same way that any other instrumental effect is applied, before comparing with observations. This reduces the effect of the error as much as can be hoped for.

The technique due to Forme and Fontaine (1999) is used to calculate electron temperatures and ion drift velocities during periods of enhanced echoes using only information about the position of the spectral peaks during the event and assuming that some parameters (i.e. ion temperature and ion composition) remain constant throughout. This technique suggests that a simpler method, with the more limited aim of recovering only the position of the

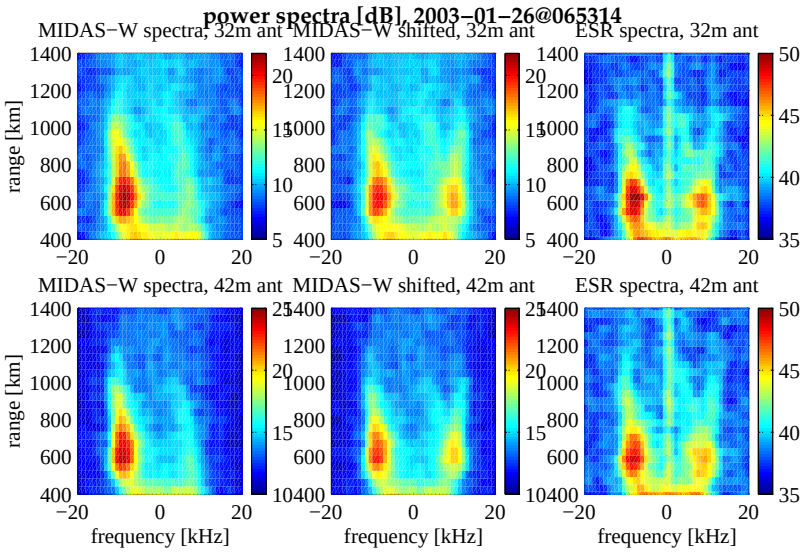


**Figure 5.16:** The observed enhancement event, as seen by the two systems. MIDAS-W spectra to the left, MIDAS-W spectra produced when introducing the same effect as that found in the ESR system in the middle, and ESR spectra to the right.

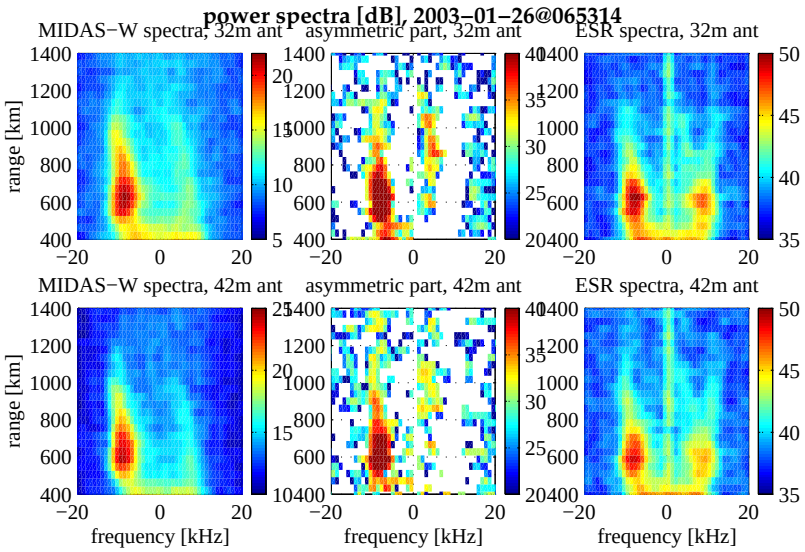


**Figure 5.17:** Recovering the position of the spectral peaks from data contaminated by the data transfer error. The leftmost panels are MIDAS-W spectra, as before, the middle two panels are show the anti-symmetric part of the ESR spectra, wherever it is positive, and the rightmost panels show unmodified ESR spectra.

spectral peaks for asymmetric spectra could be useful. Since the error causes asymmetric spectra to become artificially symmetrised, we separated the spectrum into symmetric and anti-symmetric parts, discarding the symmetric part and keeping only the positive values in the anti-symmetric part. The result is shown in figure 5.17. For cases where the asymmetry is less obvious, some sophistication is necessary for deciding when to use unmodified spectra and when to use the above method to recover asymmetric peaks.

# Chapter 6

# Observations

In this chapter, we present some observations with data acquired using the MIDAS-W data acquisition system (Holt *et al.*, 2000, Paper 2), and processed using software from the same project (Grydeland *et al.*, 2003c, Paper 3). Results of interferometry from the ESR are presented in papers 4 and 5 (Grydeland *et al.*, 2003a,b) and shown as an example in paper 3.

A wider selection of observations is available on the accompanying CD-ROM, including animations, a presentation format which does not currently lend itself to printing.

## 6.1 Millstone Hill observations

As mentioned previously, MIDAS-W is the production data acquisition system for the Millstone Hill IS radar, and has been since November 2001.

Many observations have been made possible through the new architecture that were not previously possible.

From October 6 to November 4, 2002, the ESR and Millstone Hill radars both ran continuously, providing a unique dataset for ionospheric studies, and demonstrating the stability of the architecture. Correctness of the software for ordinary operations is demonstrated through cross-comparison with previously obtained data.

The profiles shown in figure 6.1 are from this 30-day run, from an alternating code profile.

## 6.2 SOUSY Svalbard Radar

An attempt was made in 2001 to make interferometric observations of Polar Mesospheric Summer Echoes (PMSE) using the SOUSY Svalbard Radar with our portable MIDAS-W receiver. The SOUSY Svalbard Radar and operates at 53.5 MHz.

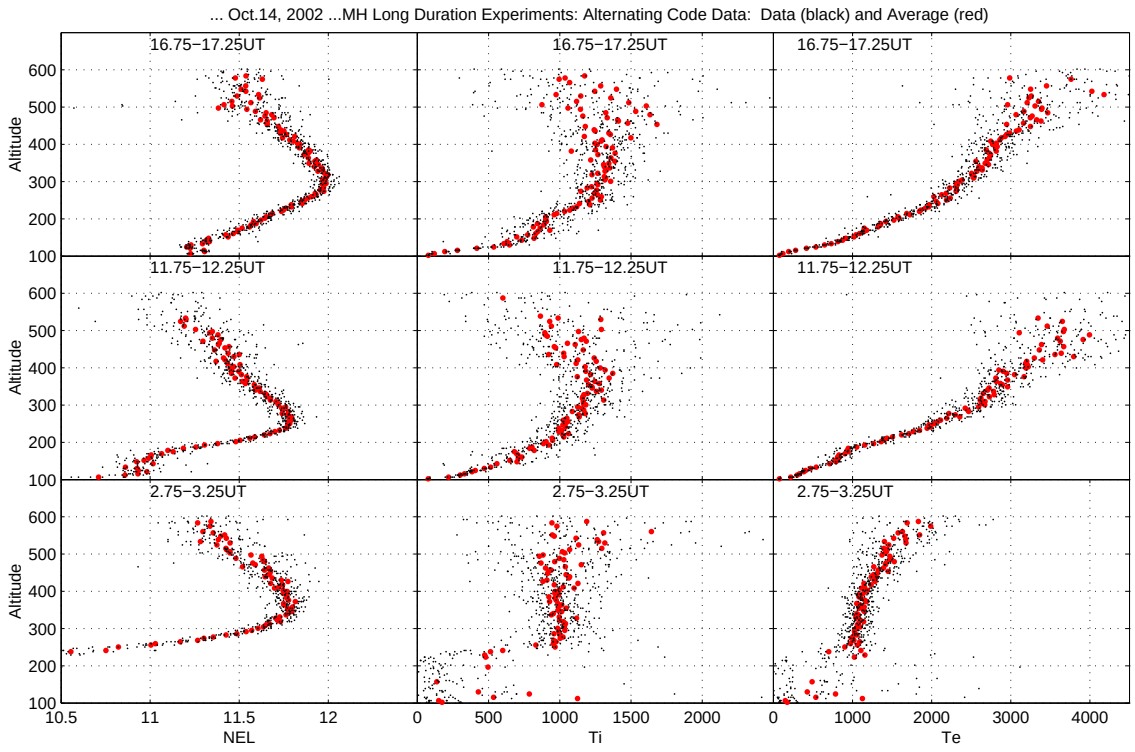


**Figure 6.1:** Example of electron density and electron and ion temperature profiles obtained with the Millstone Hill radar using alternating codes on 2002-10-14, part of the 30 continuous days of observation in October and November 2002. Figure courtesy of Shunrong Zhang.

The radar experiment uses complementary codes, with 2 $\mu$s baud length. The IF used for sampling is centered at 30 MHz, and an anti-aliasing filter of 600 kHz bandwidth was used. The usually employed sampling rate of 1 MHz has a boundary between two aliasing zones at 30 MHz, which would result in only half of the bandwidth being available, and with only half the signal to noise ratio (SNR). A sampling interval of 775 ns, (1.029 MHz sampling rate) was therefore used instead. This has an alias-free band ranging from 29.68 MHz to 30.32 MHz which was a pretty good fit to the IF and filters at a moderate increase in data rate. Unfortunately, this resulted in a significant mismatch with the baud length of the radar program, and re-sampling the data to the new sampling rate turned out to be hard, as the phase changes no longer corresponded to sample boundaries in the original signal.

In figure 6.2 power profiles obtained from the two antenna halves of the SOUSY radar are shown. A PMSE layer is clearly visible, but the layered structure seen outside the main layer is probably an artefact connected with the sampling mismatch described above.

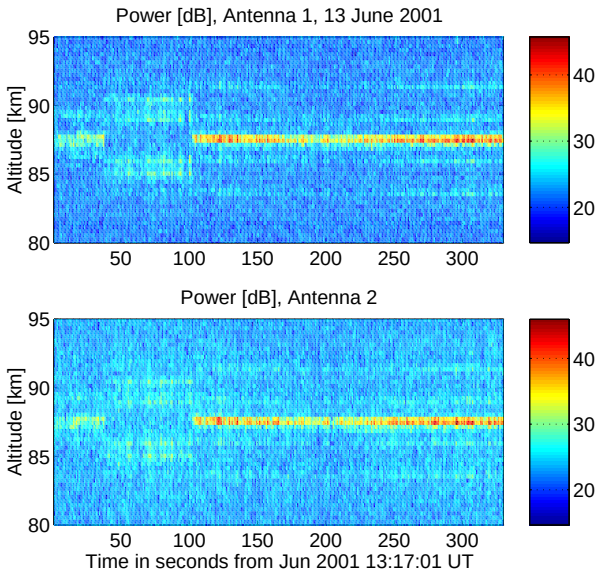


**Figure 6.2:** Power profiles obtained at the SOUSY Svalbard Radar on 2001-06-13, at 13:17 UT. A PMSE layer is visible from 100 seconds on. The secondary layering seen is most likely an artefact due to mismatched sampling.

## 6.3 Enhanced ion-acoustic echoes at the ESR

As discussed in the chapter on enhanced ion-acoustic echoes, the first observations from the EISCAT system were reported in 1991, with several theoretical papers in the following years.

From its inauguration in 1996, a number of observations of unusual spectral features were made at the ESR (Buchert *et al.*, 1999; Ogawa *et al.*, 2000). In addition to enhanced, asymmetric spectra similar to those already observed at the mainland radars, other forms of unusual echoes with lower scattered power and irregular spectral features were observed, but these have not been published (A. P. van Eyken, private comm. 1998).

With the inauguration of the second, fixed 42 m antenna at the ESR in 1999, the opportunity arose of using the two antennas as a receiver-side interferometer. At that time, the receiving system at the ESR was only capable of receiving signal from one antenna at a time, so the University of Tromsø assembled a portable MIDAS-W type data acquisition system (Holt *et al.*, 2000) to obtain data in form suitable for interferometry.

In the winters of 1999 to 2002, observation campaigns were conducted attempting to observe naturally enhanced ion-acoustic echoes with interferometric resolution. In the last years, these were coordinated with high-resolution narrow field-of-view video cameras to find causal relations between enhanced radar echoes and visible aurora.

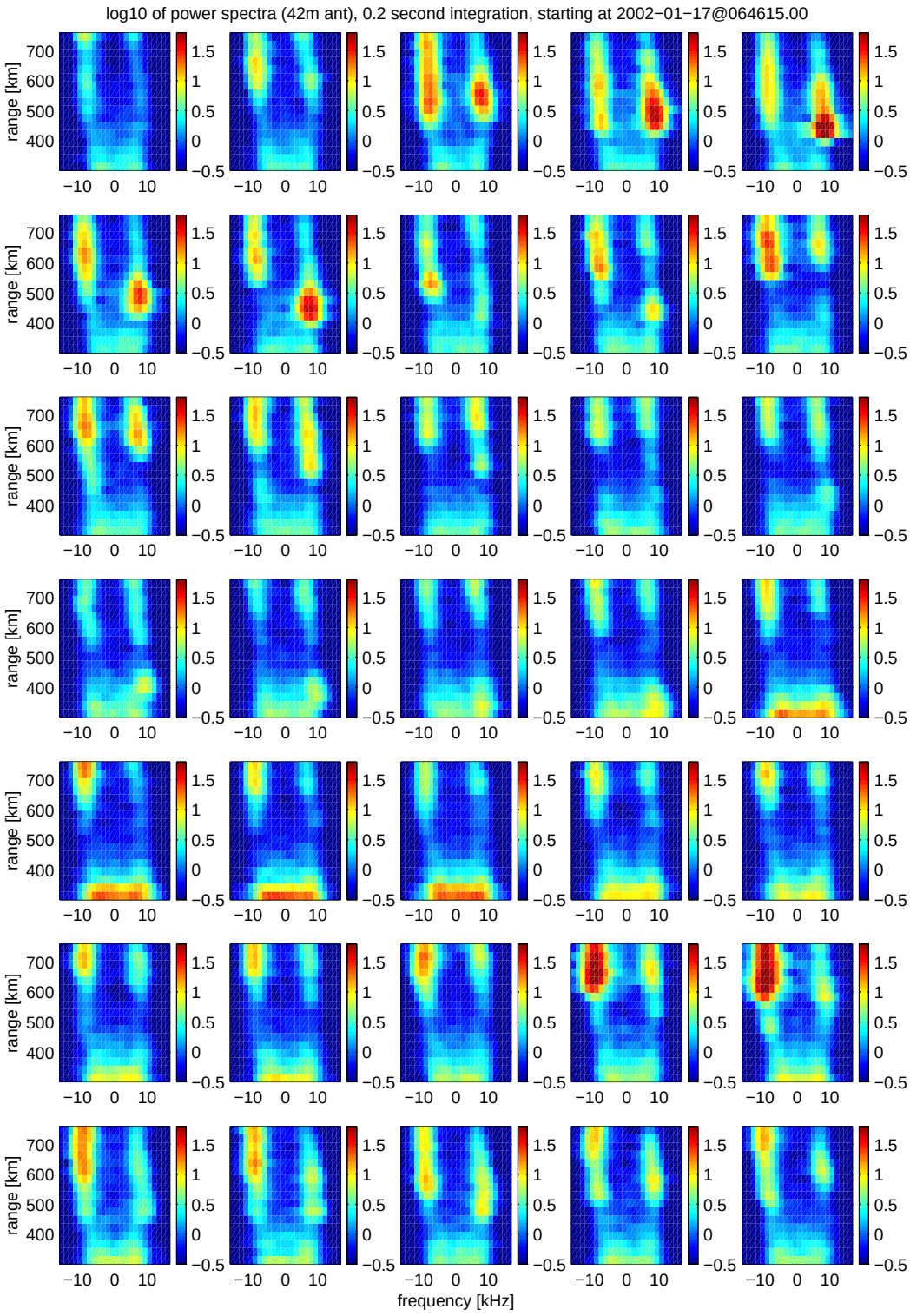


**Figure 6.3:** Power spectra from the ESR, from the event on 2002-01-17. The panels show successive 0.2 s integrations, starting on 06:46:15 UT, near the beginning of the event.

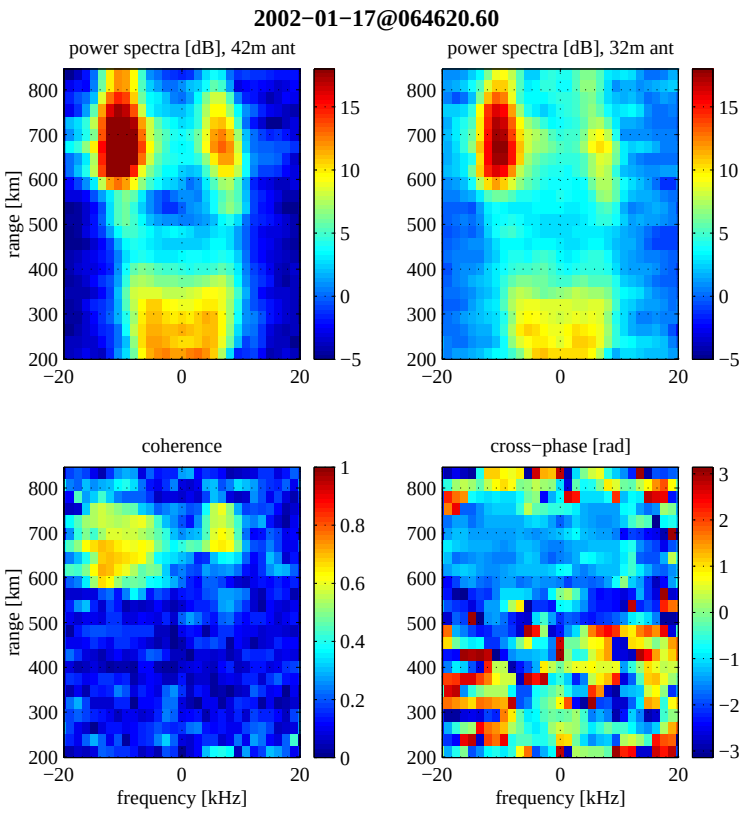


**Figure 6.4:** Power spectra for the two antennae, the coherence and the cross-spectrum phase for an entire profile, this one from a 0.2 s integration starting at 06:46:20.60 UT.

Figure 6.3 shows a succession of 0.2 s integrations from the event of 2002-01-17, starting near the onset of the event and lasting a significant fraction of it. Every line in the figure is a second of data, seven seconds total.

### 6.3.1 Interferometry

Figure 6.4 shows an example of an ionospheric profile of interferometric observation. The panels show power spectra from the 42 m and 32 m antennas, coherence and phase for a 0.2 s integration starting at 06:46:20.60 UT. This is the same data used in one of the published papers (Grydeland *et al.*, 2003b), but reprocessed to cover greater ranges and using three of the four pulses per IPP instead of two, as in the paper.

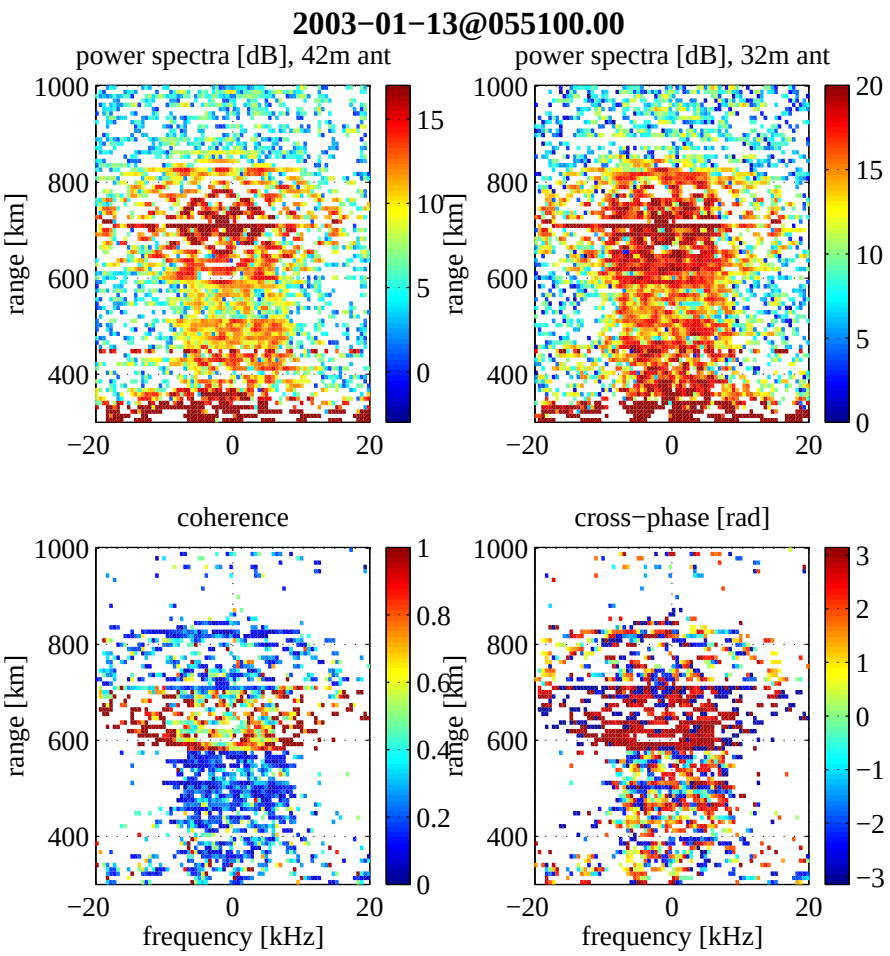


**Figure 6.5:** An example of what is probably a satellite echo seen with the alternating code experiment `tau0`. The signal has been strong enough to saturate the receiver, resulting in the complete breakdown of the code. This data was processed using three times oversampling (60 $\mu$s bauds, 20 $\mu$s decimated samples), three neighbouring range gates were added for 9 km range resolution, and the data has been integrated for 12 s.

### 6.3.2 Coded pulses

The alternating code experiment `tau0` was modified slightly to provide triggering signal for the MIDAS-W system and used for interferometry in the winters of 1999, 2000 and 2002. For reasons which elude us, no enhanced echoes have been found in any of this data, or in much else of the `tau0` data at all. In figure 6.5 we show instead an example of what appears to be a hard target at 700 km range. The scatterer is apparently strong enough to saturate the receiver, resulting in the breakdown of the coding, seen by the (point-like)

scatterer being distributed over many ranges and frequencies. Between 400 and 600 km, the spectra look reasonable, and the coherence is low, as is expected for volume scattering.

# Chapter 7

# Future Directions

A techniques-oriented work like this is necessarily open-ended, particularly since some of the techniques employed has exposed entirely new features of the phenomenon under investigation. The use of radar interferometry for such dynamic phenomena is still in its infancy, and many improvements are easily imaginable.

## 7.1 Phase rotation for velocity determination

The interferometer in the basic form only sees structures which remain in the same position for the duration of the integration. A structure which moves too far along the baseline will interfere destructively with itself, and will not be detected.

When computing cross-spectra, we can modify the phase of one of the signals from one pulse to the next to look for moving structures. This is exactly the same as the phase rotation used in radio astronomy interferometry to compensate for the apparent motion of the source across the sky due to the Earth's rotation.

For a preliminary test, the coherence computation described in section 5.2 was repeated a number of times with different phase increments, where phase increment has been specified in radians per IPP, and the IPP of the `gup0` experiment is 6.720 ms. What this translates to in terms of velocities along the baseline is of course range dependent. Maximum coherence was extracted for range-Doppler regions and plotted vs. phase increment in figure 7.1. While there is reason to believe interesting results can be obtained by looking at non-zero phase increments, this figure also shows that finding good criteria for distinguishing true coherence from noise will be essential. Manually inspecting the full four-panel plots for all phase increments of the integration in the figure reveals that only the upshifted (solid lines) coherences at small negative phase increments are likely to come from a localised scatterer, the high downshifted coherence (broken line) at large positive phase increment is due to noise.

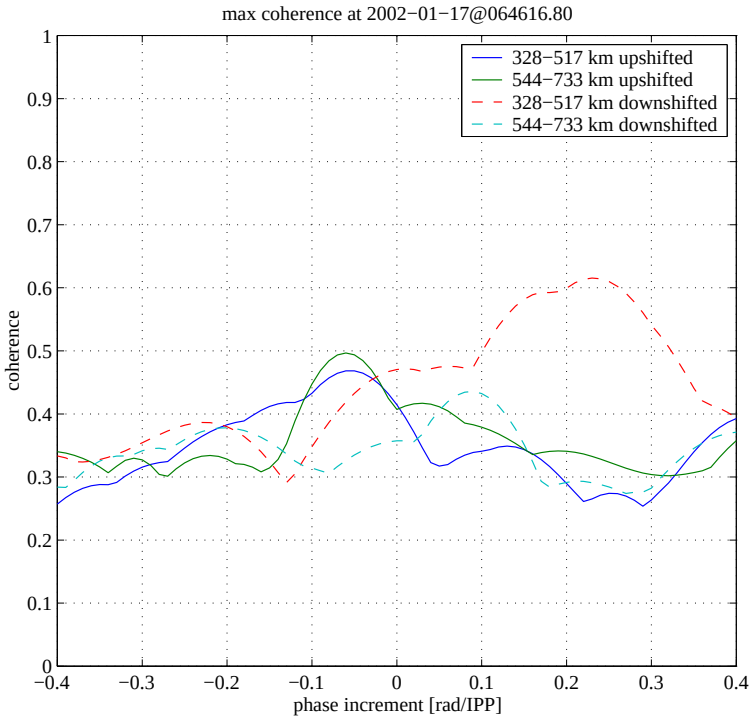


**Figure 7.1:** Phase rotation, preliminary test. The figure shows maximum coherence in each of four range-Doppler cells as a function of phase shift per IPP. The data is from a 0.2 s integration starting at 06:46:16.80 on 2002-01-17.

## 7.2 Combined interferometry and digital beam-forming: precise horizontal localization of scatterer

The techniques of receiver-side interferometry and digital beam-forming are different and complementary ways of looking at the same basic information when several receivers are available for the same signal.

Beam-forming in phased arrays means applying phase to the signal from every single antenna element and combining these, resulting in a beam pattern quite different from (usually narrower than) the beams of any single element. As long as signal arrives from many different directions, there is in principle no reason to limit the number of beams formed, as is exploited in e.g. imaging riometers (Stauning, 1996, and references therein). When signal in TSV form is available from each element, beam-forming can be performed numerically, called *digital beam-forming*, and can even be performed after the fact on recorded TSV data. While the resulting beams are narrower than the single-element beams, the beam

itself defines the resolution, as for ordinary single-element antennas. If a scatterer is inside the beam it is seen, otherwise it is not.

Interferometry, as we have seen at length already, is different in that only scattering from localised structures can be detected, and with a coherence level determined by the structure's size along the baseline. Interferometry with a single baseline results in ambiguous position estimates. In the cases presented in previous chapters, there are 4 or 5 likely positions along the baseline for each observed structure.

Digital beam-forming on the signal from two high-gain antennas pointing in the same direction might appear to be a peculiar exercise, particularly since the illuminated volume was defined in transmission. Combined with the positioning ambiguity of the single-baseline interferometer, however, we see how the possibility arises of sweeping a digitally formed beam *using exactly the same signals* over the scattering volume. This can be used to resolve the ambiguity, at least for the cases where the discrete structure is scattering much more strongly than the rest of the volume.

## 7.3 Interferometric Imaging

At Jicamarca, interferometric imaging is used for imaging of $E$ and $F$ region irregularities, with multiple baselines created from sub-fields of the large phased array (e.g. Kudeki and Sürücü, 1991; Hysell, 1996; Chau and Woodman, 2001a).

While assembling a phased array or an array of 32 m antennas is probably too expensive, the very high scattering levels seen for anomalous echoes implies that it should be possible to observe this signal on a more modest receive-only antenna. It is probably feasible to distribute a modest number of inexpensive (3–5 m fixed parabolic dish) antennas in the immediate vicinity of the ESR antennas to obtain multiple interferometry baselines, and where data would only be recorded whenever enhanced echoes were detected on the main dish.

Similarly, the very strong signal level and modest altitude of PMSE ($\sim$ 80 km) should make it feasible to distribute a number of inexpensive 3 m dipole antennas in the vicinity of the SOUSY Svalbard radar for interferometric imaging of this high-latitude phenomenon.

# Chapter 8

# Summary and Conclusions

In this thesis, the interesting subject of naturally enhanced ion-acoustic echoes has been investigated. The different theories proposed for explaining them have been presented, and their implications on observable quantities have been discussed.

Observations made with the older EISCAT systems of naturally enhanced ion-acoustic echoes and plasma lines at the same time were presented. The simultaneous occurrence of enhanced ion-acoustic echoes and plasma lines favours an explanation for the enhanced echoes based on beam-excited Langmuir Turbulence.

To enable more detailed observations, a new architecture for the development of software for radio science has been designed. Signal processing components have been implemented and demonstrated to work reliably for incoherent scattering radars.

Using this technology framework, an interferometric technique involving the two antennas of the ESR has been developed for the study of filamented structure in the auroral ionosphere. An method for determining the horizontal size of a localised scatterer has been developed, taking into account the different beam patterns of the antennas.

A portable data acquisition system has been assembled and used to collect large quantities of data, with some occurrences of naturally enhanced echoes. The time development of such an enhancement event was investigated and found to vary significantly on sub-second timescales. A typical timescale for the development of the enhanced scattering was found, and it was seen that enhancement occurs simultaneously in both shoulders on this typical timescale for the duration of the enhancement event.

Through the interferometric technique, the enhanced echoes were found to arise from very localised regions in the auroral ionosphere, a result which implies scattering cross-sections two to three orders of magnitude above what was previously suspected. This result has significant impact on theories, as such enhancement can only be explained through plasma instability, and explanations based on marginal stability can be excluded.

The opportunity for limited horizontal positioning offered by single-baseline interferometry has been used to show that simultaneous enhancement of both ion-acoustic shoulders occur

predominantly in the same position along the baseline. Together with the observation that they occur at the same time, this leads to the conclusion that enhancement of both shoulders is produced in the same volume. This eliminates theoretical explanations which only explain enhancement of one shoulder at a time.

Significant contributions have been made to the field of radio science instrumentation through the work done in Software Radar.

A receiver-side interferometric technique has been introduced for the study of naturally enhanced ion-acoustic echoes, and significant new knowledge of this phenomenon has been acquired through this technique.

The obtained results have clear implications on theoretical explanations for such enhancements. In particular we find that the explanation based on the ion-electron two-stream instability favoured by many authors is unlikely to explain our observations.

The conclusions drawn here throws all previous observations of simultaneous enhancement into a new light, and these observations should be revisited.

# References

**Bjørnå, N.**, Derivation of ion-neutral collision frequencies from a combined ion line/plasma line incoherent scatter experiment, *J. Geophys. Res.*, *94*(A4), 3799–3804, 1989.

**Bjørnå, N. and Kirkwood, S.**, Derivation of ion composition from a combined ion line/plasma line incoherent scatter experiment, *J. Geophys. Res.*, *93*(A6), 5787–5793, 1988.

**Bjørnå, N. and Trulsen, J.**, Effect of a power law particle flux on the ionospheric incoherent scattering cross section, *Phys. Scripta*, *33*, 284–288, 1986.

**Bjørnå, N., Havnes, O., Jensen, J. O., and Trulsen, J.**, Enhancement of the incoherent scattering plasma lines due to precipitating protons and secondary electrons, *Phys. Scripta*, *25*, 632–636, 1982.

**Buchert, S. C., van Eyken, A. P., Ogawa, T., and Watanabe, S.**, Naturally enhanced ion-acoustic lines seen with the EISCAT Svalbard Radar, *Adv. Space Res.*, *23*(10), 1699–1704, doi:10.1016/S0273-1177(99)00382-8, 1999.

**Bythrow, P. F., Potemra, T. A., Hanson, W. B., Zanetti, L. J., Meng, C.-I., Huffman, R. E., Rich, F. J., and Hardy, D. A.**, Earthward directed high-density Birkeland currents observed by HILAT, *J. Geophys. Res.*, *89*(A10), 9114–9118, 1984.

**Chau, J. L. and Woodman, R. F.**, Three-dimensional coherent radar imaging at Jicamarca: comparison of different inversion techniques, *J. Atmos. Sol. Terr. Phys.*, *63*(2-3), 253–261, doi:10.1016/S1364-6826(00)00142-5, 2001a.

**Chau, J. L. and Woodman, R. F.**, Interferometric and dual-beam observations of daytime spread-$F$-like irregularities over Jicamarca, *Geophys. Res. Lett.*, *28*(18), 3581–3584, 2001b.

**Collis, P. N., Häggström, I., Kaila, K., and Rietveld, M. T.**, EISCAT radar observations of enhanced incoherent scatter spectra; their relation to red aurora and field-aligned currents, *Geophys. Res. Lett.*, *18*(6), 1031–1034, 1991.

**Damtie, B., Nygrén, T., Lehtinen, M. S., and Huuskonen, A.**, High resolution observations of sporadic-E layers within the polar cap ionosphere using a new incoherent scatter radar experiment, *Ann. Geophys.*, *20*(9), 1429–1438, 2002.

**Damtie, B., Lehtinen, M. S., and Nygrén, T.**, Decoding of Barker coded incoherent scatter measurements by means of mathematical inversion, *Ann. Geophys.*, *21*, accepted, 2003.

**Djuth, F. T., Sulzer, M. P., and Elder, J. H.**, Application of the coded long-pulse technique to plasma line studies of the ionosphere, *Geophys. Res. Lett.*, *21*(24), 2725–2728, 1994.

**Djuth, F. T., Sulzer, M. P., Elder, J. H., and Grover, K. M.**, The CRRES AA 2 release: HF wave-plasma interactions in a dense $Ba^+$ cloud, *J. Geophys. Res.*, *100*(A9), 17 347–17 366, 1995.

**Dougherty, J. P. and Farley, D. T.**, A theory of incoherent scattering of radio waves by a plasma, *Proc. Roy. Soc.*, *A 259*, 79–99, part 1 of a series of articles, 1960.

**Erickson, P. J., Lind, F. D., Holt, J. M., and Grydeland, T.**, Radar technology development at Millstone Hill: The MIDAS-W software radar system, presented at the Radar Techniques Workshop (G), National Radio Science meeting, Boulder, Colorado, USA, 2001.

**Farley, D. T.**, Incoherent scatter correlation function measurements, *Radio Sci.*, *4*(10), 935–953, 1969.

**Farley, D. T.**, Multiple-pulse incoherent-scatter correlation function measurements, *Radio Sci.*, *7*(6), 661–666, 1972.

**Farley, D. T.**, Incoherent scatter radar probing, in *Modern Ionospheric Science*, edited by H. Kohl, R. Rüster, and K. Schlegel, pp. 415–439, European Geophysical Society, 1996.

**Farley, D. T., Ierkic, H. M., and Fejer, B. G.**, Radar interferometry: A new technique for studying plasma turbulence in the ionosphere, *J. Geophys. Res.*, *86*(A3), 1467–1472, 1981.

**Fejer, J. A.**, Scattering of radio waves by an ionized gas in thermal equilibrium, *Can. J. Phys.*, *38*, 1114–1133, 1960.

**Fontaine, D. and Forme, F.**, Ionospheric small-scale structures and turbulence inferred from EISCAT observations: a review, *J. Geomag. Geoelectr.*, *47*(9), 869–878, 1995.

**Forme, F., Ogawa, Y., and Buchert, S. C.**, Naturally enhanced ion acoustic fluctuations seen at different wavelengths, *J. Geophys. Res.*, *106*(A10), 21 503–21 515, 2001.

**Forme, F. R. E.**, A new interpretation on the origin of enhanced ion acoustic fluctuations in the upper ionosphere, *Geophys. Res. Lett.*, *20*(21), 2347–2350, 1993.

**Forme, F. R. E.**, Parametric decay of beam-driven Langmuir wave and enhanced ion-acoustic fluctuations in the ionosphere: a weak turbulence approach, *Ann. Geophys.*, *17*(9), 1172–1181, doi:10.1007/s005850050842, 1999.

**Forme, F. R. E. and Fontaine, D.**, Enhanced ion acoustic fluctuations and ion outflows, *Ann. Geophys.*, *17*(2), 182–189, doi:10.1007/s005850050749, 1999.

**Forme, F. R. E., Fontaine, D., and Wahlund, J. E.**, Two different types of enhanced ion acoustic fluctuations observed in the upper ionosphere, *J. Geophys. Res.*, *100*(A8), 14 625–14 636, 1995.

**Foster, J. C.**, Plasma turbulence and enhanced UHF radar backscatter from the topside ionosphere, in *Physics of Space Plasmas (1988), SPI Conference Proceedings*, vol. 8, pp. 213–229, Scientific Publishers, Inc., 1990.

**Foster, J. C., del Pozo, C., Groves, K., and St. Maurice, J.-P.**, Radar observations of the onset of current driven instabilities in the topside ionosphere, *Geophys. Res. Lett.*, *15*(2), 160–163, 1988.

**Gamma, E., Helm, R., Johnson, R., and Vlissides, J.**, *Design Patterns: Elements of Reusable Object-Oriented Software*, Addison-Wesley, 1994.

**Groves, K. M., Lee, M. C., and Foster, J. C.**, Nonlinear ionospheric propagation effects on UHF radio signals, in *Physics of Space Plasmas (1991), SPI Conference Proceedings*, vol. 11, pp. 377–392, Scientific Publishers, Inc., 1991.

**Grydeland, T.**, *Observations of Auroral Plasma Lines*, Master's thesis, University of Tromsø, Tromsø, 1998.

**Grydeland, T., Holt, J. M., and Erickson, P. J.**, MIDAS-W: A workstation-based incoherent scatter radar data acquisition system, presented at the IX. International EISCAT Workshop, Wernigerode, Germany, 1999.

**Grydeland, T., Holt, J. M., Erickson, P. J., and Lind, F. D.**, Recent observational techniques for is plasma line observations, presented at the National Radio Science meeting Radar Techniques Workshop (G), Boulder, CO, USA, 2001a.

**Grydeland, T., Lind, F. D., Erickson, P. J., and Holt, J. M.**, Reusable signal processing components for Software Radars, presented at the X. International EISCAT Workshop, session 5, New Hardware and Software Developments, Tokyo, Japan, 2001b.

**Grydeland, T., Blixt, E. M., Løvhaug, U. P., Hagfors, T., La Hoz, C., and Trondsen, T. S.**, Interferometric radar observations of filamented structures due to plasma instabilities and their relation to dynamic auroral rays, *Ann. Geophys.*, submitted, 2003a.

**Grydeland, T., La Hoz, C., Hagfors, T., Blixt, E. M., Saito, S., Strømme, A., and Brekke, A.**, Interferometric observations of filamentary structures associated with plasma instability in the auroral ionosphere, *Geophys. Res. Lett.*, *30*(6), 1338, doi:10.1029/2002GL016362, 2003b.

**Grydeland, T., Lind, F. D., Erickson, P. J., and Holt, J. M.**, Software radar signal processing, *Radio Sci.*, in preparation, 2003c.

**Guio, P. and Lilensten, J.**, Effect of suprathermal electrons on the intensity and Doppler frequency of electron plasma lines, *Ann. Geophys.*, *17*(7), 903–912, doi:10.1007/s005850050817, 1999.

**Hagfors, T.**, Density fluctuations in a plasma in a magnetic field, with applications to the ionosphere, *J. Geophys. Res.*, *66*(6), 1699–1712, 1961.

**Holt, J. M., Rhoda, D. A., Tetenbaum, D., and van Eyken, A. P.**, Optimal analysis of incoherent scatter radar data, *Radio Sci.*, *27*(3), 435–447, 1992.

**Holt, J. M., Erickson, P. J., Gorczyca, A. M., and Grydeland, T.**, MIDAS-W: a workstation-based incoherent scatter radar data acquisition system, *Ann. Geophys.*, *18*(9), 1231–1241, doi:10.1007/s005850000271, 2000.

**Holt, J. M., Lind, F. D., Erickson, P. J., and Grydeland, T.**, The Open Radar Initiative, presented at the X. International EISCAT Workshop, session 5, New Hardware and Software Developments, Tokyo, Japan, 2001.

**Huuskonen, A., Lehtinen, M. S., and Pirttilä, J.**, Fractional lags in alternating codes: Improving incoherent scatter measurements by using lag estimates at noninteger multiples of baud length, *Radio Sci.*, *31*(2), 245–261, 1996.

**Hysell, D. L.**, Radar imaging of equatorial $F$ region irregularities with maximum entropy interferometry, *Radio Sci.*, *31*(6), 1567–1578, 1996.

**Isham, B., Rietveld, M. T., Grydeland, T., La Hoz, C., Leyser, T. B., Honary, F., Kosch, M., Hagfors, T., and Ueda, H.**, HF-pump-induced parametric instabilities in the auroral E-region, presented at the 20th Anniversary Symposium on Ionospheric Interactions in Tromsø, 2000.

**Kirkwood, S., Nilsson, H., Lilensten, J., and Galand, M.**, Strongly enhanced incoherent-scatter plasma lines in aurora, *J. Geophys. Res.*, *100*(A11), 21 343–21 355, 1995.

**Kofman, W., Lejeune, G., Hagfors, T., and Bauer, P.**, Electron temperature measurements by the plasma line technique at the french incoherent scatter radar facilities, *J. Geophys. Res.*, *86*(A8), 6795–6801, 1981.

**Kudeki, E. and Sürücü, F.**, Radar interferometric imaging of field-aligned plasma irregularities in the equatorial electrojet, *Geophys. Res. Lett.*, *18*(1), 41–44, 1991.

**Kudeki, E., Bhattacharyya, S., and Woodman, R. F.**, A new approach in incoherent scatter $F$ region E x B drift measurements at Jicamarca, *J. Geophys. Res.*, *104*, 28 145–28 162, 1999.

**La Hoz, C., Rietveld, M. T., Grydeland, T., and Isham, B.**, Observations of anomalous ion line spectra associated with enhanced plasma lines during auroral precipitation, presented at the AGU fall meeting, San Francisco, 2000a.

**La Hoz, C., Rietveld, M. T., Isham, B., and Grydeland, T.**, HF-pump-induced parametric instabilities in the auroral E-region, presented at the 20th Anniversary Symposium on Ionospheric Interactions in Tromsø, 2000b.

**Lehtinen, M., Markkanen, J., Väänänen, A., Huuskonen, A., Damtie, B., Nygrén, T., and Rahkola, J.**, A new incoherent scatter technique in the EISCAT Svalbard Radar, *Radio Sci.*, *37*(4), 1050, doi:10.1029/2001RS002518, 2002.

**Lehtinen, M. S.**, Statistical theory of incoherent scatter measurements, Tech. Rep. 86/45, EISCAT Scientific Association, Kiruna, Sweden, ph. D. Thesis, University of Helsinki, Helsinki, Finland, 1986.

**Lehtinen, M. S. and Häggström, I.**, A new modulation principle for incoherent scatter measurements, *Radio Sci.*, *22*(4), 625–634, 1987.

**Lehtinen, M. S. and Huuskonen, A.**, The use of multipulse zero lag data to improve incoherent scatter radar power profile accuracy, *J. Atmos. Terr. Phys.*, *48*(9-10), 787–793, 1986.

**Lehtinen, M. S., Huuskonen, A., and Pirttilä, J.**, First experiences of full-profile analysis with GUISDAP, *Ann. Geophys.*, *14*(12), 1487–1495, doi:10.1007/s005850050410, 1996.

**Lehtinen, M. S., Huuskonen, A., and Markkanen, M.**, Randomization of alternating codes: Improving incoherent scatter measurements by reducing correlations of gated autocorrelation function estimates, *Radio Sci.*, *32*(6), 2271–2282, 1997.

**Lind, F. D., Erickson, P. J., Holt, J. M., and Grydeland, T.**, The Open Radar Initiative: Reliable technology for Radio Science, presented at the Radar Techniques Workshop (G), National Radio Science meeting, Boulder, Colorado, USA, 2001.

**Lind, F. D., Erickson, P. J., Holt, J. M., and Grydeland, T.**, The Open Radar Initiative, *Radio Science Bulletin*, in preparation, 2003.

**Meyer, M., Zhou, C., Gidner, D., and Sahr, J.**, Passive VHF radar interferometer observation of meteor trails, presented in the New Approaches to radio sensing of the Terrestrial plasma environment (GJii) session of the XXVIIth URSI General Assembly, Maastricht, the Netherlands, 2002.

**Noël, J.-M. A., St.-Maurice, J.-P., and Blelly, P.-L.**, Nonlinear model of short-scale electrodynamics in the auroral ionosphere, *Ann. Geophys.*, *18*(9), 1128–1144, doi:10.1007/s005850000265, 2000.

**Nygrén, T.**, *Introduction to incoherent scatter measurements*, Invers Publications, Sodankylä, Finland, 1996.

**Ogawa, Y., Forme, F., and Buchert, S. C.**, Frequency dependent power fluctuations: a feature of the ESR system or physical?, *Ann. Geophys.*, *18*(9), 1224–1230, doi:10.1007/s005850000282, 2000.

**Percival, D. B. and Walden, A. T.**, *Spectral analysis for physical applications*, Cambridge University Press, Cambridge, England, 1993.

**Perkins, F. and Salpeter, E. E.**, Enhancement of plasma density fluctuations by nonthermal electrons, *Phys. Rev.*, *139*(1A), A55–A62, doi:10.1103/PhysRev.139.A55, 1965.

**Perkins, F. W., Salpeter, E. E., and Yngvesson, K. O.**, Incoherent scatter from plasma oscillations in the ionosphere, *Phys. Rev. Lett.*, *14*(15), 579–581, doi:10.1103/PhysRevLett.14.579, 1965.

**Pines, D. and Bohm, D.**, A collective description of electron interactions: II. collective *vs* individual particle aspects of the interactions, *Phys. Rev.*, *85*(2), 338–353, doi:10.1103/PhysRev.85.338, 1952.

**Reed, J. H.**, *Software Radio*, Communications Engineering and Emerging Technologies Series, Prentice-Hall PTR, 2002.

**Rietveld, M. T., Collis, P. N., and St.-Maurice, J.-P.**, Naturally enhanced ion acoustic waves in the auroral ionosphere observed with the EISCAT 933-MHz radar, *J. Geophys. Res.*, *96*(A11), 19 291–19 305, 1991.

**Rietveld, M. T., Collis, P. N., van Eyken, A. P., and Løvhaug, U. P.**, Coherent echoes during EISCAT UHF common programmes, *J. Atmos. Terr. Phys.*, *58*(1-4), 161–174, doi:10.1016/0021-9169(95)00027-5, 1996.

**Rietveld, M. T., Isham, B., La Hoz, C., Grydeland, T., Honary, F., Leyser, T. B., Ueda, H., Kosch, M., and Hagfors, T.**, HF-enhanced F region electron temperatures and E region plasma lines from the nighttime auroral ionosphere, presented at Committee on Space Research (COSPAR) 33nd Scientific Assembly, Warsaw, Poland, 2000.

**Rietveld, M. T., Isham, B., Grydeland, T., La Hoz, C., Leyser, T. B., Honary, F., Ueda, H., Kosch, M., and Hagfors, T.**, HF-pump-induced parametric instabilities in the auroral E-region, *Adv. Space Res.*, *29*(9), 1363–1368, doi:10.1016/S0273-1177(02)00186-2, 2002.

**Robinson, P. A.**, Nonlinear wave collapse and strong turbulence, *Rev. Mod. Phys.*, *69*(2), 507–573, doi:10.1103/RevModPhys.69.507, 1997.

**Rosenbluth, M. N. and Rostoker, N.**, Scattering of electromagnetic waves by a nonequilibrium plasma, *Phys. Fluids*, *5*(7), 776–788, 1962.

**Rostoker, N.**, Test particle method in kinetic theory of a plasma, *Phys. Fluids*, *7*(4), 491–498, 1964.

**Saito, S., Forme, F. R. E., Buchert, S. C., Nozawa, S., and Fujii, R.**, Effects of a kappa distribution function of electrons on incoherent scatter spectra, *Ann. Geophys.*, *18*(9), 1216–1223, doi:10.1007/s005850000264, 2000.

**Salpeter, E. E.**, Electron density fluctuations in a plasma, *Phys. Rev.*, *120*(5), 1528–1535, doi:10.1103/PhysRev.120.1528, 1960.

**Sedgemore-Schulthess, F. and St.-Maurice, J.-P.**, Naturally enhanced ion-acoustic spectra and their interpretation, *Surv. Geophys.*, *22*(1), 55–92, doi:10.1023/A:1010691026863, 2001.

**Sedgemore-Schulthess, K. J. F., Lockwood, M., Trondsen, T. S., Lanchester, B. S., Rees, M. H., Lorentzen, D. A., and Moen, J.**, Coherent EISCAT Svalbard Radar spectra from the dayside cusp/cleft and their implication for transient field-aligned currents, *J. Geophys. Res.*, *104*(A11), 24 613–24 624, 1999.

**St.-Maurice, J.-P., Kofman, W., and James, D.**, In situ generation of intense parallel electric fields in the lower ionosphere, *J. Geophys. Res.*, *101*(A1), 335–356, 1996.

**Stasiewicz, K., Holmgren, G., and Zanetti, L.**, Density depletions and current singularities observed by Freja, *J. Geophys. Res.*, *103*(A3), 4251–4260, 1998.

**Stauning, P.**, Investigations of ionospheric radio wave absorption processes using imaging riometer techniques, *J. Atmos. Terr. Phys.*, *58*(6), 753–764, doi:10.1016/0021-9169(95)00072-0, 1996.

**Sulzer, M. P.**, A radar technique for high range resolution incoherent scatter autocorrelation function measurements utilizing the full average power of klystron radars, *Radio Sci.*, *21*(6), 1033–1040, 1986.

**Sulzer, M. P.**, A new type of alternating code for incoherent scatter measurements, *Radio Sci.*, *28*(6), 995–1001, 1993.

**Turunen, T.**, GEN-SYSTEM—a new experimental philosophy for EISCAT radars, *J. Atmos. Terr. Phys.*, *48*(9-10), 777–785, 1986.

**Turunen, T. and Silén, J.**, Modulation patterns for the EISCAT incoherent scatter radar, *J. Atmos. Terr. Phys.*, *46*(6/7), 593–599, 1984.

**Wahlund, J.-E., Forme, F. R. E., Opgenoorth, H. J., Persson, M. A. L., Mishin, E. V., and Volokitin, A. S.**, Scattering of electromagnetic waves from a plasma: enhanced ion acoustic fluctuations due to ion-ion two-stream instabilities, *Geophys. Res. Lett.*, *19*(19), 1919–1922, 1992a.

**Wahlund, J.-E., Opgenoorth, H. J., Häggström, I., Winser, K. J., and Jones, G. O. L.**, EISCAT observations of topside ionospheric ion outflows during auroral activity: Revisited, *J. Geophys. Res.*, *97*(A3), 3019–3037, 1992b.

**Wannberg, G.**, The G2-System and general purpose alternating code experiments for EISCAT, *J. Atmos. Terr. Phys.*, *55*(4/5), 543–557, 1993.

**Yngvesson, K. O. and Perkins, F. W.**, Radar Thomson scatter studies of photoelectrons in the ionosphere and Landau damping, *J. Geophys. Res.*, *73*(1), 97–110, 1968.

**Zakharov, V. E.**, Collapse of Langmuir waves, *Sov. Phys. JETP*, *35*(5), 908–914, (Engl. translation), 1972.